THE OHIO STATE UNIVERSITY

Performance of Traffic-Alert Collision Avoidance (TCAS) Antennas in the Presence of Scatterers

K.S. Sampath, R.G. Rojas and W.D. Burnside

The Ohio State University

ElectroScience Laboratory

Department of Electrical Engineering
Columbus, Ohio 43212

Technical Report 722792-5
Grant No. NAG-1-1058
July 1993

National Aeronautics and Space Adminstration
Langley Research Center
Hampton, VA 23665-5225

A. Approved for public release; Distribution is unlimited

NOTICES

When Government drawings, specifications, or other data are used for any purpose other than in connection with a definitely related Government procurement operation, the United States Government thereby incurs no responsibility nor any obligation whatsoever, and the fact that the Government may have formulated, furnished, or in any way supplied the said drawings, specifications, or other data, is not to be regarded by implication or otherwise as in any manner licensing the holder or any other person or corporation, or conveying any rights or permission to manufacture, use, or sell any patented invention that may in any way be related thereto.

50272-101

REPORT DOCUMENTATION PAGE	1. REPORT NO.	2.	3. Recipient's Accession No.

4. Title and Subtitle
Performance of Traffic-Alert Collision Avoidance (TCAS) Antennas in the Presence of Scatterers

5. Report Date
July 1993

6.

7. Author(s)
K.S. Sampath, R.G. Rojas and W.D. Burnside

8. Performing Org. Rept. No.
722792-5

9. Performing Organization Name and Address
The Ohio State University
ElectroScience Laboratory
1320 Kinnear Road
Columbus, OH 43212

10. Project/Task/Work Unit No.

11. Contract(C) or Grant(G) No.
(C)
(G) NAG-1-1058

12. Sponsoring Organization Name and Address
National Aeronautics and Space Administration
Langley Research Center
Hampton, VA 23665

13. Report Type/Period Covered
Technical Report

14.

15. Supplementary Notes

16. Abstract (Limit: 200 words)

The performance of two TCAS systems is studied in the presence of electromagnetic scatterers. TCAS is an aircraft mounted angle of arrival (AOA) system, which estimates the bearing of a signal transmitted from a mode-S transponder on another nearby aircraft (intruder). Two systems are studied: (i) Comparison of Relative Amplitude system (CRA), and (ii) Spiral Phase Antenna (SPA).

The CRA antenna receives the reply via four switched beams. The bearing is estimated by comparing the amplitudes of the received signal. The SPA is based on the phase interferometer, which utilises the received phase via sum and difference beams. The AOA is computed by comparing the reply with similar values on a calibration table, which is generated by modeling the TCAS antenna on the bare fuselage of a Boeing 727-200. The antenna patterns for the TCAS are found via high frequency methods based on the Uniform Geometric Theory of Diffraction (UTD). By minimizing the standard deviation of the bearing error in a specified angular sector, optimal locations for top and bottom mounted TCAS antennas are found on the Boeing 727-200, 737-300 and 747-200 airframes. It will be shown that the overall bearing errors of the amplitude system are consistently smaller than the spiral phase TCAS.

The effect of two types of nearby scatterers—antennas, and engine inlets—is studied. The AT741 L-band blade, DMC60-1 VHF Communication antenna were chosen as being representative antenna interference examples. Models are derived for the blades via a moment method analysis followed by a least squares procedure to synthesize the scattering patterns. Studies were conducted to estimate the minimum separation between the two antennas for acceptable operation. It will be shown that the spiral phase TCAS is adversely affected by the presence of a blade antenna. The amplitude system does not suffer from this limitation, especially for the forward look angles which are of most interest here.

A model to represent the inlet scattering is based on the multiple scattering method and UTD. The engine on top of the B727-200 fuselage is modeled by a terminated circular waveguide. Then, the effect of moving the antenna forward on the fuselage is studied. It is again shown that the performance of the amplitude system is superior.

17. Document Analysis a. Descriptors

AIRCRAFT
ANTENNAS
ANALYSIS
ELECTROMAGNETIC
PATTERNS
GTD (GEOMETRICAL THEORY OF DIFFRACTION)

b. Identifiers/Open-Ended Terms

c. COSATI Field/Group

18. Availability Statement
A. Approved for public release;
Distribution is unlimited.

19. Security Class (This Report)
Unclassified

20. Security Class (This Page)
Unclassified

21. No. of Pages
142

22. Price

(See ANSI-Z39.18) *See Instructions on Reverse* OPTIONAL FORM 272 (4-77)
Department of Commerce

Contents

List of Figures

List of Tables

Chapter 1

Introduction

1.1 Background and Motivation

The flight safety of an airplane critically relies upon the proper operation of various communication, weather, navigation and other avionic systems [1]. Many of these systems have antennas and/or other structures on the skin of the aircraft. The operational characteristics of any antenna on the airplane include the effect of the various structures making up the airframe and the electromagnetic coupling among the multitude of antennas and transponders. Since antennas are usually designed assuming that they are isolated and mounted on flat ground planes, the actual pattern/performance of the antenna can significantly differ from their theoretical designs. Hence, for the safe operation of the aircraft, it is vital to predict the electromagnetic performance of each system in the presence of others.

With the increasing number of airplanes in the sky, avoidance of mid-air collisions has assumed new importance [2]. To this end, the Federal Aviation Administration has mandated that all aircraft that can carry more than 30 passengers be fitted with an advanced Traffic-alert Collision Avoidance System (TCAS) [3]. The TCAS is basically a direction finding and tracking radar, that determines the bearing of a nearby aircraft from a signal received from that aircraft. There are a number of tracking radars described in the literature; however, due to cost, space, weight as well as other constraints, only a few of these can be used in airborne applications [4].

The basic operation of the TCAS is as follows: The TCAS equipped airplane transmits a directional query signal. This query triggers a transponder on nearby airplanes, if so equipped. The digitally coded, transponder return signal is received by the TCAS and processed to detect the presence of an intruder. It may also estimate the bearing, velocity etc., of the other airplane. For convenience, the TCAS equipped aircraft will be referred to as the *own* airplane and the transponder equipped nearby airplane will be called the *intruder*.

Presently, there are three generations of the collision avoidance systems, named TCAS I, II and III respectively. The TCAS I system, the oldest, could only inform the pilot about the presence of other aircraft in his vicinity. It could not advise the pilot of evasive maneuvers to take to avoid a potential collision. The TCAS II system, currently in the production phase, has conflict resolution logic, which can suggest that the pilot should climb or dive [5]. The most recent system, the TCAS III has the ability to determine the bearing of the intruder aircraft accurately, and can issue to the pilot an advisory to bank left or right in addition to climb or dive. This is possible because, along with the bearing, the TCAS III system can also determine the altitude, velocity, and distance of the intruder from the transponder response. More information about these systems can be found in [6],[7],[8].

There are many factors that adversely affect the performance of the TCAS in estimating the bearings of surrounding aircraft. Even though it is not very hard to predict the bearing of an intruder under ideal design conditions, it is much more difficult to predict the performance of the same system when the antenna is mounted on an actual aircraft. This is due to the distortion of the radiation pattern by the curvature of the fuselage, scattering by the wings, engines, horizontal and vertical stabilizers as well as other nearby antennas located on the skin. The cost of making full scale measurements and evaluating these systems under actual flight conditions is very high, time consuming, and error prone. Therefore, there is a need for alternative methods to study the performance of various systems.

One common method is to use scale models to make measurements [9]. This is inflexible in that one can not study all possible locations for a TCAS antenna on the fuselage of various aircraft. Another possibility is to use computer models to calculate the radiation patterns in the near or far field, and process the signal on a computer. The latter method is adopted here, and in the succeeding pages, the TCAS system performance is evaluated under various adverse conditions.

1.2 Synopsis

In this report, two different TCAS antennas are studied in detail. They are classified based on the operation. These are:

1. Comparison of Relative Amplitude system (CRA).

2. Spiral Phase Antenna system (SPA), and

The antennas for both systems consist of a four element circular array of monopoles; however, their operation and their performance in the presence of nearby scatterers is quite different. The CRA TCAS finds the bearing by comparing the amplitudes of the received signals; whereas, the SPA TCAS determines the bearing by using only the phase information contained in them. In this work, three main topics are covered:

- Modeling isolated TCAS antennas on aircraft.

- Simulation of TCAS performance in the presence of nearby antennas.

- Modeling of engine to better account for its effect on the TCAS.

Chapter 2 introduces the two systems. Their operation, modeling the antennas and the issues involved in modeling their performance are discussed. Models for the CRA and the SPA TCAS systems are developed. These are used in conjunction with the high frequency models of various airplanes. The radiation patterns are

obtained using the airborne antenna code, called NEWAIR3, based on the uniform geometric theory of diffraction [10],[11],[12]. The impact of various scatterers on the TCAS is characterized by the *bearing error*, defined as the difference between the system computed bearing and the actual bearing of an intruder. Simulation of the TCAS and computation of the bearing over all azimuth results in a bearing error curve. Under ideal conditions, the bearing error is zero. Due to the scatterers and other antennas on the airframe, which distort the received signals, this is not the case. The magnitude of the error indicates the relative effect of various scatterers on the TCAS [13],[14]. The salient features and properties of the error curves are also discussed in Chapter 2.

In Chapter 3, models are derived for different airframes and error curves are computed for each TCAS antenna at various positions on the fuselage. The error curves are then used to compute the standard deviation of the bearing error in a specified angular sector, which is used as a figure of merit to evaluate the performance of the TCAS at that location. It can be either used to compare the two systems TCAS on the same fuselage at two different locations or the same system on different airframes at similar locations. Three airplanes were chosen: Boeing models 737-300, 747-200 and 727-200. The variation of the standard deviation of the bearing error as a function of distance from the nose are presented. The curves of standard deviation versus the location on the fuselage are provided for both the top and bottom mounted SPA and CRA antenna systems [15]. It is shown that the various aircraft scatterers play an important role in the determination of the *angle of arrival* (AOA) errors. The need for a better engine model is demonstrated for some cases, specifically when an engine is directly illuminated by the TCAS.

The effect of two nearby antennas mounted aft of the TCAS antenna at optimum location on the behavior of the TCAS is considered next in Chapter 4. The scattering from the blade antennas in the vicinity were included in the patterns of the TCAS antenna via superposition [16]. Two representative antennas were chosen for this

study; one a VHF blade, and the other an L-band blade. Modeling methods for these two antennas are different and hence are discussed separately. First, using a moment method analysis, the scattering fields were computed [17]. Next, using an antenna synthesis procedure based on the method of least squares, models for the blade antennas were developed. It is found that these nearby antennas have a bigger impact on the SPA TCAS than the CRA system. This is especially true in the forward directions. The reasons for this phenomenon are discussed, citing examples from the study on the Boeing 737-300 [15].

Chapter 5 discusses the modeling of the aircraft engine as a circular waveguide cavity. The waveguide was terminated using a perfectly conducting flat plate. The patterns of the scattering from the engine were obtained via modal techniques and then superimposed on the patterns of the TCAS [18],[19],[20]. It was discovered that the engine model consisting of flat plates overestimates the error in certain regions and under-estimates in others. The waveguide model leads to a more uniform bearing error. It is also seen that the CRA is affected much less than the SPA system. The performance of the system can be improved slightly by moving the antenna forward. The advantages and disadvantages of modeling the engine as a terminated waveguide versus a closed rectangular box are discussed.

The results are summarized in Chapter 6. Guidelines are devised to locate the TCAS antenna on the fuselage without compromising the performance in the presence of various scatterers. The results indicate that for best performance, one should place the TCAS antenna towards the forward portion of the fuselage. For forward look angles, it is found that the CRA TCAS performs better than the SPA system under all situations considered in this report. Consequently, installation of the CRA antenna poses fewer difficulties than the SPA antenna. This could be an important factor when the space available on the fuselage is small or there are other nearby scatterers. Based on results obtained so far, antenna placement on other aircraft is

briefly considered. Finally, some techniques that might improve the performance of the TCAS antennas in general are suggested.

Chapter 2

Operation of TCAS

2.1 Introduction

Two angle of arrival systems are introduced in this chapter. They are classified as:

- Comparison of Relative Amplitude (CRA) system. The CRA TCAS operates by comparing the amplitudes of the received signals via different beams. The phase information is normally ignored.
- Spiral Phase Antenna (SPA) system. A competing TCAS system, that finds the bearing of the intruder from the phase of the received signals. This algorithm usually discards the amplitude information.

The TCAS antennas are modeled and the systems simulated on a digital computer. The properties of the the two systems are explored using the bearing error transfer functions. Some bearing error curves for the CRA TCAS are found to have discontinuities at some specific angles. It is discovered that the SPA TCAS is more sensitive to nearby scatterers than the CRA system.

2.2 Comparison of Relative Amplitude System

The CRA TCAS employs a four element circular array. This array transmits a beam in one of four selectable directions. The array is mounted on the fuselage and aligned

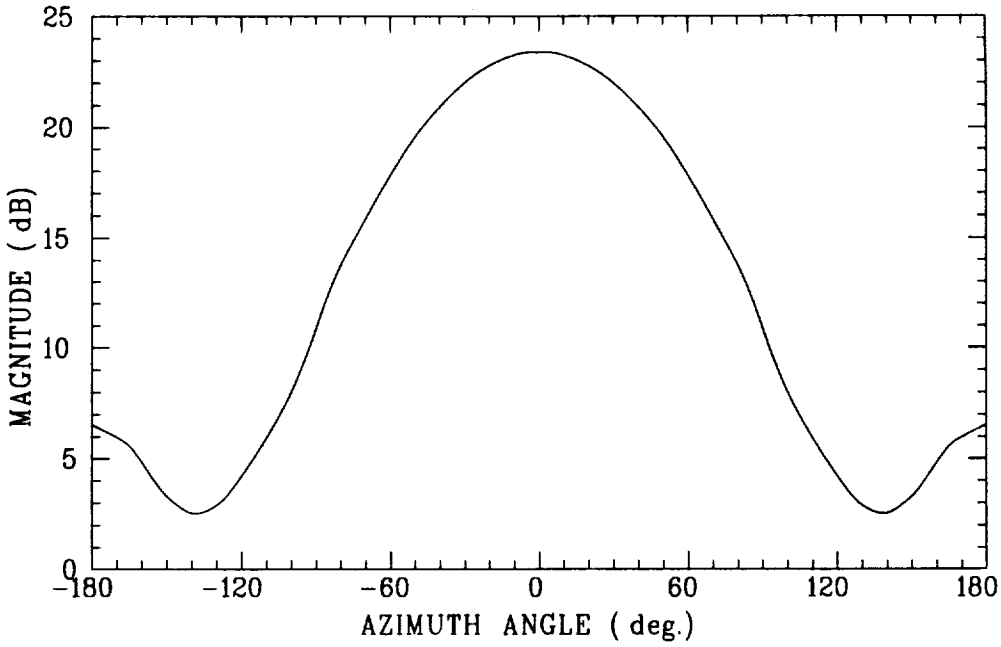

Figure 2.1: Typical directional interrogation beam for the amplitude TCAS.

in such a way that the beams are directed in the 0°, 90°, 180° and 270° of relative bearing with respect to the forward direction. The beams have a 3-dB beamwidth of $90° \pm 10°$ for all elevation angles between $+20°$ and $-15°$. Note that 0° elevation corresponds to the standard azimuth pattern cut. A sketch of the desired receiver pattern is shown in Figure 2.1.

The frequency of transmission of the query signal is 1030 MHz. The received signal is received individually by each element of this antenna array at 1090 MHz. The magnitudes of the four received signals are then compared and the difference between the largest two computed. Comparison of this difference signal with similar values on a calibration curve yields the angle of arrival (estimated bearing of the intruder).

The TCAS antenna is modeled by four short z-directed monopoles on a flat ground plane as depicted in Figure 2.2. The current distributions on the monopoles are assumed to be sinusoidal. Let the excitation of the individual elements be given

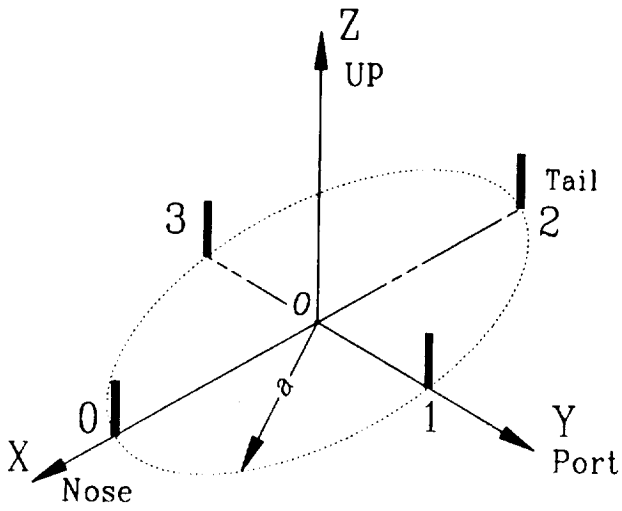

Figure 2.2: Geometry of the 4 element CRA TCAS model.

by

$$I_i = A_i e^{j\alpha_i} \tag{2.1}$$

where, I_i is the complex excitation, A_i is the amplitude, and α_i is the phase of element i, where $i = 0, 1, 2, 3$, and $j = \sqrt{-1}$. The elements are numbered counterclockwise from the X-axis as shown.

The far field antenna pattern $E_\theta(\theta, \phi)$ is the product of the element pattern $F(r, \theta, \phi)$ and the array factor $AF(\theta, \phi)$ such that

$$E_\theta(\theta, \phi) = F(r, \theta, \phi) \cdot AF(\theta, \phi) \tag{2.2}$$

where, the azimuth angle ϕ is measured counterclockwise from the forward direction (towards the nose), and θ is measured from the vertical as shown in Figure 2.3.

The element pattern of a dipole of length l or a monopole of length $l/2$ on a ground plane can be written as [21]

$$F(r, \theta, \phi) = \frac{j\eta e^{-jkr}}{2\pi r} \left[\frac{\cos\left(\frac{kl}{2}\cos\theta\right) - \cos\frac{kl}{2}}{\sin\theta} \right] \tag{2.3}$$

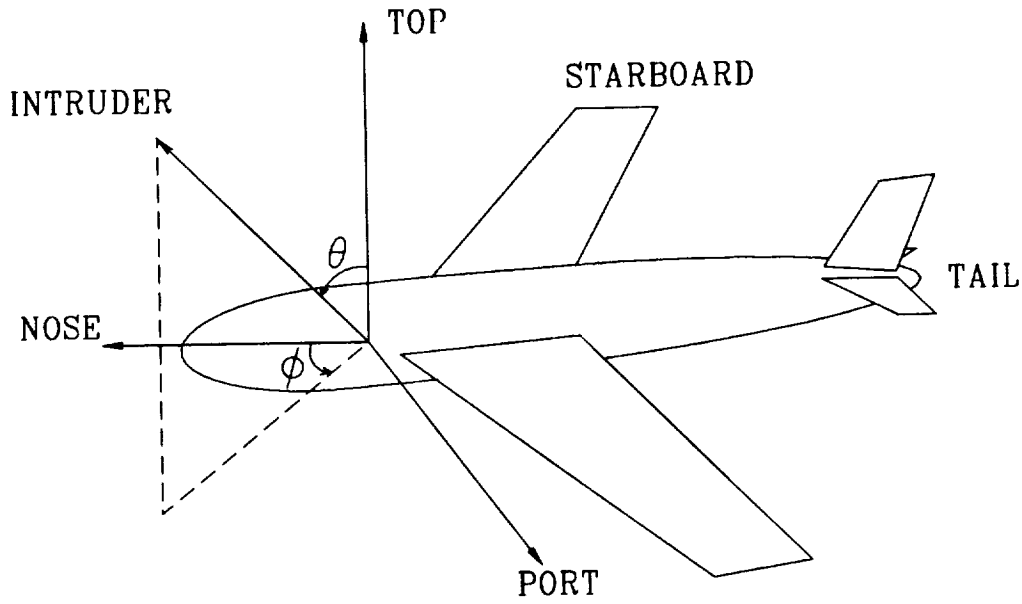

Figure 2.3: The aircraft coordinate system. Azimuth angle is measured counter-clockwise from the forward direction. Elevation angle is measured from the horizon.

and the array factor is given by

$$AF(\theta,\phi) = \sum_{i=0}^{3} A_i e^{j(\alpha_i + ka\sin\theta\cos(\phi-\phi_i))} \tag{2.4}$$

where, a is the radius of the array, and k is the free space wavenumber, and $k = 2\pi/\lambda$. $\phi_i = i\frac{\pi}{2}$ is the angular position of the i^{th} element, η is the impedance of free space, and (r,θ,ϕ) are the standard spherical coordinates.

Since the number of elements is small, the amplitudes are set to a constant value $A_i = A$, and only the phase of the excitation is modified so as to get a maximum in any one of the four directions given by $\phi_j = j\frac{\pi}{2}, j = 0,1,2,3$, corresponding to nose, port side (left), tail, and right (starboard), respectively. Also, in order to achieve a symmetric azimuthal pattern, the two elements perpendicular to the axis of the beam heading must have the same phase. From these conditions, for example, for a beam maximum in the direction of the nose ($\theta = \theta_0, \phi = 0°$), one possibility is to pick

$$\alpha_0 \;=\; \text{arbitrary} \tag{2.5a}$$

$$\alpha_1 = \alpha_0 + ka\sin\theta_0 \tag{2.5b}$$

$$\alpha_2 = \alpha_0 + 2ka\sin\theta_0, \qquad \text{and} \tag{2.5c}$$

$$\alpha_3 = \alpha_1. \tag{2.5d}$$

The weights were calculated for each beam heading ϕ_j, and $\theta_0 = 80°$, because this θ_0 corresponds to the elevation angle of most interest, namely 10°. These weights were then kept fixed in further calculations. To scan the space, one simply adjusts the phase distribution of the antenna elements.

The radiation patterns of the TCAS antenna in this synthesis, as well as other simulations were obtained by using a FORTRAN program called *NEWAIR3.* NEWAIR3 is based on the high frequency method, the Uniform Geometric Theory of Diffraction (UTD). This is sometimes referred to as the *aircraft code* or the *airborne antenna code.* The code can be used to compute the radiation patterns of short monopoles and slots on a curved body. The body is modeled by a composite ellipsoid, joined smoothly at the location of the antenna. Other structural features such as wings, tail etc. are simulated by perfectly conducting (PEC) flat plates. Details may be found in the literature [12, 11].

From a number of simulations with varying parameters of the array, a radius of $a = 2.28''$ and antenna length of $l = \lambda/4$ were chosen at the frequency of simulation 1090 MHz. The length of the antenna elements affects only the elevation plane patterns, and the effect is small for $l < \lambda/4$. As an example, the four beams were calculated on the fuselage of a Boeing 727-200 at a distance of $380''$ from the nose. The computer model consisted of only the fuselage. The beams are depicted in Figure 2.4 and the important properties are tabulated in Table 2.1. It is noted that the radiation characteristics are different for all four beams because of the effect of fuselage curvature.

The model for the operation of the amplitude system proceeds by first calculating the calibration or *lookup table.* For the CRA system, this consists of the difference of the dB magnitude of the received signals for the antenna mounted on the fuselage

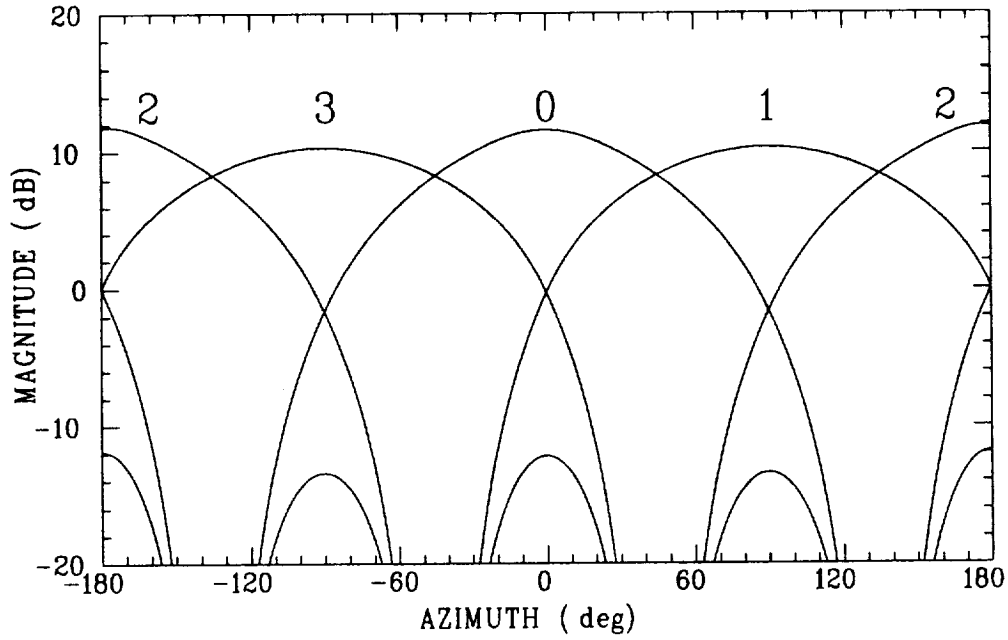

Figure 2.4: Four beams for top mounted CRA array located 380″ from the nose on the fuselage of Boeing 727-200.

Table 2.1: Parameters of the four CRA beams 380″ from the nose on Boeing 727 fuselage (radius = 2.28″).

Beam Bearing	Beamwidth (°)		Drop at 90° (dB)
	3 dB	10 dB	
Ideal	**90**	**180**	**10.00**
Nose	85.1	160.5	13.2
Port side	92.2	177.9	10.3
Tail	84.0	158.6	13.5
Starboard	92.2	177.9	10.3

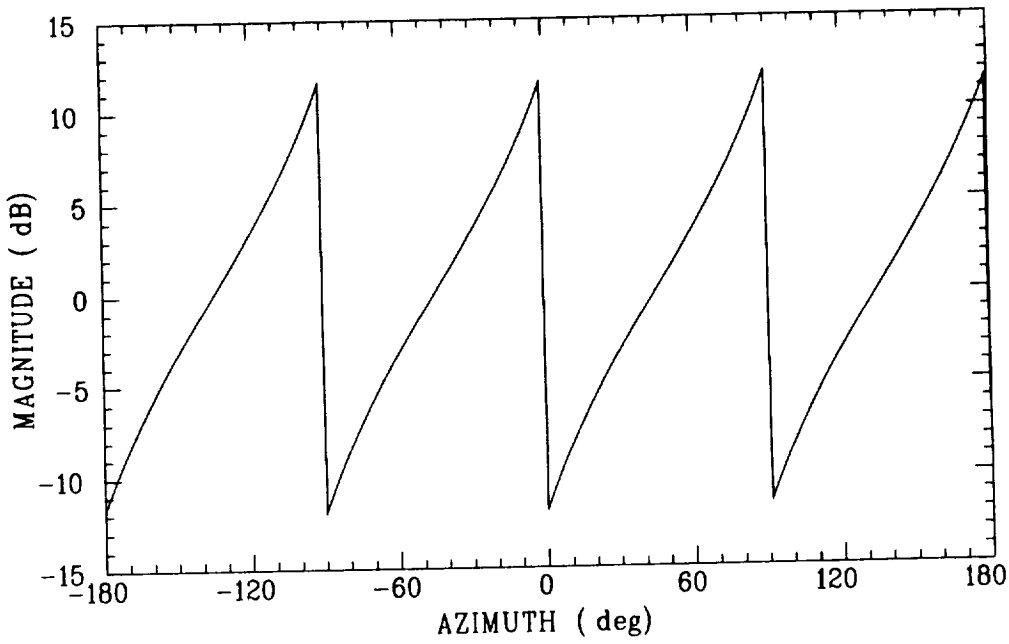

Figure 2.5: Creation of the CRA lookup table from the received signals.

of Boeing 727-200, with no other scatterers present. The received signal is simulated by calculating the four beams radiated by the TCAS array. By reciprocity, the transmitting and the receiving patterns of the array are identical [22]. The azimuthal space is divided into four quadrants, namely 0°–89°, 90°–179°, 180°–269°, and 270°–359°. The two beams with the largest amplitude in any given quadrant are known from the received signals, and one of these is selected as a reference signal. The other signal is subtracted from this reference signal to obtain a value that can then be used in the lookup table. Since there are four beam headings, there are four monotonically increasing sections of the lookup table as shown in Figure 2.5. The channel numbers of the two largest received signals are also stored. The list of channel numbers and the reference signal for all possible ϕ is given in Table 2.2.

Next, the radiation patterns of a TCAS antenna on an actual aircraft are computed taking into account the effect of various structures on the airframe, like wings, tail, engine, etc., which distort the signal transmitted/received by the TCAS array. These distortions are in the form of variations in amplitude and phase of the received

Table 2.2: Determination of the reference beams for the TCAS under ideal conditions.

ϕ (degrees)	Highest Channel	Next Channel	Reference Beam
0–44	0	1	
45–89	1	0	1
90–134	1	2	
135–179	2	1	2
180–224	2	3	
225–269	3	2	3
270–314	3	0	
315–359	0	3	0

Table 2.3: Location of intruder from received signals under ideal conditions.

Reference Beam #	Section of Lookup Table searched
1	0–89
2	90–179
3	180–269
0	270–359

signals. Again, the difference signal is computed and stored along with the channel numbers in what is defined as the *wing table.*

To calculate the bearing error, one starts with a given difference signal and the channel numbers from the wing table. From the channel number of the reference beam, the quadrant of the intruder can be determined. This is given in Table 2.3. That section of the lookup table is then searched for the same value of the difference signal as the received signal as depicted in Figure 2.6. The predicted bearing is found via linear interpolation when the difference signal lies between two points in the lookup table. The *bearing error* ϵ is defined as

$$\epsilon = \phi_d - \phi_a \tag{2.6}$$

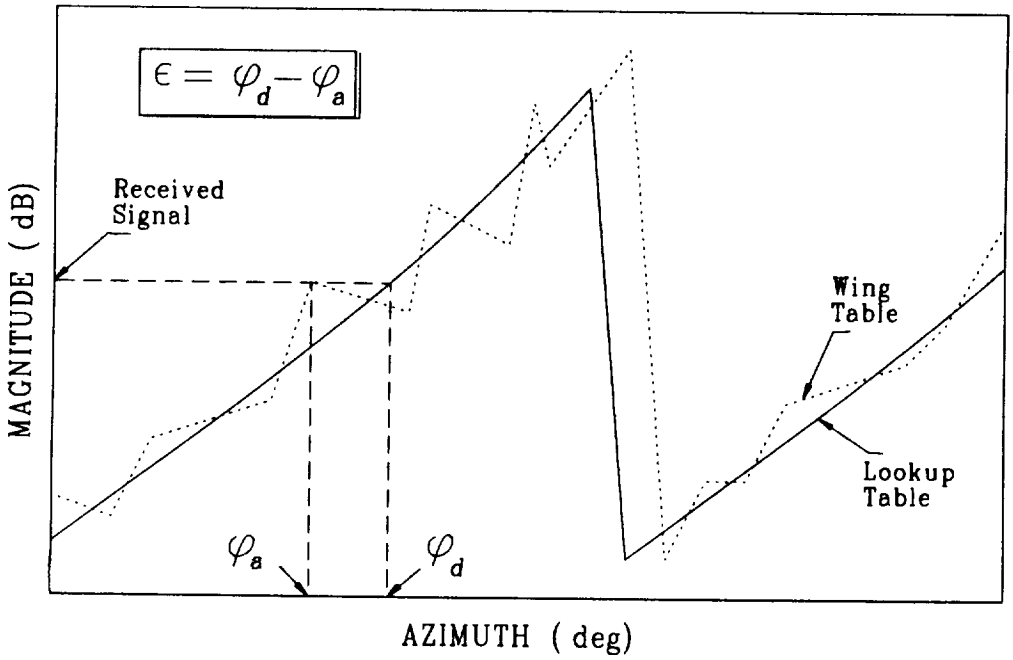

Figure 2.6: Calculation of bearing error.

where, ϕ_d and ϕ_a are the *d*etected (predicted) and *a*ctual azimuth angles of the intruder, respectively.

There are two sources of ambiguity/uncertainty that arise in this calculation. One type of ambiguity occurs when the difference signal lies outside the range of the lookup table. In this case, the two highest signals are a valid combination of beams, but the value of the difference signal is not within the boundaries of that section of the lookup table. This generates an *out of range* warning, and the error is calculated by setting the difference signal equal to the closest (extreme) value of the lookup table. The other source of error arises due to structural scattering, when two beams that have opposite bearings have the largest amplitudes in a given quadrant. This leads to an illegal combination of channels which leaves the processor with no lookup table to search. Hence, one can not estimate the bearing of the intruder. The error is then set equal to the previous value of bearing error and a *no lookup table* warning is issued.

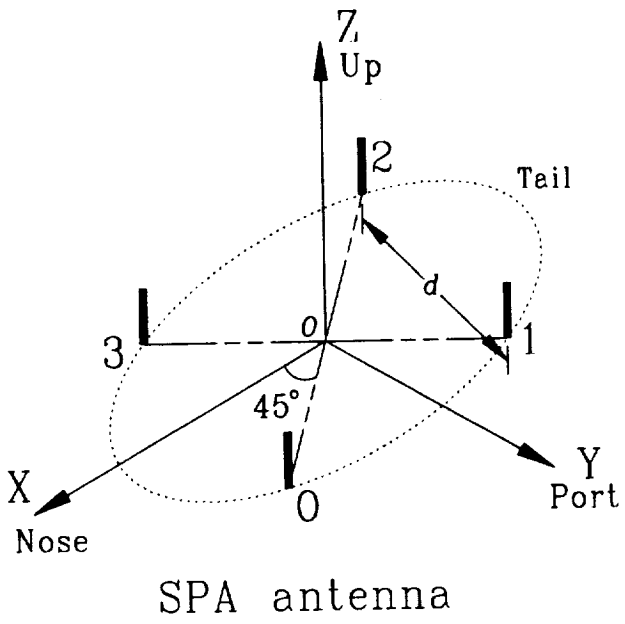

Figure 2.7: Geometry for the spiral phase antenna. Note the antenna alignment.

2.3 Spiral Phase Antenna System

As the name implies, the Spiral Phase Antenna (SPA) TCAS operates using the phase information contained in the received signal. Note that *spiral* refers to the phase of the received signal, as opposed to the type of antenna. The feasibility of using a spiral phase antenna for direction finding applications was first explored in [23]. The SPA array consists of four short monopoles arranged on a circle as shown in Figure 2.7. Note that this array is offset by 45° in comparison to the CRA antenna. As depicted, the positive x-axis points towards the nose of the aircraft and the distance $d = 2.709''$ corresponds to $\lambda/4$ at 1090 MHz.

The operation of the SPA TCAS is fairly simple. The TCAS equipped aircraft transmits an omnidirectional interrogation (query) signal. The transponder on the intruder responds by transmitting a reply at 1090 MHz, which is received by each element of the TCAS array.

For modeling purposes on the digital computer, the received signals are simulated by transmitting signals at 1090 MHz. In contrast to the CRA antenna, all monopoles

of the SPA array are excited with exactly the same amplitude and phase in the airborne antenna code. Sum (Σ) and difference (Δ) signals are generated according to:

$$E_\theta^\Sigma = \sum_{i=0}^{3} E_{\theta i} \qquad \text{and} \tag{2.7a}$$

$$E_\theta^\Delta = (E_{\theta_0} - E_{\theta 2}) + j(E_{\theta 3} - E_{\theta 1}) \tag{2.7b}$$

where, $E_{\theta i}, i = 0, 1, 2, 3$ are the complex received signals associated with the four elements of the antenna array at some azimuth angle.

Consider four monopoles of length $l/2$ on a ground plane, arranged as shown in Figure 2.7. The pattern is still described by Equations (2.3) and (2.4). For the SPA antenna, the distance between adjacent elements is $d = \lambda/4$. Hence the radius a of the array is given by

$$a = \frac{\lambda}{4\sqrt{2}}. \tag{2.8}$$

For the SPA system, $I_i = A$ is constant. Hence, from Equations (2.7), one finds that

$$\begin{aligned} E_\theta^\Sigma &= \sum_{i=0}^{3} A e^{jka\sin\theta\cos(\phi-\phi_i)} \\ &= 4A\cos\left(\frac{\pi}{4}\sin\theta\cos\phi\right)\cos\left(\frac{\pi}{4}\sin\theta\sin\phi\right) \end{aligned} \tag{2.9}$$

and

$$E_\theta^\Delta = 2jA\sin\left(\frac{\pi}{4}\sin\theta(\cos\phi+\sin\phi)\right) - 2\sin\left(\frac{\pi}{4}\sin\theta(\cos\phi-\sin\phi)\right) \tag{2.10}$$

In the lit region of the antenna, due to the size of the antenna array and distance to the intruder (who is in the far zone of the array), the amplitudes of all received signals are equal; they differ only in phase. The phase angle α is defined by

$$\alpha = \arg\left(\frac{E_\theta^\Delta}{E_\theta^\Sigma}\right) \tag{2.11}$$

In this alogorithm, the phase of the sum signal, E_θ^Σ serves as a phase reference. Note that α is monotonic in nature and hence can be used to unambiguously determine the angle of arrival of the received signal.

As is the case with the amplitude system, one must first generate a lookup table. This is done by calculating the radiation patterns of the TCAS antenna on the bare fuselage of a Boeing 727-200, located 380″ from the nose. The patterns are calculated at 10° elevation for a top mounted antenna and $-10°$ for a bottom mounted antenna as before. The amplitude and phase of the sum and difference beams for a top mounted antenna at the above location are illustrated in Figures 2.8 and 2.9, respectively.

It is noted that the pattern origin is at the center of the array and hence the phase of the sum beam is constant over all azimuth. The phase of the Δ beam is approximately linear. The monopulse curve (lookup table) is shown in Figure 2.10, which also exhibits the monotonic, almost linear variation of phase. This phase curve is the calibration curve used in all further calculations involving the SPA TCAS. It remains the same even if one is modeling a different airplane.

Once the lookup tables have been obtained, the radiation patterns are calculated, taking into consideration, the scattering and distortion by various structures on the airplane. These monopulse curves are distorted due to scattering by the structures on the airplane and coupling from other nearby antennas, if present. As in the case of the amplitude system, the error curves are calculated for the locations, elevations and airframes of interest.

2.4 Results

Typical results are provided for the case of a top mounted TCAS on a Boeing 737-300 based on the algorithms described above. A scaled line drawing of the principal views of the Boeing 737-300 is illustrated in Figure 2.11. As seen, this aircraft has two engines mounted below the wings.

The computer model used for the top mounted antenna is shown in Figure 2.12. The engines were not included in the model because of their distance from the antenna and the shadowing of the electromagnetic rays by the fuselage. The engines

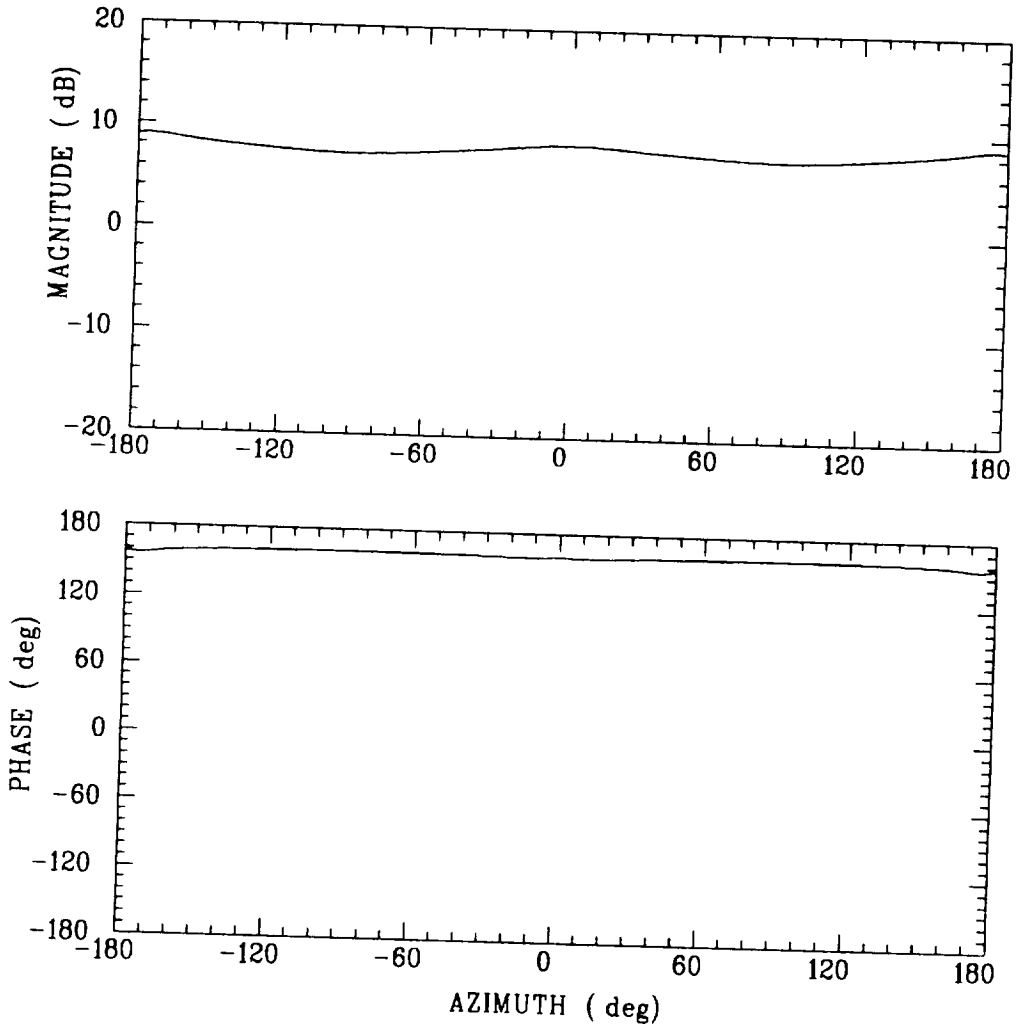

Figure 2.8: Amplitude and phase of sum (Σ) beam of an SPA antenna. The TCAS antenna was mounted on top of the fuselage of a Boeing 727-200, 380″ from the nose. Elevation = 10°.

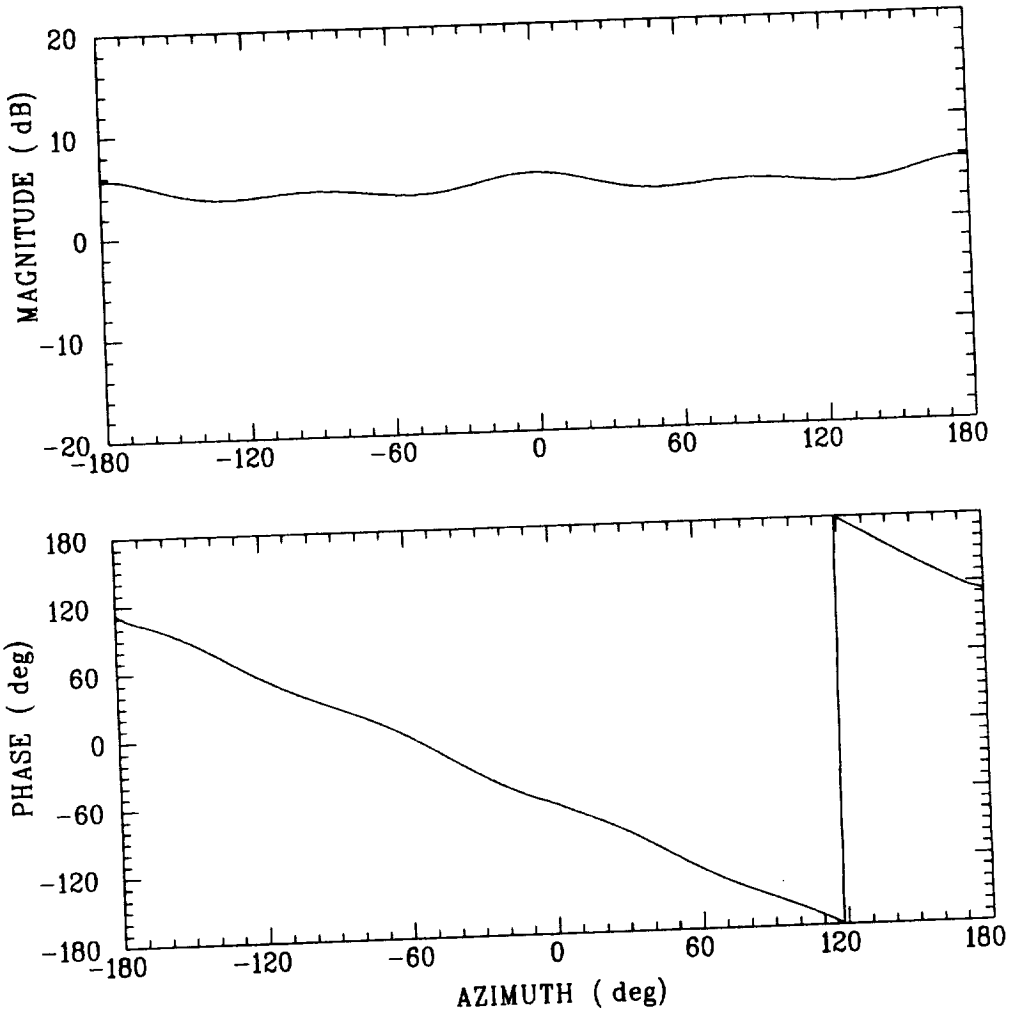

Figure 2.9: Amplitude and phase of difference (Δ) beam of the SPA antenna at the same location as in Figure 2.8.

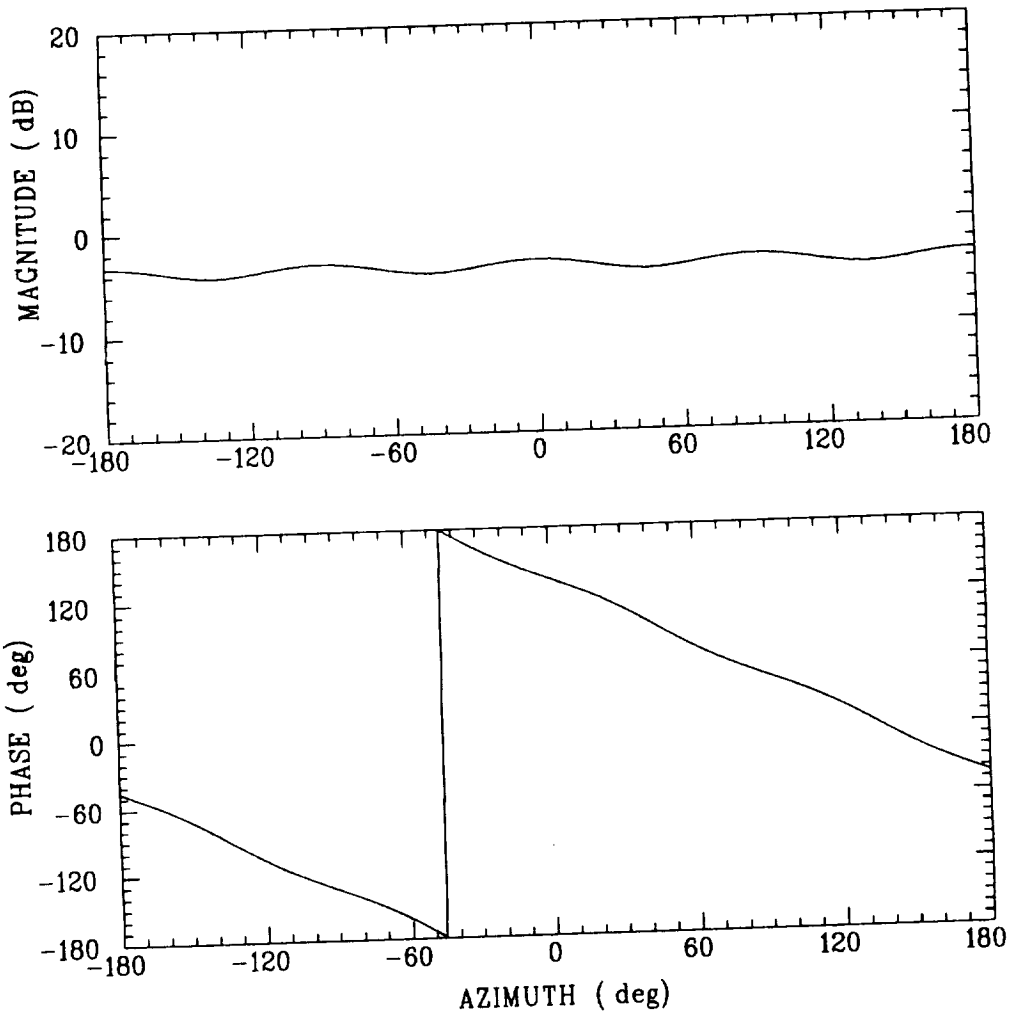

Figure 2.10: Lookup table for the SPA system. Only the phase information is used.

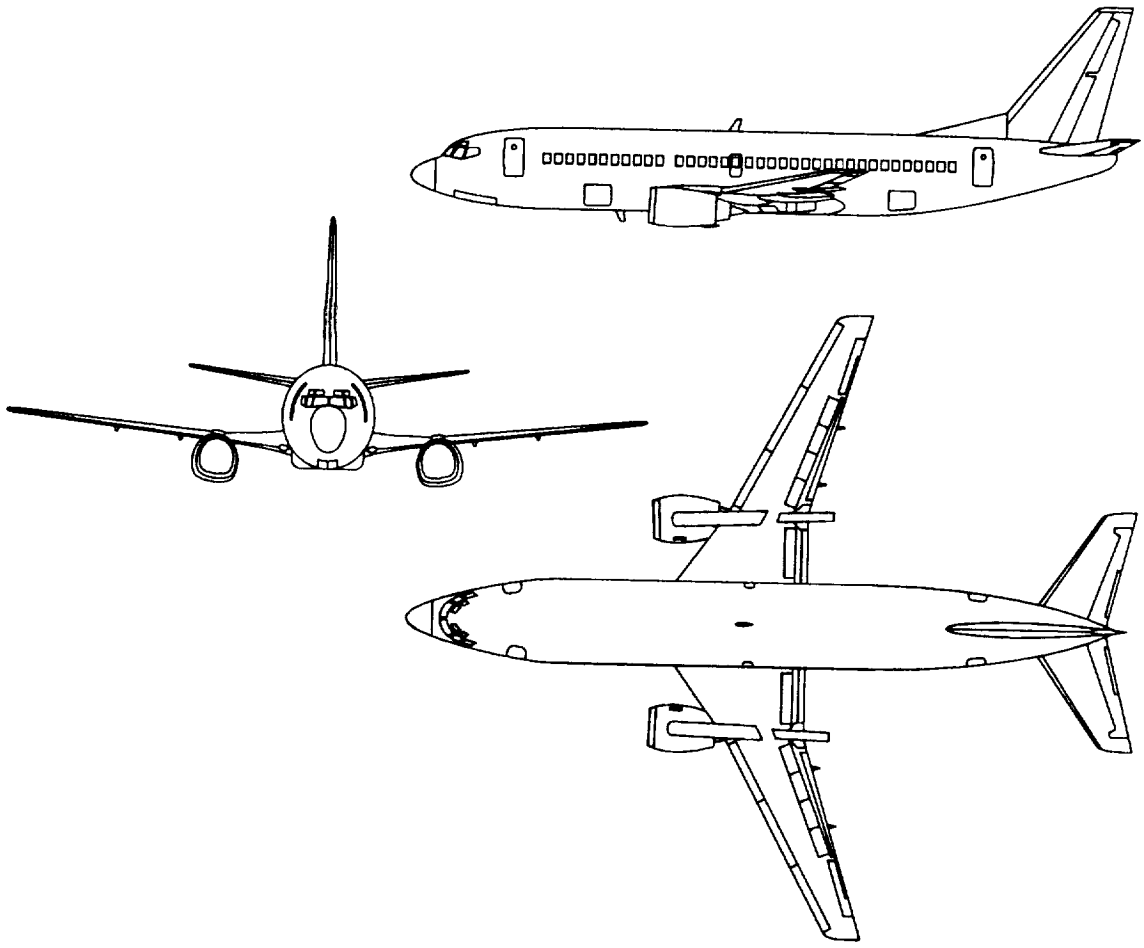

Figure 2.11: Scaled line drawings of the Boeing 737-300 aircraft.

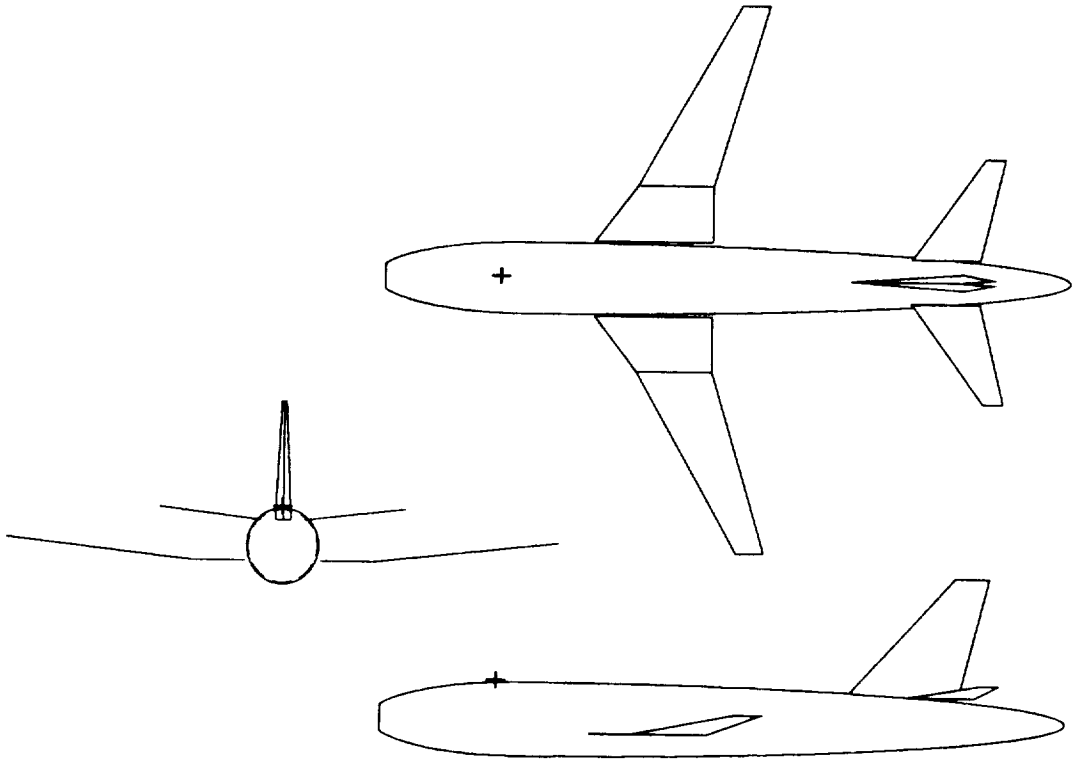

Figure 2.12: Computer model for Boeing 737-300 for a top mounted antenna. The antenna is located 289″ from nose.

do play an important role in the performance of the bottom mounted antenna. The effect the engine has on the TCAS is discussed in Chapter 5. The results presented here thus represent the typical errors one might expect on an aircraft fuselage when the engines are not visible. It is noted in passing that, normally, the contribution from the horizontal stabilizers is often ignored when the radiating element is a vertical monopole, as in this study.

The lookup tables for the CRA and SPA systems were generated on the bare fuselage of a Boeing 727-200. The antennas were located 380″ from the nose. The elevation of the receiver was 10° for the top mounted antennas. Error curves for the Boeing 737-300 aircraft are shown in Figures 2.13–2.18 for the TCAS antennas located about 289″ from the nose (location code 0240). These error curves cover elevations $-20°$ to 30° in 10° steps.

One notices that the error curves for the CRA and SPA systems are surprisingly similar, even though the bearing algorithms are completely different. This emphasizes the fact that the bearing error computed here is due to the body of the airplane; since it is the same for both systems, the error curves are also similar. The error is minimum around 10° elevation. This is because the lookup tables were computed at that elevation also. As the elevation goes higher or lower, the error tends to increase. This is especially pronounced in the error curves at elevations $-10°$ and $-20°$ where, the intruder lies in the shadow region of the TCAS antenna. One may also notice that the errors of the SPA system tend to be higher than the CRA system, because it is a phase system, and the received phase varies much more rapidly than the amplitude. Finally, due to the way in which the error is calculated, it is seen that the error curves of the CRA system are odd-symmetric ($\epsilon(\phi) = -\epsilon(-\phi)$).

It is seen from the top of Figure 2.17 and 2.18 that there are discontinuities in the error curves of the CRA system at angles where the beams switch, i.e., 0°, $\pm 90°$, and 180°. The reason for this has already been explained briefly. Here, let us attempt to elucidate by considering an example. The reader is referred to Figure 2.19, which

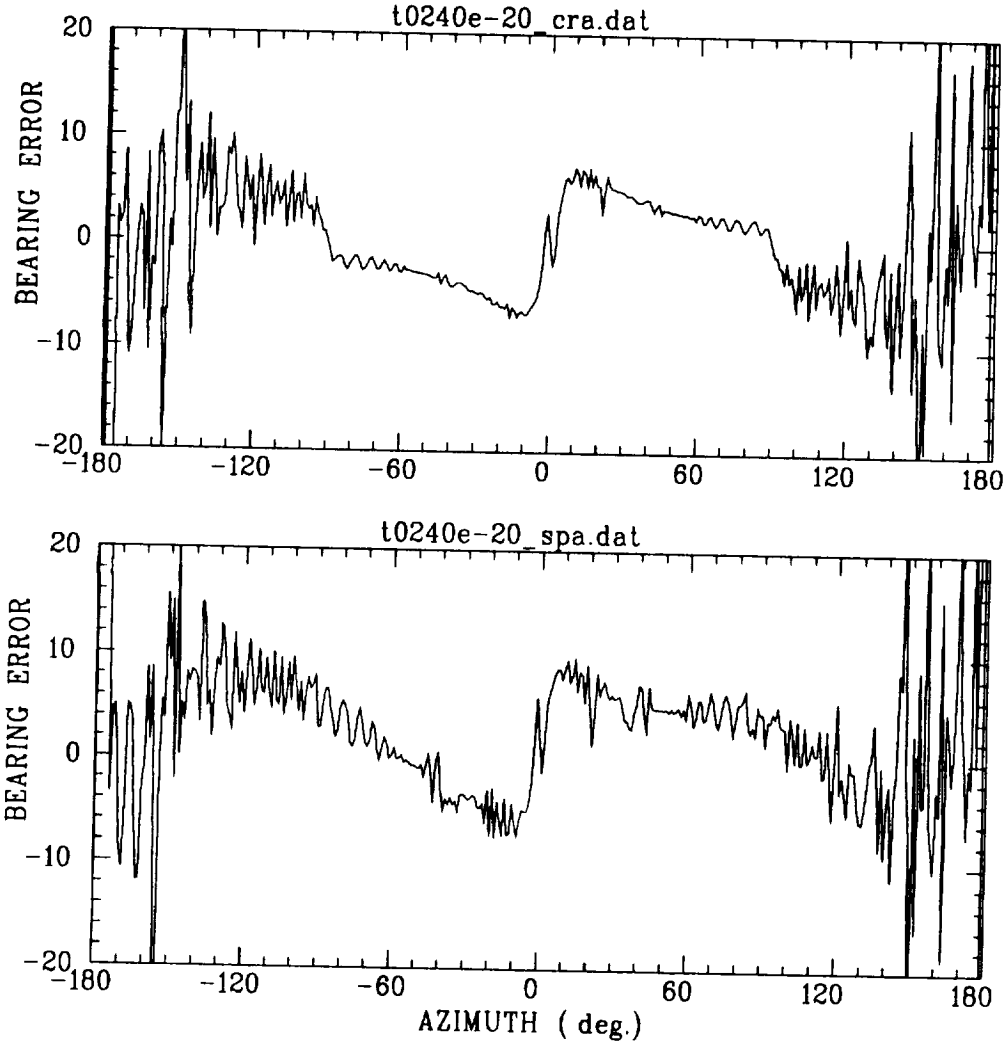

Figure 2.13: Error curves for CRA (top) and SPA (bottom) TCAS at $-20°$ elevation. The antenna was mounted on top of the fuselage of a Boeing 737-300 model about 289″ from the nose.

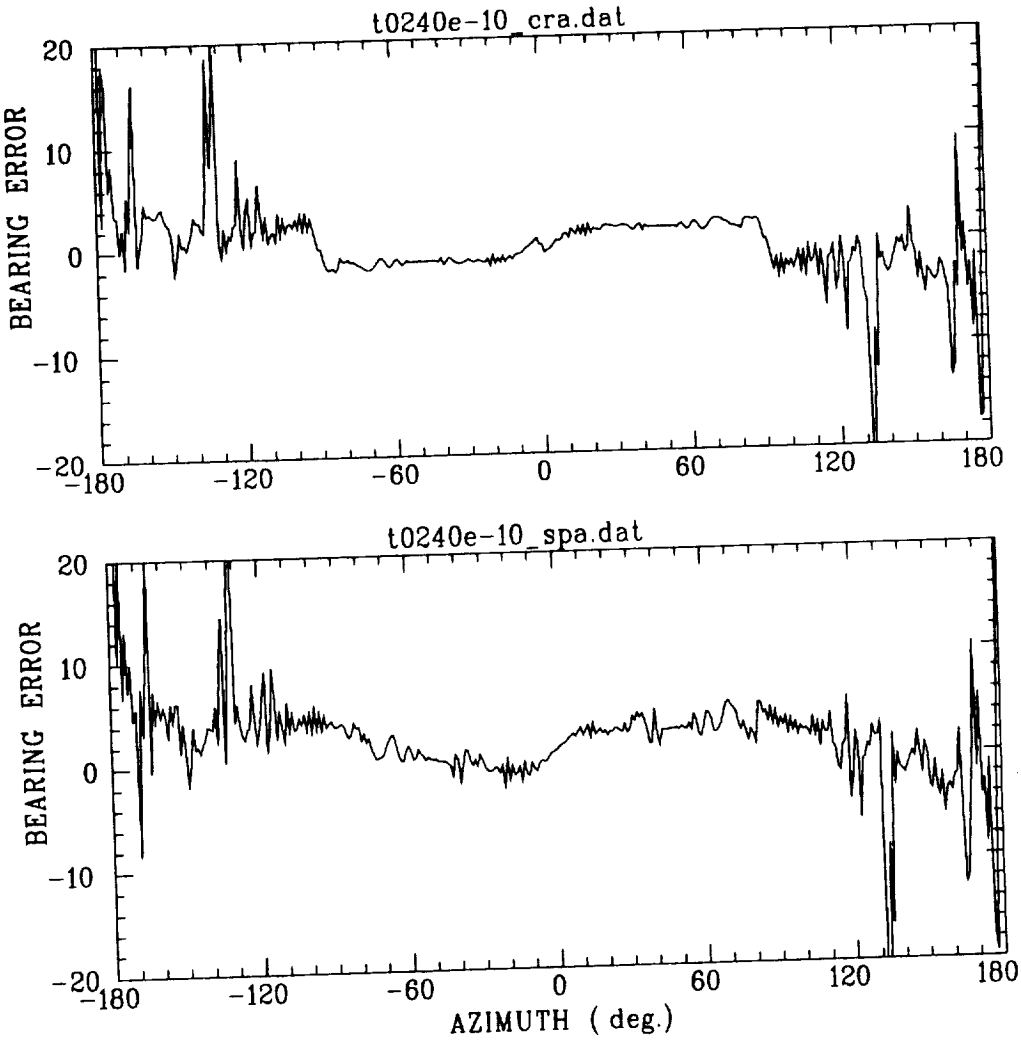

Figure 2.14: Error curves for CRA (top) and SPA (bottom) TCAS at $-10°$ elevation. TCAS setup same as Figure 2.13.

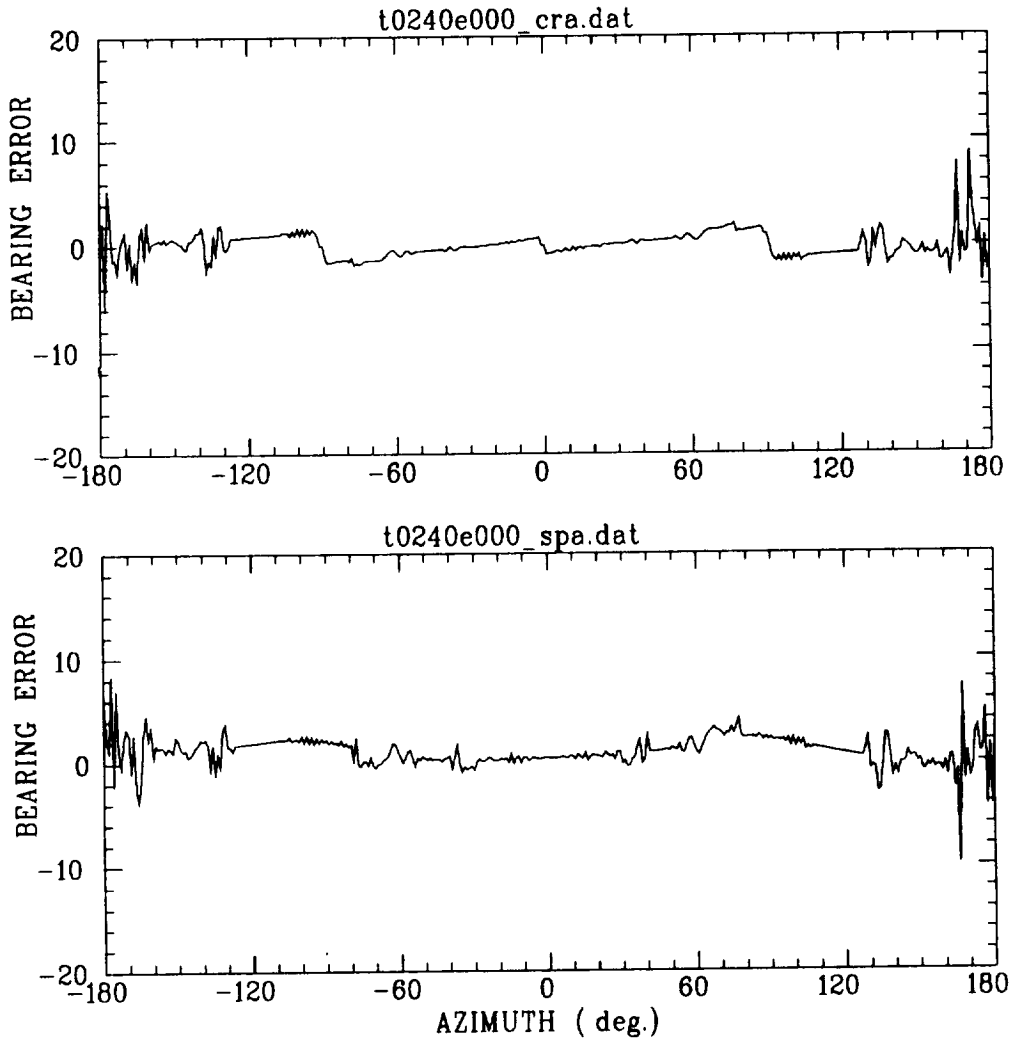

Figure 2.15: Error curves for CRA (top) and SPA (bottom) TCAS at 0° elevation. TCAS setup same as Figure 2.13.

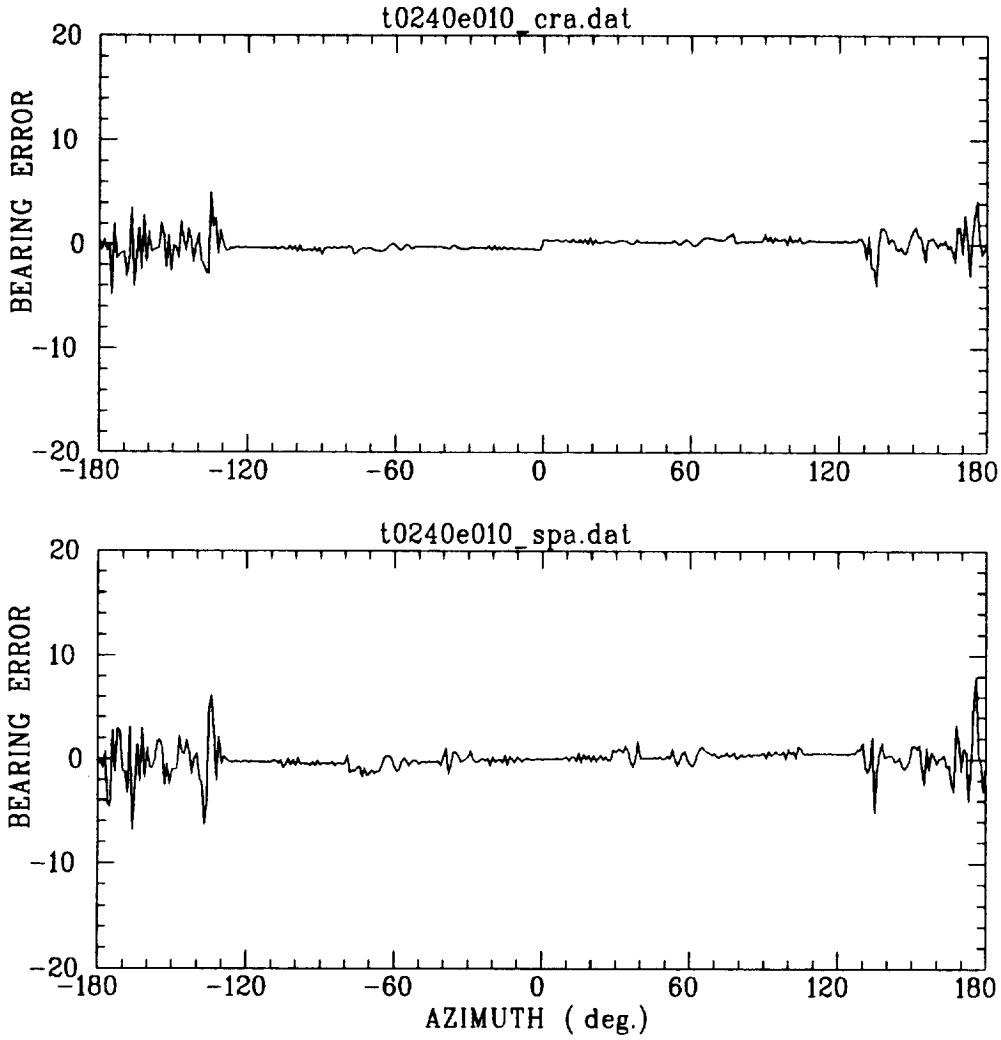

Figure 2.16: Error curves for CRA (top) and SPA (bottom) TCAS at 10° elevation. TCAS setup same as Figure 2.13.

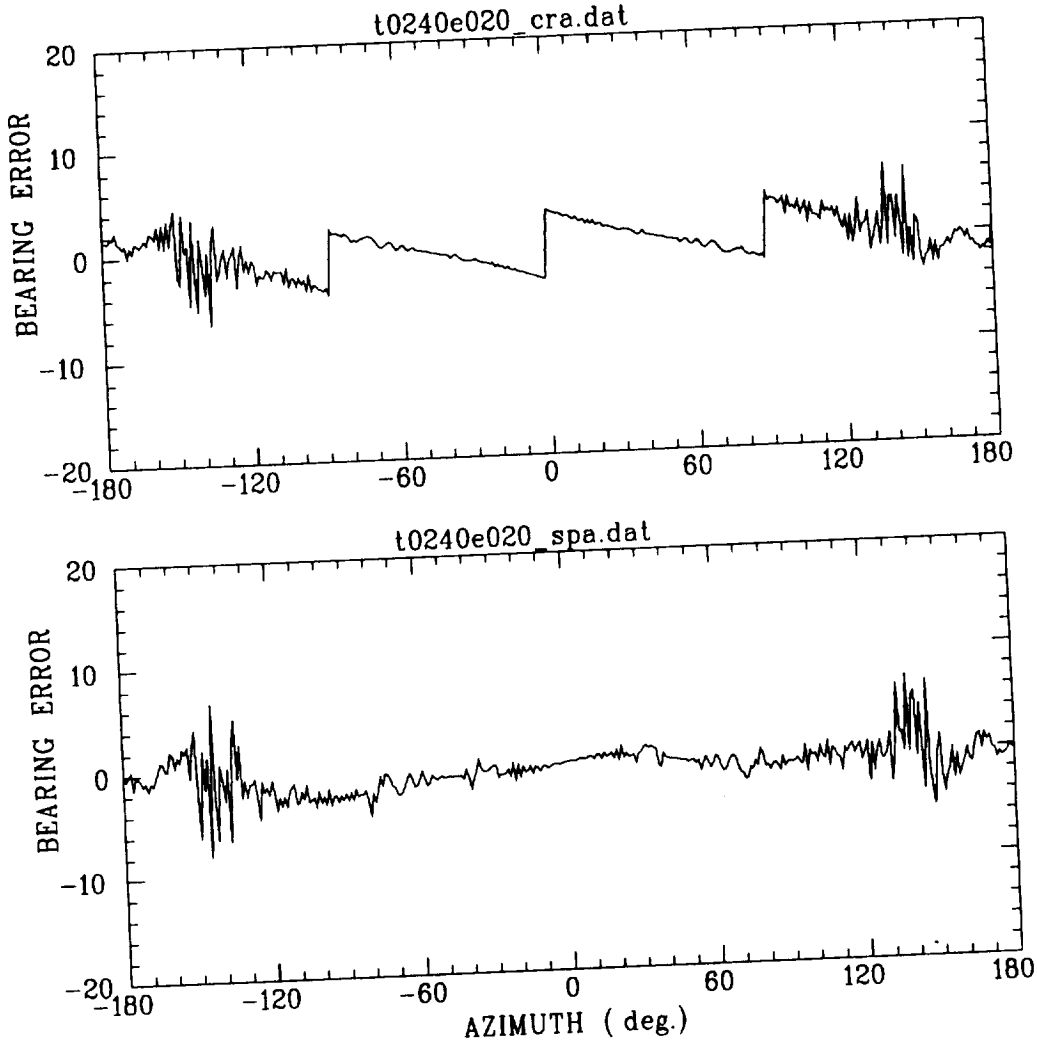

Figure 2.17: Error curves for CRA (top) and SPA (bottom) TCAS at 20° elevation. TCAS setup same as Figure 2.13.

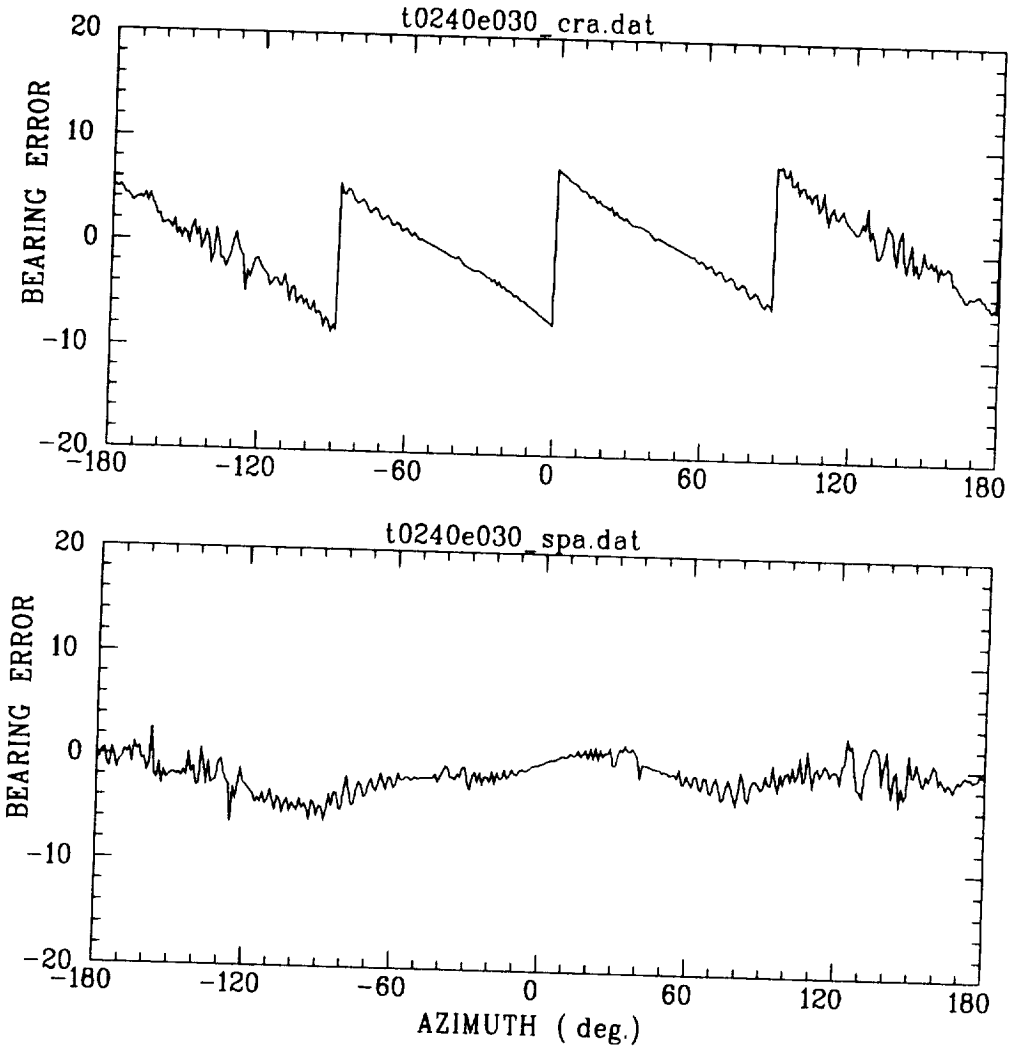

Figure 2.18: Error curves for CRA (top) and SPA (bottom) TCAS at 30° elevation. TCAS setup same as Figure 2.13.

is an enlarged view of the azimuth region 80° to 100°. The lookup table and wing table at 30° are depicted.

Case 1: $\phi_a = 88°$.

Let the actual bearing of the intruder be $\phi_a = 88°$. The channels of the two highest received signals are 0 and 1. From Table 2.3, it is determined that the intruder lies in the first 0°–90° quadrant. Searching the corresponding section of the lookup table, for the value of the received difference signal (9.4 dB), it is found $\phi_d = 82.6°$. Therefore, the error is $\epsilon_1 = \phi_{d1} - \phi_{a1} = -5.4°$.

Case 2: $\phi_a = 89°$.

Let the intruder be at $\phi_a = 89°$ for the same situation considered above. Now, the difference signal is -9.4 dB, and the two highest channels received are 1 and 2. Then, searching the lookup table to the right side in Figure 2.19, the detected position of the intruder is 97.2° to lead to an error of $\epsilon_2 = \phi_{d2} - \phi_{a2} = 8.2°$. Hence, the magnitude of the discontinuity is: $\epsilon_2 - \epsilon_1 = 13.6°$, and this is easily verified from either Figure 2.18 or 2.19.

Now, it is clear that the jumps in the CRA system occur due to the beam switching scheme and the slight change of the beams as a function of elevation. By a similar reasoning, it is deduced and verified that there are no discontinuities in some error curves, especially close to the elevation at which the lookup table was created. Further, the magnitude of the discontinuity increases with increasing elevation. This is probably one of the most serious drawbacks of the four element CRA system.

In all cases studied, and those presented here, it is observed that the magnitude of the error and the region of its occurrence correlate well with the relative locations of the TCAS antenna and the scatterer. This is seen in all figures, where, in the tail region, the error is much larger due to scattering by the vertical stabilizer.

The performance of both systems is similar in the absence of scatterers; however, when scatterers are present, the CRA tends to perform better than the SPA TCAS.

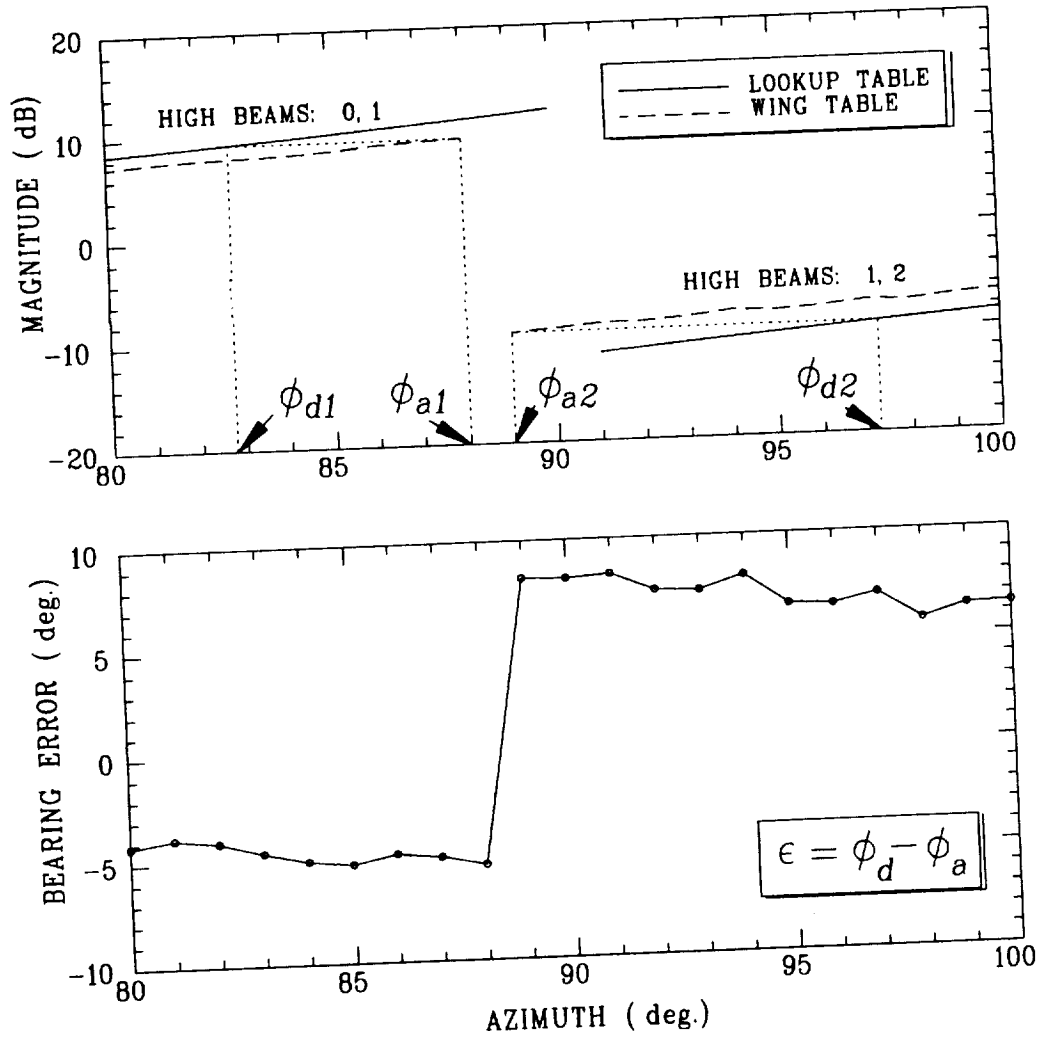

Figure 2.19: Illustration of the jumps in some CRA error curves. The section of the wing table corresponds to Boeing 737-300 airplane, antenna located 289″ from the nose at 30° elevation.

The implications of this phenomenon will become more apparent in the ensuing chapters.

Chapter 3

Optimal Location of TCAS

3.1 Introduction

One of the important applications of the Bearing Error Transfer Functions (BETF) is in the estimation of an optimal location for the top and bottom mounted TCAS antennas on aircraft. In this study, three representative commercial airframes are chosen, based on the location of engines and the number of planes in service. These are:

Boeing 727-200: Class-3 engine Turbojet, approximately 1300 aircraft in service.

Boeing 737-300: Class-2 engine Turbojet, about 800 aircraft in service.

Boeing 747-200: Class-4 engine Turbojet, approximately 180 aircraft in service.

The criterion used here is based on minimizing the standard deviation of the BETF over the angular sectors given below:

- Top Antenna: Forward sector, $-90°$ to $+90°$ azimuth averaged over $-10°$ to $+20°$ in elevation, in $5°$ steps.
- Bottom Antenna: 360°azimuth, averaged over $-20°$ to $0°$ elevation, in 5°steps.

For both top and bottom mounted antennas, the error curves are calculated over the whole azimuth with a resolution of $1°$ at a chosen elevation. The standard

deviation *top* (σ_t) and *bottom* (σ_b) antennas are defined by

$$\sigma_{t(b)} = \sqrt{\frac{\sum_{i=1}^{M_{t(b)}} \sum_{j=1}^{N_{t(b)}} (|\epsilon_{ij}| - \mu_{t(b)})^2}{N_{t(b)} + M_{t(b)} - 1}} \tag{3.1}$$

where $\mu_{t(b)}$ is the average value of the BETF averaged over the appropriate range of azimuth and elevation angles, that is,

$$\mu_{t(b)} = \frac{1}{N_{t(b)} + M_{t(b)}} \sum_{i=1}^{M_{t(b)}} \sum_{j=1}^{N_{t(b)}} |\epsilon_{ij}| \tag{3.2}$$

where ϵ_{ij} is the bearing error and i and j denote the i^{th} and j^{th} elevation and azimuth angles, respectively. It is noted that the absolute value of BETF is taken in the above equations because based on the definition of the bearing error, BETF can be positive or negative. $M_{t(b)}$ denotes the number of elevation angles for the top (bottom) mounted antennas, respectively. Likewise, $N_{t(b)}$ denotes the number of azimuth angles for the top (bottom) antennas, respectively. In this study, $M_t = 7$, $M_b = 5$, $N_t = 181$, and $N_b = 361$.

3.2 Boeing 737-300

The aircraft first considered is the Boeing 737-300. This airplane has two engines mounted below the wings as seen from the scaled line drawing of the principal views of the Boeing 737-300 in Figure 2.11. The engines do not play a significant role in the determination of optimum location for the top mounted antenna; hence, they can be ignored in the high frequency model. The best location for the TCAS antenna on the bottom, however, is sensitive to the distance from the engine; hence the engines must be included in the UTD model.

The airplane model used for the top antenna has already been introduced in Section 2.4. The performance of both the CRA and SPA systems is assessed by calculating the standard deviation curves. The standard deviation curve for these antennas is shown in Figure 3.1. The detailed statistics of each location may be found in Appendix A. The optimal location of the top mounted antenna is at 289″

and 229″ (location codes 0240 and 0180 respectively) for the CRA and SPA systems, respectively. It is seen that the standard deviation curves are fairly constant for both systems. This means that one may place the TCAS antenna anywhere from about 220″ to 520″ from the nose. The optimal locations are illustrated in Figure 3.2.

The bottom mounted TCAS antenna is considered next. The computer models used for the bottom mounted antennas on the Boeing 737-300 are shown in Figures 3.3 and 3.4. It is noted that the aircraft models are different for top and bottom mounted antennas and also for the forward and aft region of the airplane.

Unlike the top mounted antenna case, the engines play an important role in the determination of the optimal location because they scatter energy, and hence affect the accuracy of the TCAS system in estimating the AOA of the intruder. A worst case calculation is made in this chapter with the engines being modeled by closed boxes. A flat plate is placed at the front face of the engine to cover the inlet. It is important to note that this model of the engine will overestimate the specular reflection component of the scattered field. This leads to unnaturally high and low errors in the individual error curves. The standard deviation curves given in Figure 3.5 confirm this. It is seen that the standard deviation is largest in the region from 400″ to 600″ from the nose, which is also the region occupied by the engines. Thus, the optimum location of both systems occurs 95″ from the nose, which is also the farthest region forward of the engines. This location is shown marked in Figure 3.6. It may also be observed that the standard deviation decreases as the antenna is moved away from the engines. As in the case of the top mounted antenna, the overall performance of the CRA TCAS is better than the SPA.

3.3 Boeing 747-200

This aircraft, one of the biggest passenger carriers, poses some unique modeling problems. This is due to the presence of a cupola (hump) on top of the forward section of the fuselage, which approximately extends up to station 900. (See Figure 3.7).

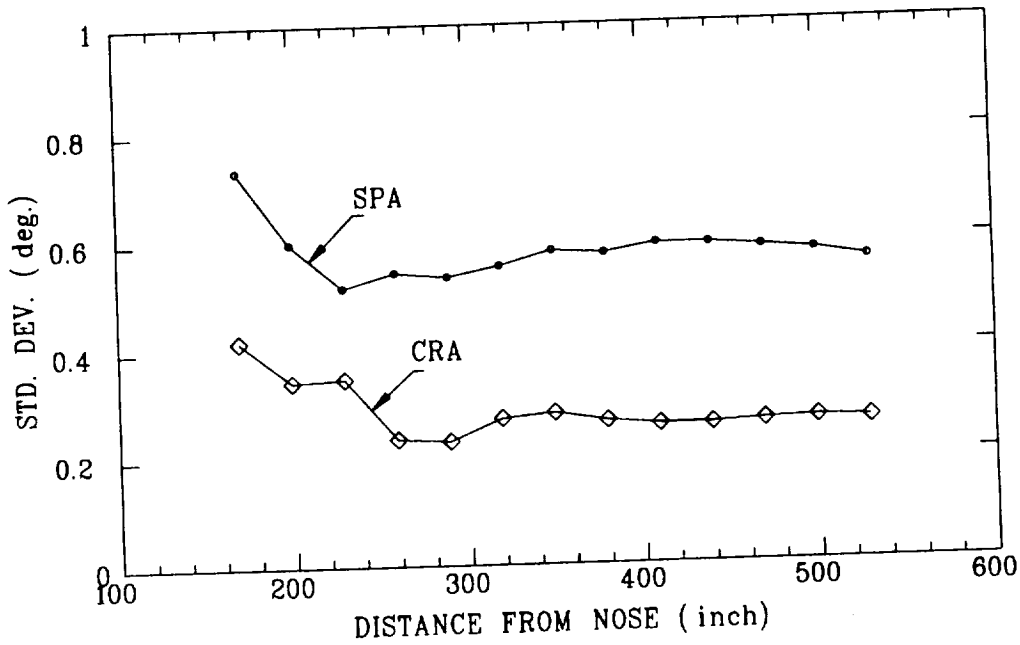

Figure 3.1: Standard deviation for top mounted TCAS array: Boeing 737-300.

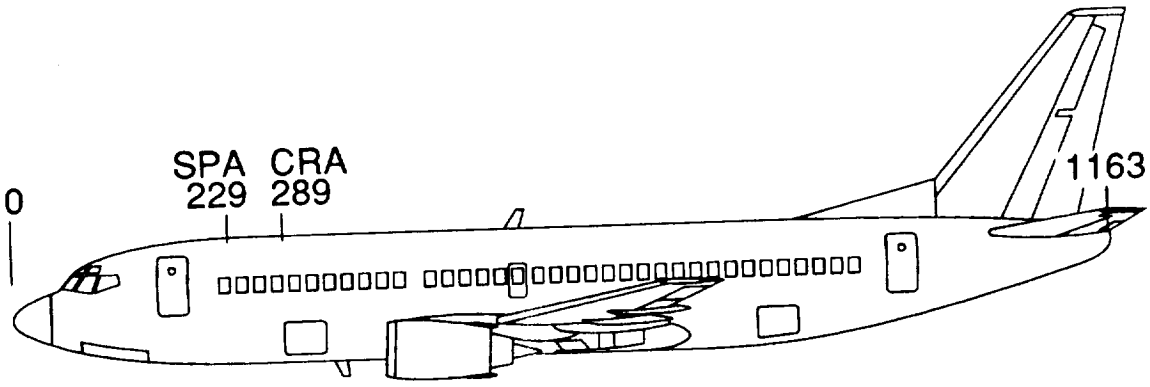

Figure 3.2: Location of optimum position for top mounted CRA and SPA arrays: Boeing 737-300.

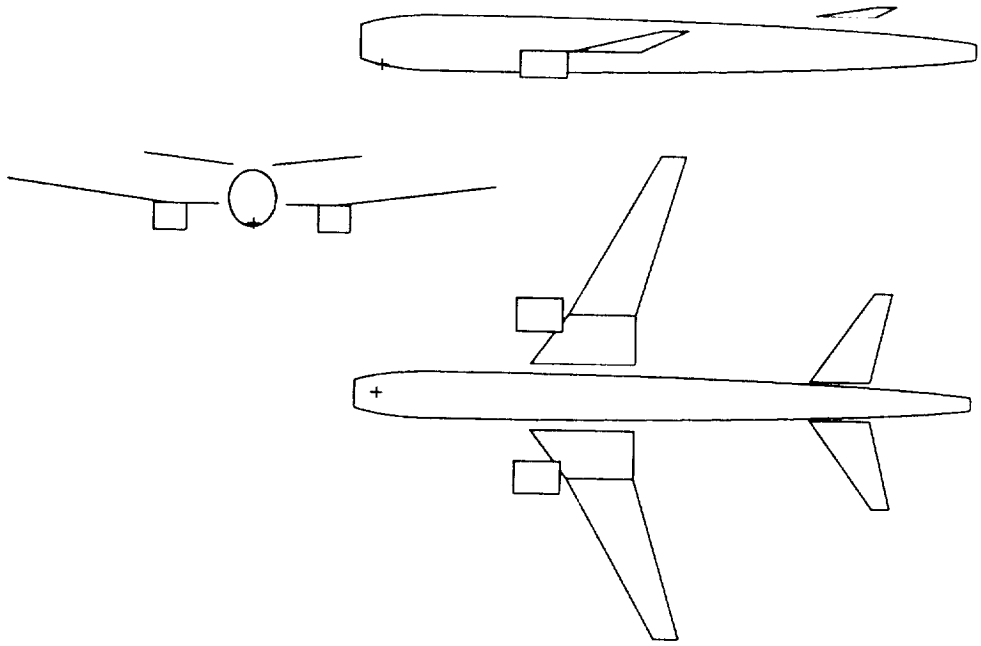

Figure 3.3: Computer model for Boeing 737-300 for a bottom mounted antenna in the forward region of the fuselage. Bottom view is shown.

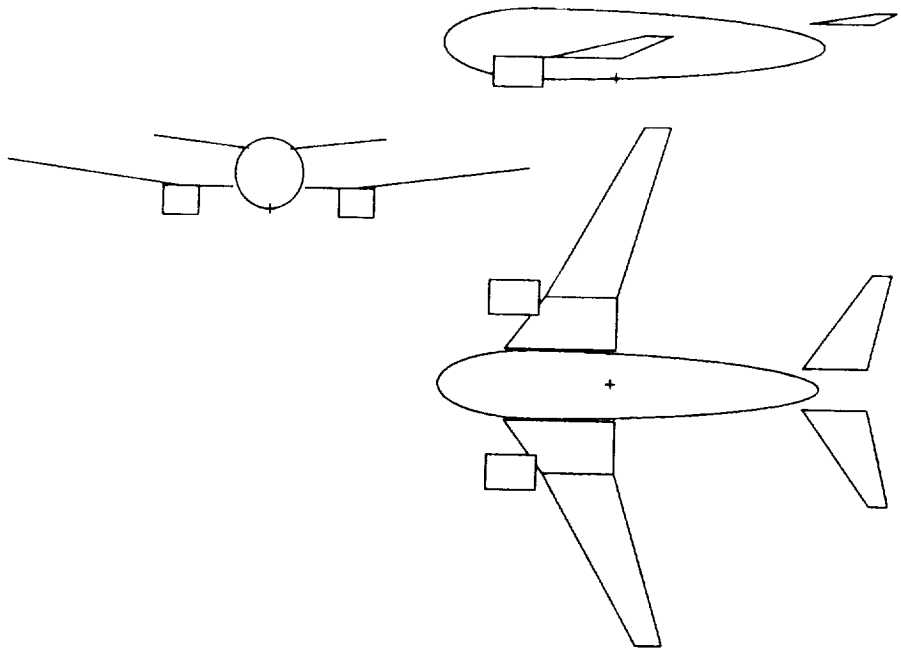

Figure 3.4: Computer model for Boeing 737-300 for a bottom mounted antenna located aft. Bottom view is seen.

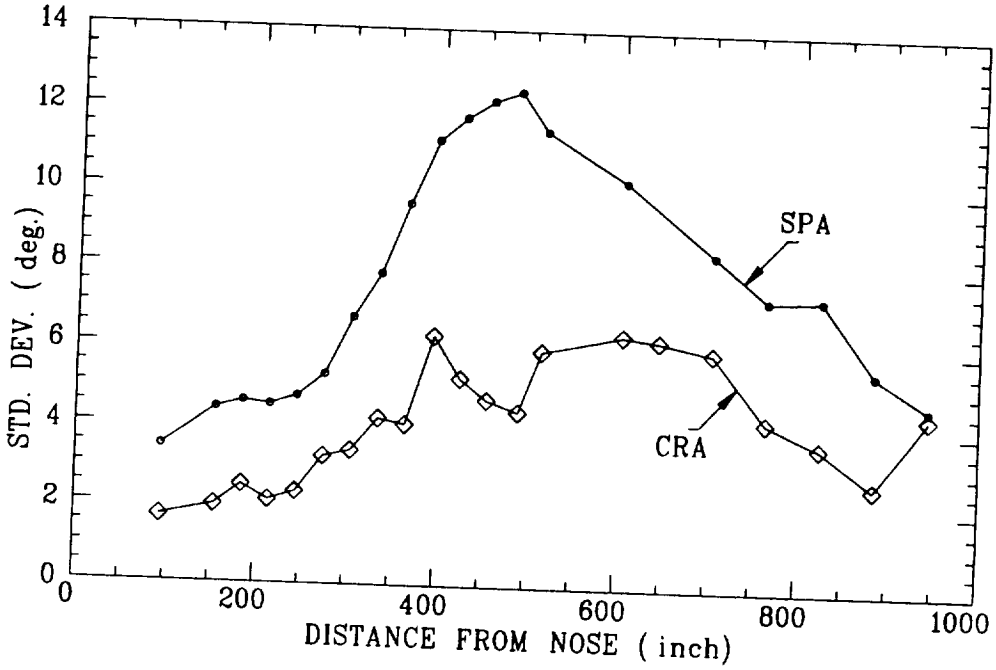

Figure 3.5: Standard deviation for bottom mounted TCAS array: Boeing 737-300.

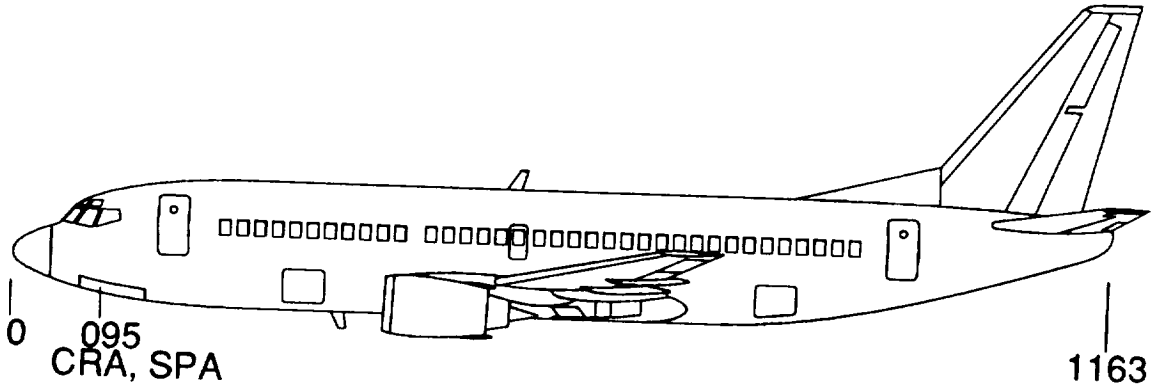

Figure 3.6: Location of optimum position for bottom mounted CRA and SPA arrays: Boeing 737-300.

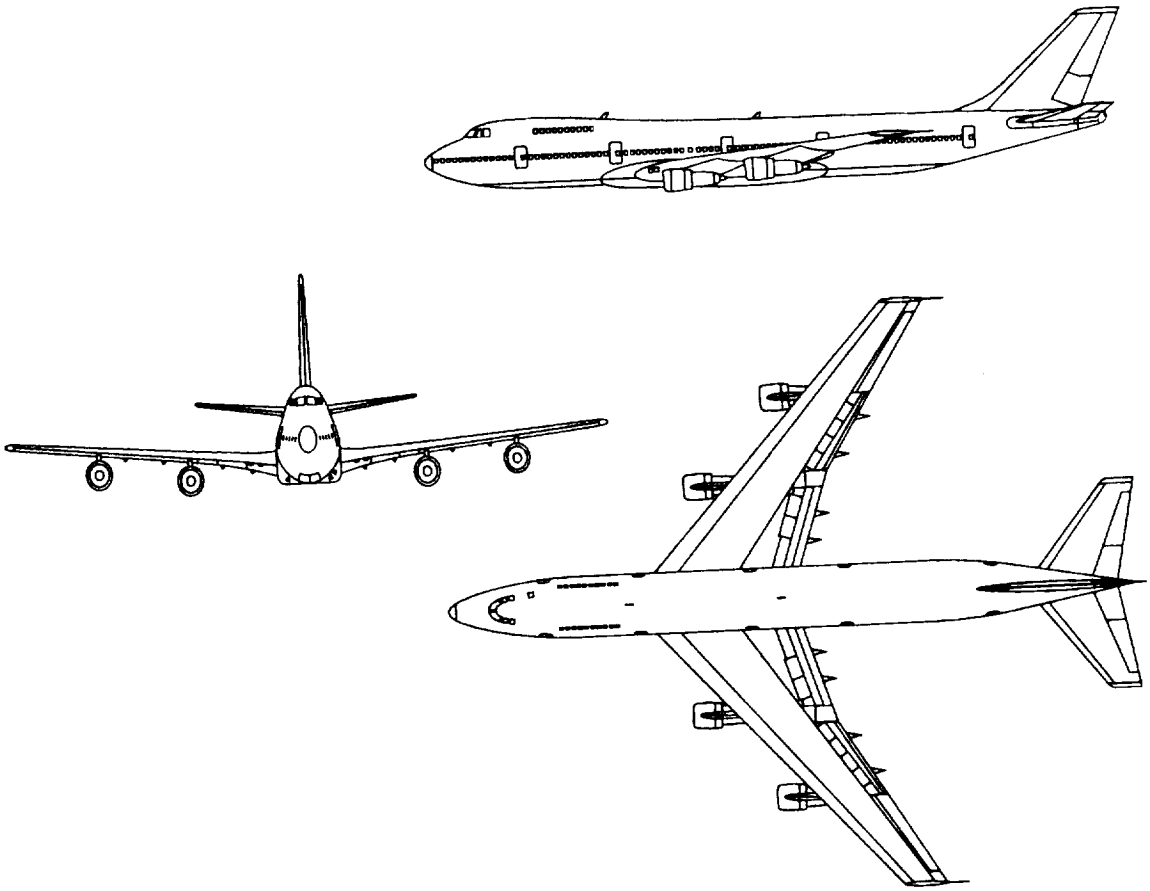

Figure 3.7: Scaled line drawings of the Boeing 747-200 aircraft.

Thus, a more sophisticated modeling scheme was adopted involving the Helicopter Antenna Radiation Program (HARP) [24]. The cross sections of the Boeing 747-200 fuselage were specified at various locations along the length, as well as the geometry of the wings, engines, tail, etc. The code then generates the high frequency computer model for the aircraft for an antenna located anywhere on the fuselage.

For obvious reasons, the model for the top of the fuselage for antennas mounted on or behind the cupola are different. Two representative models are shown in Figures 3.8 and 3.9. The part of the fuselage that is not modeled by the composite ellipsoid is approximated using flat plates. As mentioned earlier, the engines are not included in the models for the top mounted antenna because their effect is negligible on the radiation patterns of the TCAS.

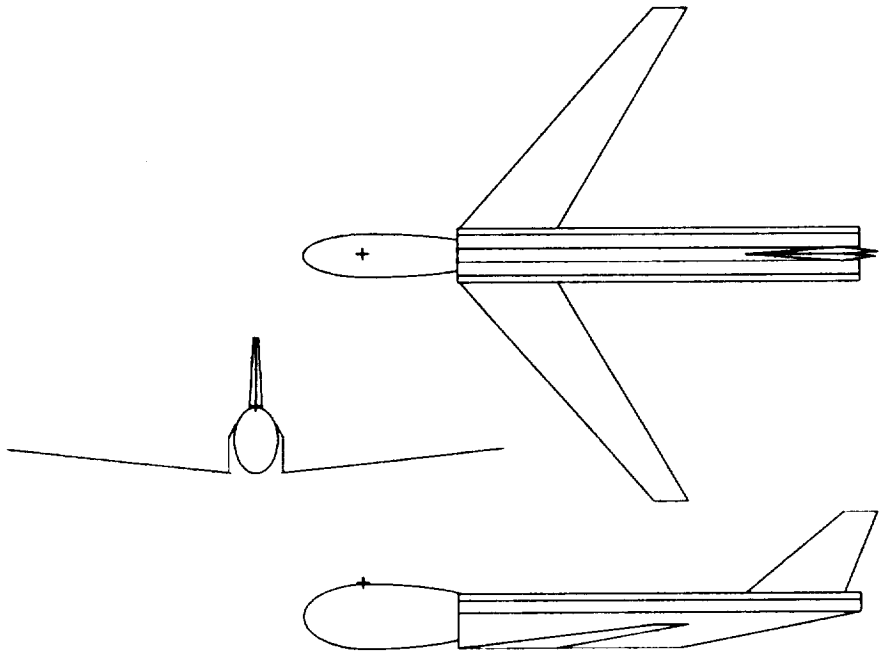

Figure 3.8: Computer model for Boeing 747-200: top mounted antenna (forward).

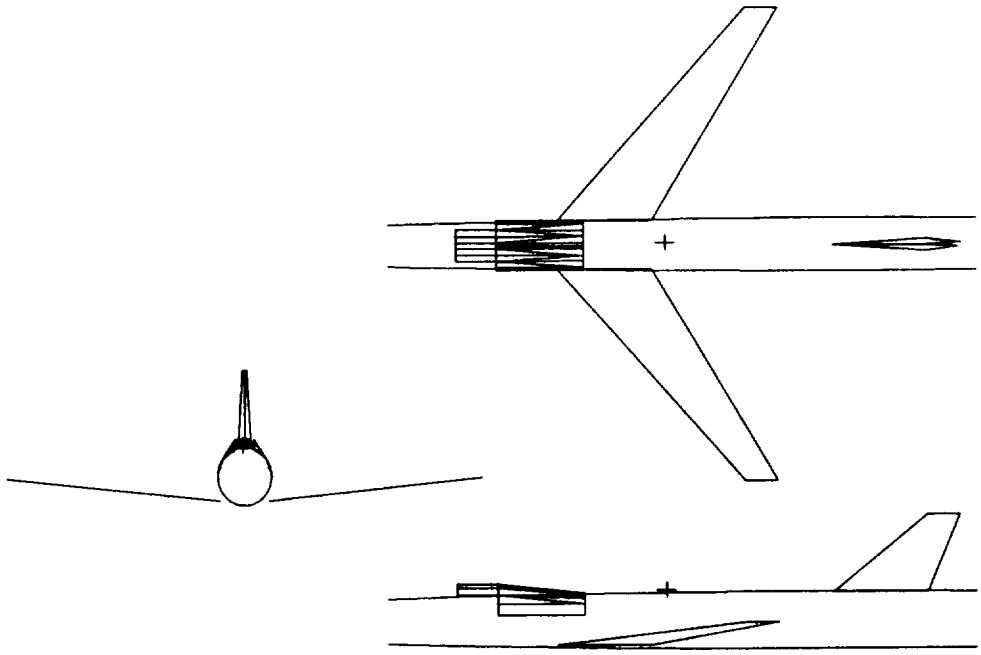

Figure 3.9: Computer model for Boeing 747-200: top mounted antenna (aft).

The standard deviation curves for the CRA and SPA TCAS systems are shown in Figure 3.10. Note that station number 90 is at the nose of the aircraft. The corresponding statistical data is given in Tables A.5 and A.6. It is observed that the standard deviation is very small and similar for both systems. The optimal location for both antennas turns out to be at station 0540, where the monopole antennas are approximately vertical with respect to the fuselage. The optimum locations for the top mounted TCAS are shown in Figure 3.11. Since the standard deviation curve is fairly constant, the TCAS antenna may be placed at any convenient location between stations 0400 and 0800. This region lies on top of the cupola. If the antenna is moved farther back to stations 1380 and 1440, the standard deviation is much larger. This is to be expected, and arises due to scattering by the cupola, which now lies directly in front of the antenna.

As in the case for the Boeing 737-300, the engines have to be included when simulating the TCAS mounted on the bottom of the fuselage. Two typical computer models for the aircraft for bottom mounted antennas are shown in Figures 3.12 and 3.13. As mentioned earlier, these are the worst case error calculations, in that the engines are modeled by closed, perfectly conducting boxes. The standard deviation curves as a function of station number are given in Figure 3.14. The optimum locations for both systems happen to be at station 0320 and are shown marked on a line drawing of the airplane in Figure 3.15.

The engines do not affect the performance as badly as the Boeing 737-300. The reason for this is twofold. First, the engines are farther away from the TCAS antenna, and second, the engines are slightly higher than the level of the bottom of fuselage. Since elevations in the range of 0° to -20° are considered, the scattering from the engines affects the patterns somewhat less. As a result, the standard deviation is seen to increase as the antenna approaches the mid section of the fuselage, but the rise is not as steep as the Boeing 737-300. Again, the CRA system performs better than the SPA system for the locations considered.

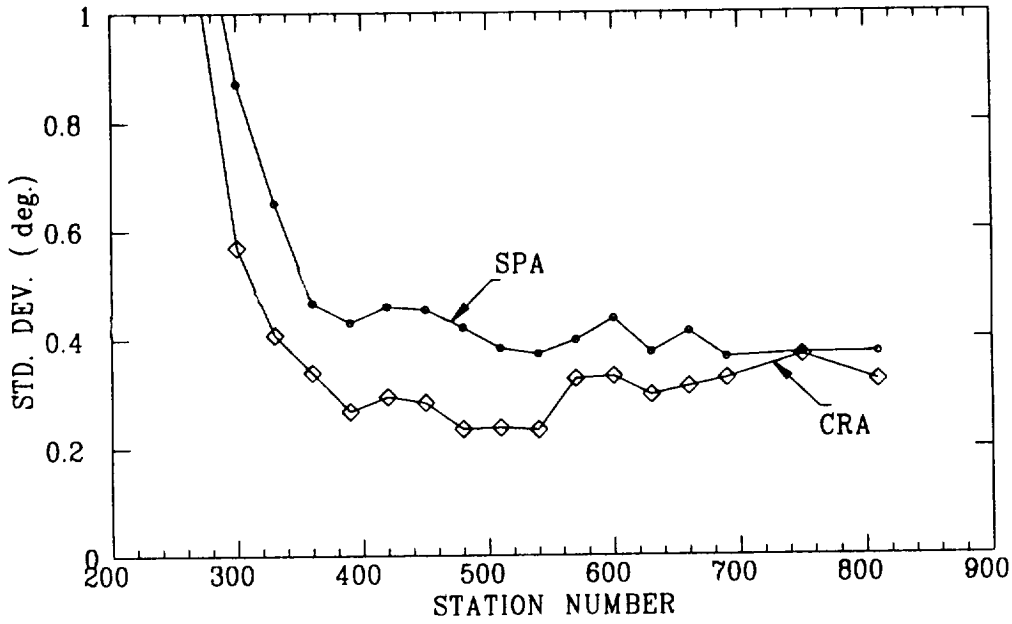

Figure 3.10: Standard deviation for top mounted antenna: Boeing 747-200.

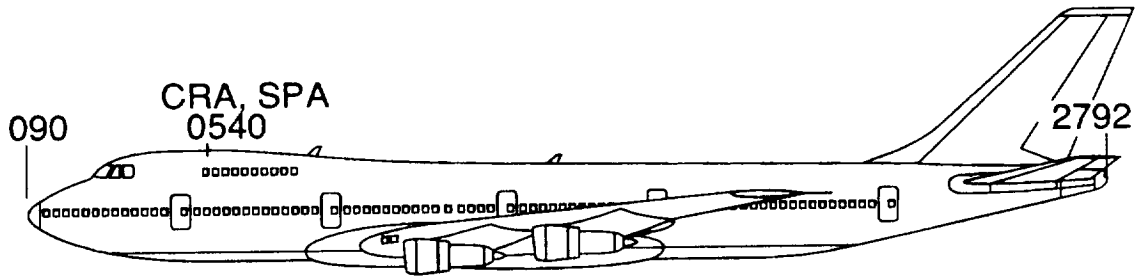

Figure 3.11: Optimum location for CRA and SPA top mounted arrays: Boeing 747-200.

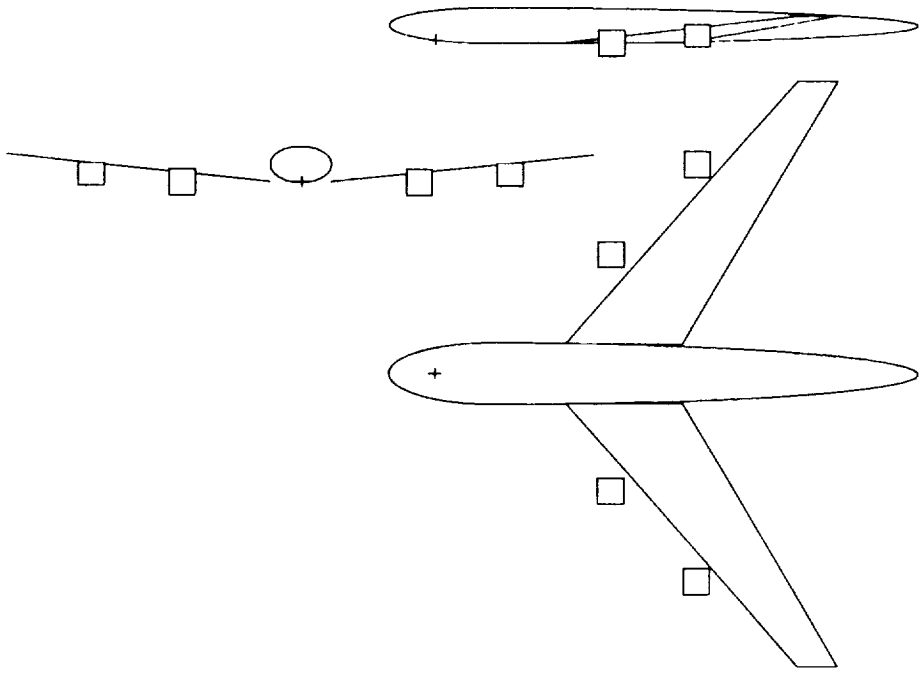

Figure 3.12: Computer model for Boeing 747-200: bottom mounted antenna (forward).

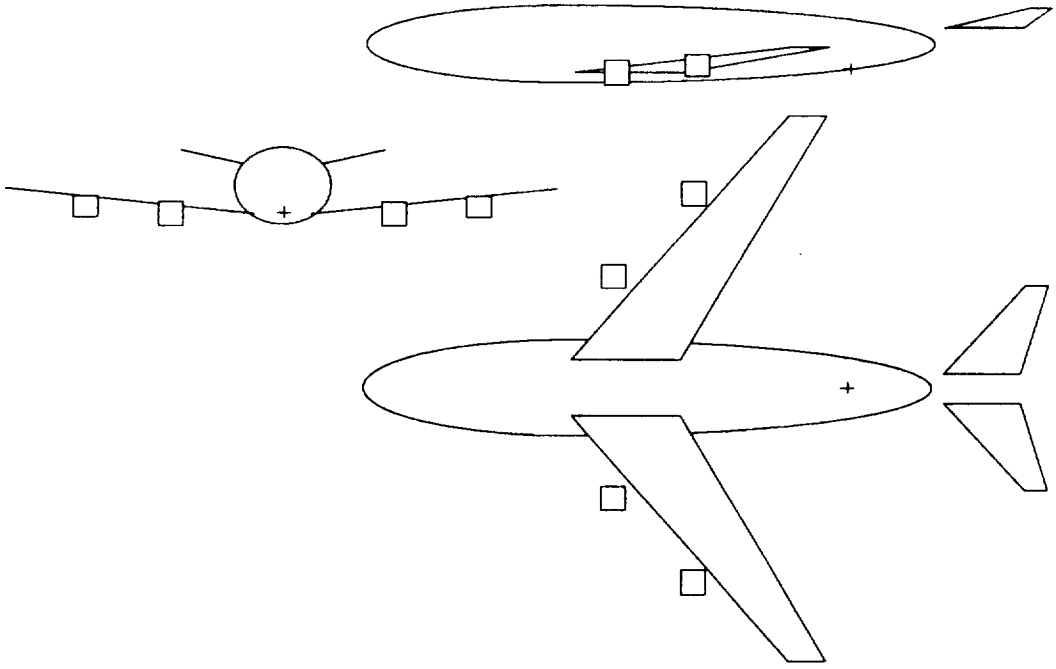

Figure 3.13: Computer model for Boeing 747-200: bottom mounted antenna (aft).

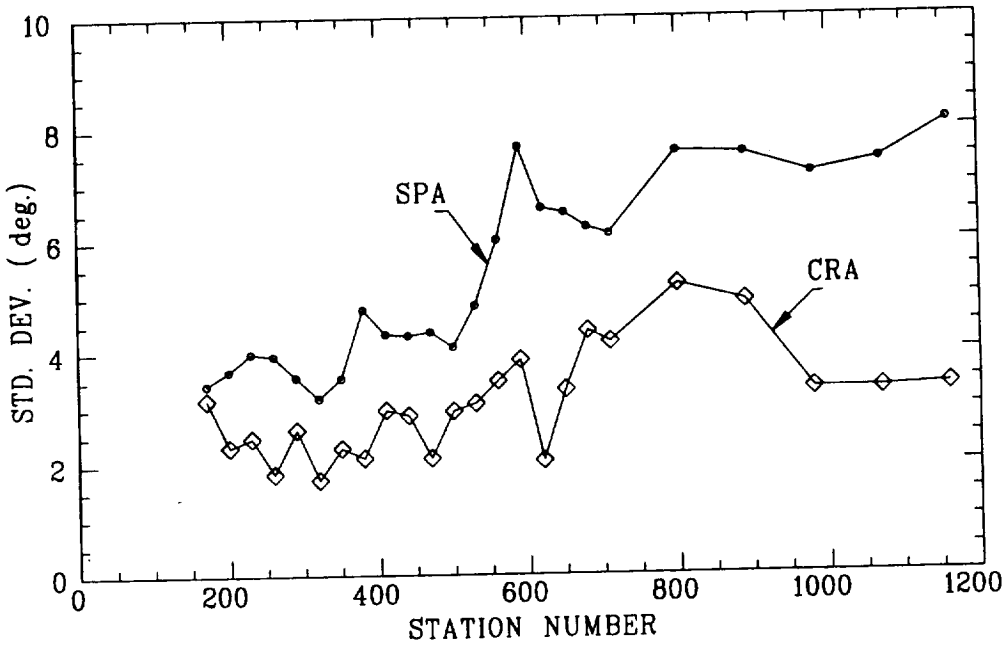

Figure 3.14: Standard deviation for bottom mounted antenna: Boeing 747-200.

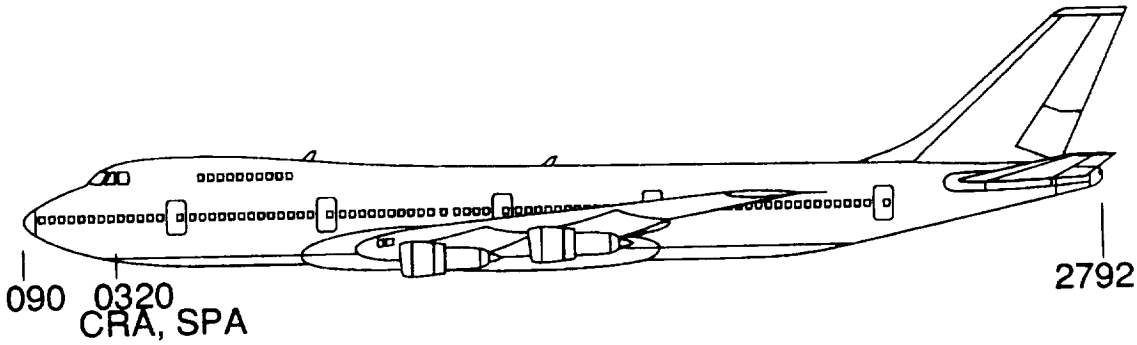

Figure 3.15: Optimum location for CRA and SPA bottom mounted TCAS arrays on the Boeing 747-200.

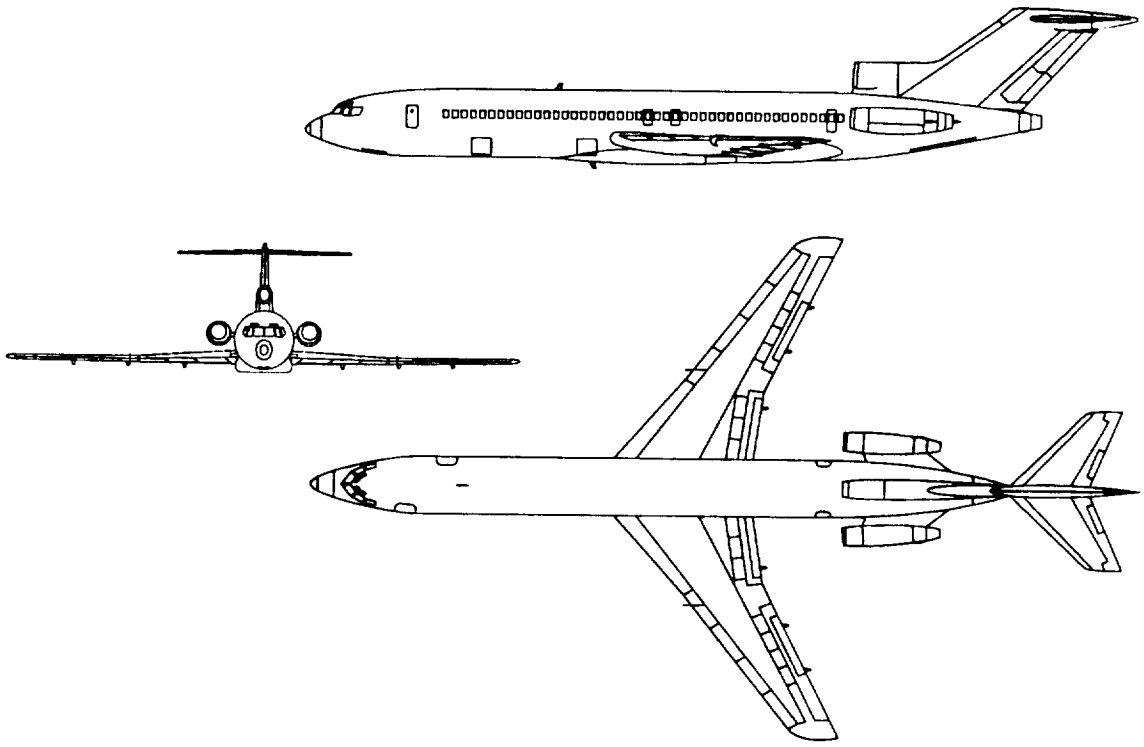

Figure 3.16: Scaled line drawings of the Boeing 727-200 aircraft.

3.4 Boeing 727-200

The Boeing 727-200 airframe was included in this study for its rather unusual placement of engines — two on the fuselage on either side, and a third engine directly underneath the vertical stabilizer on top of the fuselage. The scaled line drawings for this aircraft are shown in Figure 3.16. The computer model for the top mounted antennas is shown in Figure 3.17. The corresponding standard deviation curves are given in Figure 3.18. The most striking feature of this error curve is the relative flatness of the CRA curve, as opposed to the steep increase in the SPA error. The optimal locations for the CRA and the SPA systems are at 200″ and 140″, respectively, from the nose. These locations are marked on Figure 3.19.

It is important to note that the space available on the fuselage of a commercial airplane to locate a TCAS antenna is very limited due to the presence of many

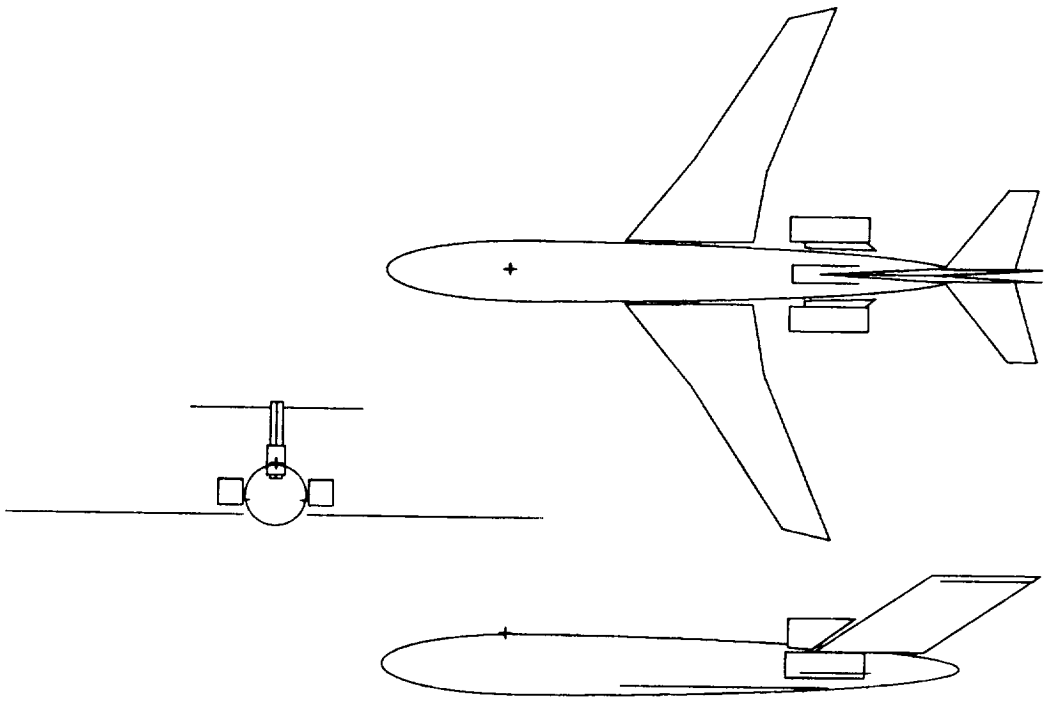

Figure 3.17: Computer model for Boeing 727-200: top mounted antenna.

other antennas. Thus, if the location of the TCAS antenna were based solely on the performance depiction in Figure 3.18, the CRA system has an edge over the SPA because its standard deviation is smaller and more constant. Therefore, the CRA antenna may be located anywhere between 100″ and 580″ and still keep the standard deviation of bearing error less than about 1.5°. The SPA antenna, in contrast, is restricted to be in the far forward region of the aircraft, because its standard deviation increases rapidly. This is partly due to the specular reflection in the forward region from the plate covering the front face of the center engine. It is emphasized that, this is the worst case calculation and a better solution, based on the self-consistent multiple scattering matrix formulation is presented in Chapter 5.

The bottom mounted antenna on the Boeing 727-200 behaves differently. The high frequency model used for this computation is shown in Figure 3.20. In contrast to the top mounted antenna, the performance of both systems is very similar as shown in Figure 3.21. The corresponding optimum locations are shown marked on

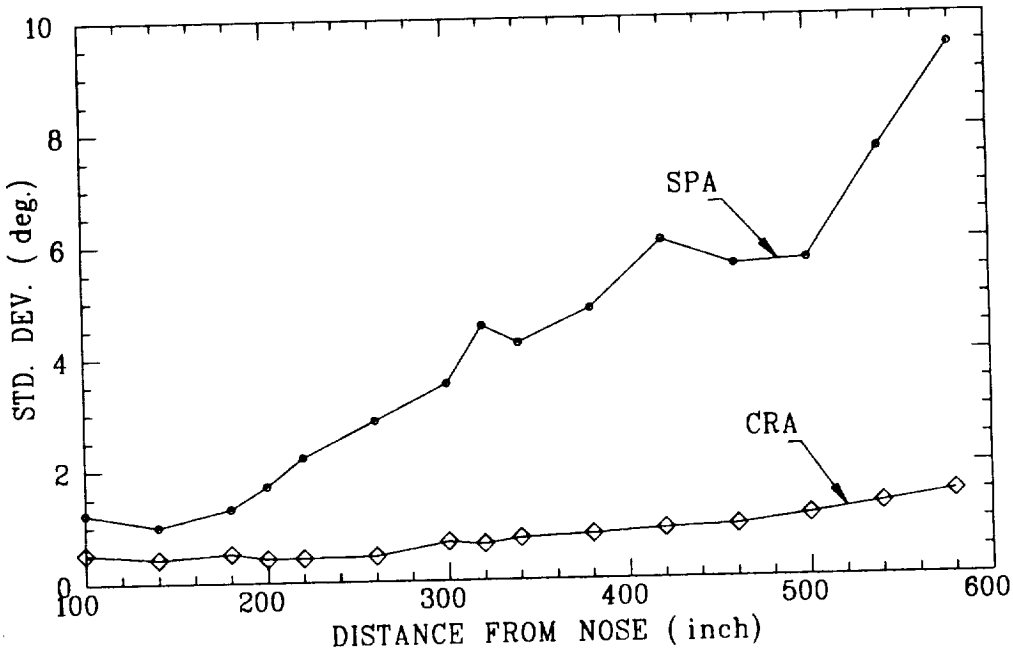

Figure 3.18: Variation of standard deviation with location for top mounted TCAS array for the Boeing 727-200.

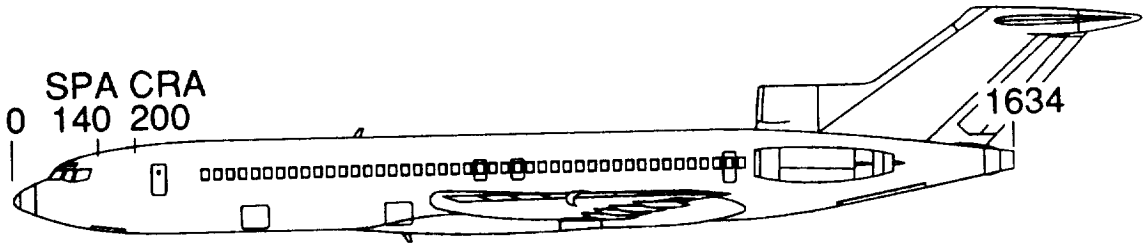

Figure 3.19: Location of optimum position for top mounted CRA and SPA antennas on the Boeing 727-200.

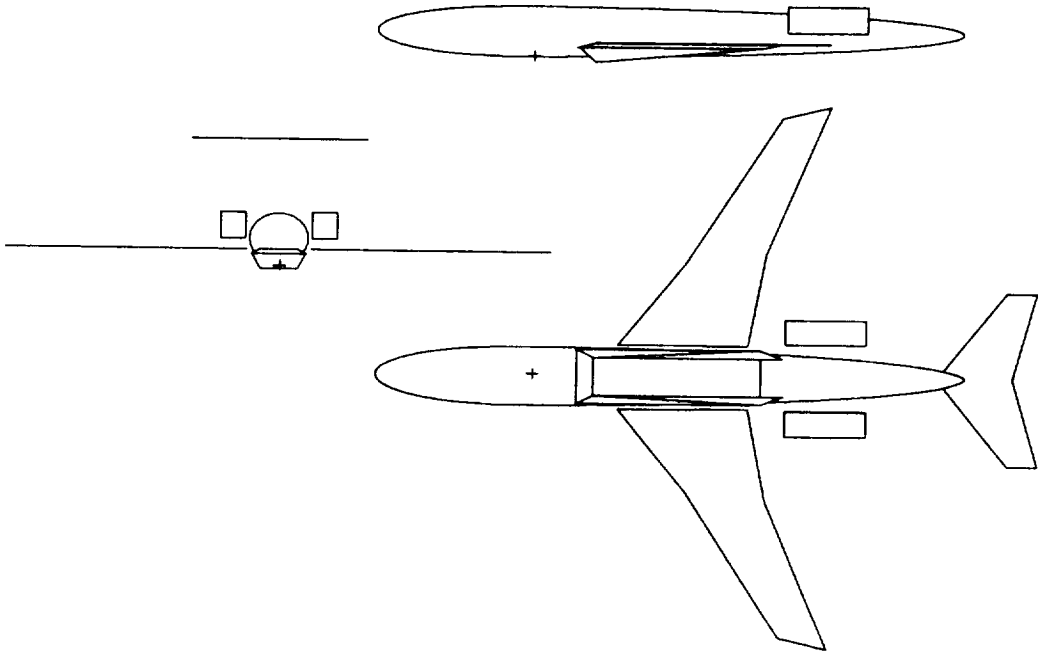

Figure 3.20: Computer model for Boeing 727-200: bottom mounted antenna.

Figure 3.22. It is seen that the antenna on the bottom may be placed anywhere from about 220″ to 380″ and still have a standard deviation close to the value reached at the optimum location.

3.5 Discussion

From the above simulations of both systems on various aircraft, some general trends are apparent. These are discussed below.

The error generally increases as one moves the antenna closer to the nose. This is very noticeable in Figures 3.1 and 3.10, for both CRA and SPA systems, and for the SPA system in Figure 3.18. This is due to the increasing slope of the fuselage as the distance between the TCAS antenna and the nose decreases. Recall that the calibration table was created for a location of the antenna that is relatively flat; i.e., the antenna normal points straight up. When the TCAS array is very close to the

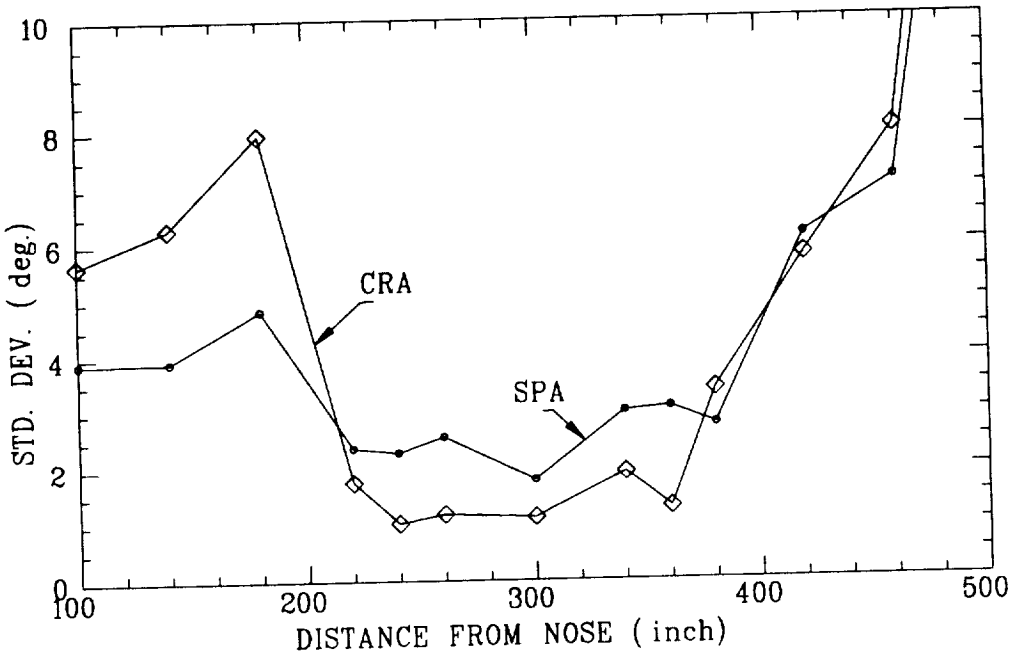

Figure 3.21: Standard deviation curves for bottom mounted antenna on the Boeing 727-200.

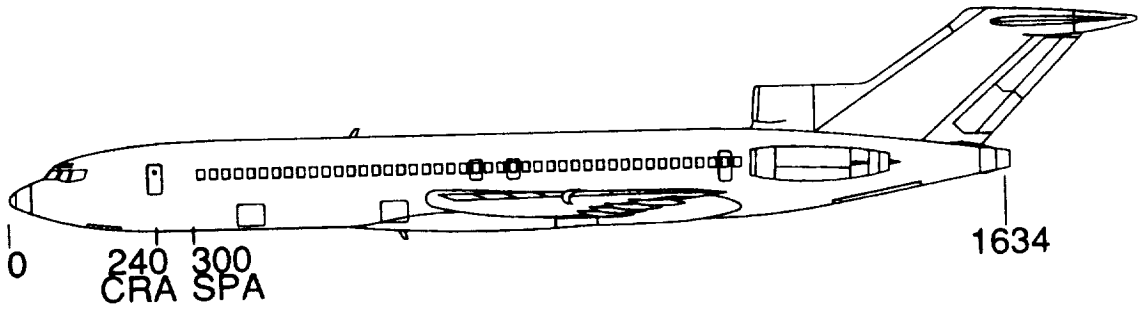

Figure 3.22: Location of optimum position for bottom mounted CRA and SPA antennas on the Boeing 727-200.

nose, the antenna normal is pointing towards the front of the aircraft. This tilt can be as great as 25° as in the case of the Boeing 747-200 for station 0270, as interpreted from Table A.5. Thus, there are larger variations in the azimuth pattern than for locations where the antenna points more straight up. This leads to a higher error being computed for locations closer to the nose than those farther aft.

It is also seen that the error is fairly constant for both TCAS systems when they are away from structural scatterers. The effect of the engine is noticeable in the curves for bottom mounted antennas for the Boeing aircraft, 737-300 and 747-200, and for the top mounted antenna on the Boeing 727-200. The role of these engines is to move the optimum location forward. Note that the effects of the engine tends to decrease as the antenna is far forward, in the rising portion of the bottom due to the natural blocking offered by the fuselage. As the antenna moves closer to the nose, the errors due to the engine decrease, whereas those due to the slope of the fuselage increase. Thus, for the bottom antenna, the optimal TCAS location is a compromise between these two factors. The effect of the engine model is discussed more completely in Chapter 5.

The SPA TCAS is a phase comparison system, which is sensitive to even small variations in the distance. For the TCAS operating at 1090 MHz, this translates to a phase error of about 33.2°/inch of error in distance measurement. This is compared to the CRA system, which operates by comparing the amplitudes of the received signals via the four beams. Obviously, the variation in received signal amplitude is much less for errors in distance measurement, because the amplitude varies roughly as r^{-1}. Thus, for a given received signal, the amplitude system is less prone to errors in calculation as well as measurement.

Recall that the bearing error for a TCAS location is computed by comparing the received signals in a lookup table. The lookup table used in the case of the CRA system has four distinct, monotonic sections, one of which is searched. The section chosen depends on the largest two signals received. The range of these tables is

about 20–24 dB over each section, which is about 90° wide. Hence, considering the worst case, an amplitude error of 1 dB results in an angle of arrival error of 4.5°; but, for typical cases, the amplitude errors are much smaller, and hence the error in the AOA. The SPA system also has a lookup table which is monotonic over the whole azimuth (slope is unity). Thus, a phase error of 1° leads to the same amount of error in bearing determination.

This affects the error calculation as follows: Consider the received signal from a given scatterer at a certain distance. The procedures to determine the reflection/diffraction points on a plate, geodesic paths on the composite ellipsoid etc., are mostly by numerical search. The received signal amplitude remains constant, whereas, the phase is affected by the distance to the scatterer, as well as the location of the specular point on the scatterer. Thus, large phase variations occur due to small numerical errors in distance measurement.

Similarly, when the receiver is shadowed by the fuselage, a numerical search is conducted to find the location of the effective source on the fuselage, from where the ray is launched tangentially to reach the receiver. For the same reasons cited above, the performance of the SPA system degrades much more rapidly than the CRA system, as the receiver moves deeper in the shadow region, or as the geodesic path gets longer.

Finally, consider an intruder in the forward quadrant of the airplane. Consider also, a scatterer, say a vertical stabilizer or a blade antenna to the aft of the TCAS. For the CRA system, the received signals combine to yield the highest channels as 0 and 1. The scattered signal from the blade is very small and it will not affect the bearing determination. On the other hand, with the SPA system, there is no such beam switching employed, and the transponder signal from the intruder in the forward region receives the same weight as a stray scattered signal. Hence, even though the SPA and CRA systems have comparable performance in the absence of scatterers, the CRA system performs better in the vicinity of scatterers.

Chapter 4

Effect of Other Antennas

4.1 Introduction

In the previous chapters, the operation of the TCAS system in the absence of any nearby antennas was considered. The distortion of the radiation patterns by the airframe resulted in an incorrect bearing being computed. There, it was assumed that the TCAS antenna was far away from (many wavelengths) all other antennas. This is not a realistic assumption on a modern commercial aircraft, where one might expect to find up to one hundred antennas, all vying for generally the same area on the fuselage. When the TCAS is in operation, it induces currents on the antennas located in its vicinity. These induced currents then radiate electromagnetic fields and distort the radiation pattern of the TCAS array. The magnitude of the induced current depends upon many factors, such as distance to the second antenna from the TCAS array, size of the antennas, power radiated etc. Moreover, when the frequency of operation of the other antenna is close to that of the TCAS, the actual induced currents in the TCAS array can be very different from the design. Thus, a smaller antenna might also have a significant effect on the operation of TCAS. Hence it is necessary to model each antenna in the vicinity of the TCAS and study the changes in the behavior of the TCAS as a whole.

Two blade antennas are considered here because they are found on all commercial aircraft. Mathematical models are developed to include the effect of the

electromagnetic re-radiation from these nearby antennas on the TCAS currents. The performance is re-evaluated based on the bearing error curves. It is seen that the nearby antennas can (and often do) significantly affect the performance of the TCAS. Finally, it is also seen that the effect of nearby antennas on the SPA TCAS is much worse than that of the CRA system.

4.2 Modeling a Nearby Antenna

Two blade antennas, which are the most common antennas used for VHF and L-band communications, are likely to be found in the vicinity of the TCAS antenna and are chosen for this study. These are the following:

1. L-Band blade antenna (Mode S): Dorne and Margolin Model AT-741.

2. VHF communications antenna: Dorne and Margolin Model DMC60-1.

The line drawings of these blade antennas are depicted in Figures 4.1 and 4.2. As can be seen, both antennas are thin blades due to aerodynamic considerations. The AT-741 is only about $\lambda/4$ in height; whereas the DMC60-1 is over one wavelength tall at the TCAS receiving frequency (1090 MHz).

In the UTD analysis using the NEWAIR code, one can synthesize a fairly arbitrary variety of radiation patterns by a set of short monopoles and/or slots. However, it is necessary to first determine the radiation pattern of the antenna under study. Moreover, the above code can not calculate the mutual coupling between various antennas mounted on the fuselage; thus, it can not calculate the currents induced on the surface of the blade by the TCAS array. Hence, it is necessary to first calculate the currents induced on the blades by other means, and next, the fields radiated by these currents. Once the fields of the nearby antennas are found, they can be superimposed with the radiation pattern of the TCAS antenna to include the effect of the blade.

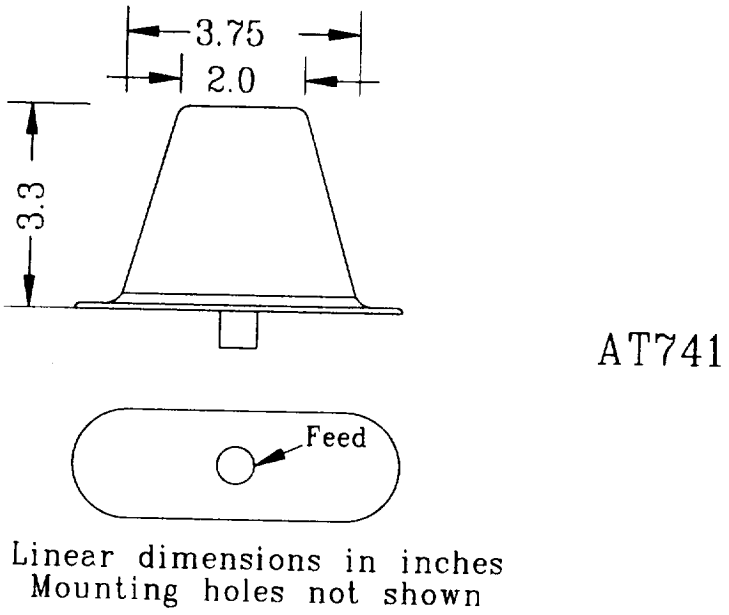

Figure 4.1: Line drawing of AT-741, L-band blade antenna.

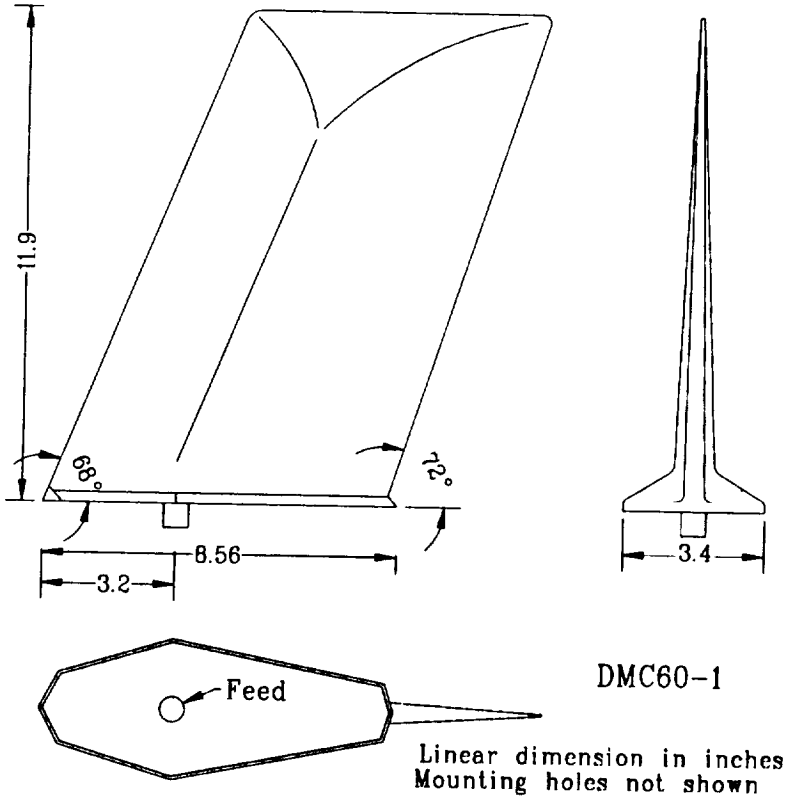

Figure 4.2: Line drawing of DMC60-1, VHF band blade antenna.

The scheme used to accomplish this task is as follows. Since both antennas are normally mounted near the centerline of the fuselage, they are within the paraxial region. Thus, one can not use the high frequency methods that compute the mutual coupling between the two antennas [25]. Since the curvature of the fuselage is very small along the axis and the antennas are close to each other, one can approximate the fuselage by a flat surface. One may then model the arbitrary geometry via the moment method (MM). For this case, where the radiation pattern of the blade antenna has to be calculated, the Electromagnetic Surface Patch Code (ESP4) is used to model the geometry in free space. To this end, the TCAS array is modeled by a set of short monopoles. The voltages at each feed point are adjusted to generate modal currents of the same magnitude and phase as the currents of the model used in the UTD analysis in the NEWAIR3 code. The radiation pattern is then calculated via both MM and UTD to verify the accuracy of the model.

Next, each blade is modeled by a flat plate. Based on measurements conducted at MIT Lincoln Laboratory, it was determined that the resistive termination (load) placed at the terminals of the blade had very little effect on the radiation patterns of the TCAS antenna [26]. From this, it may be concluded that the nearby blade antenna behaves much more like a scatterer than an antenna. Hence, the blade could be modeled in each case as a scatterer. Once the currents induced on the blade surface are calculated for a particular separation and elevation, they are stored for later use. Since the steps used in the analysis of L-band and VHF blades differ widely, they are discussed separately in the following sections.

4.3 L-band AT-741 Blade

Keeping in mind that only short monopoles, normal to the fuselage at the point of attachment can be used in the NEWAIR3 code, one first replaces the blade by a set of four wires strategically placed as shown in Figure 4.3. This is possible because the dominant induced currents on the blade are predominantly vertical, such that

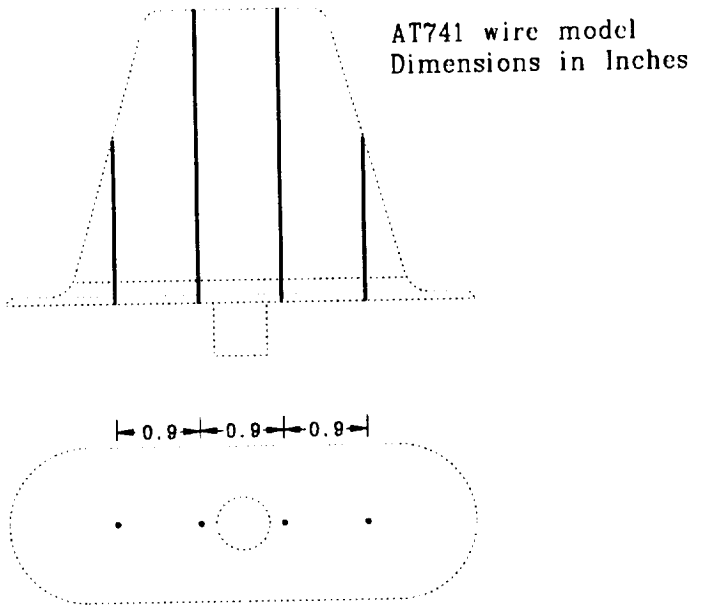

Figure 4.3: Wire model of L-band blade used in the moment method analysis.

the horizontal component can be neglected. This is demonstrated in Figure 4.4, where the patterns obtained via the moment method for the blade model and the four wire model are shown for a blade located 4 feet (48″) aft of the CRA antenna array. The blade/wire model was illuminated by the beam pointing towards the blade (beam 2), and the radiation pattern was computed at 10° elevation. One should observe that the two radiation patterns are in good agreement. Since the monopoles used in the UTD analysis have to be under $\lambda/4$ long, the two wires in the middle, which were slightly longer than $\lambda/4$ were trimmed to $\lambda/4$ and the induced currents and radiation pattern were computed again to verify that they did not change appreciably. The final wire model for the AT-741 blade used in the UTD analysis is shown in Figure 4.5.

The final step in this synthesis process is the inclusion of the radiation pattern of the blade in radiation patterns for the TCAS array. This can be accomplished via two methods. One can either recompute each element pattern in the presence of the blade antenna and process the received signals, or, compute the blade scattered fields

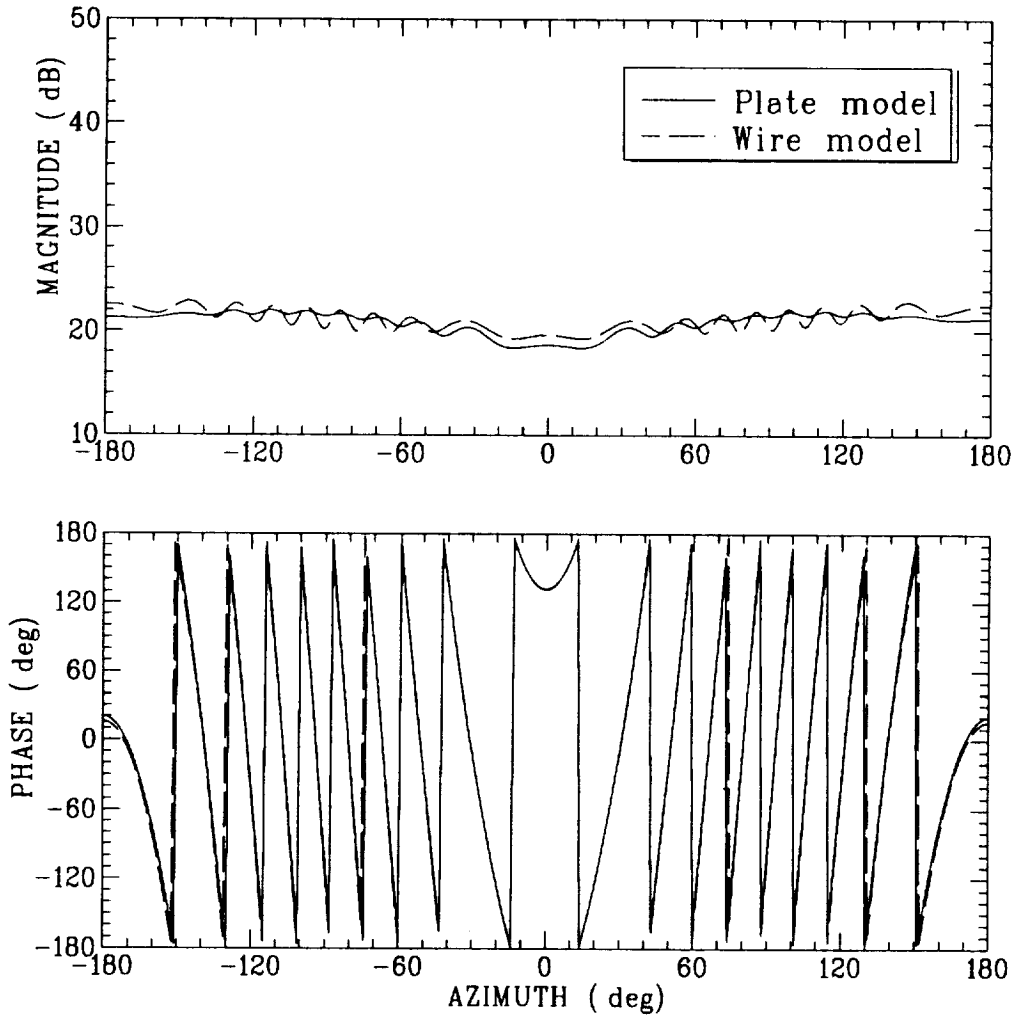

Figure 4.4: Comparison of radiation pattern of plate and wire models obtained via the moment method.

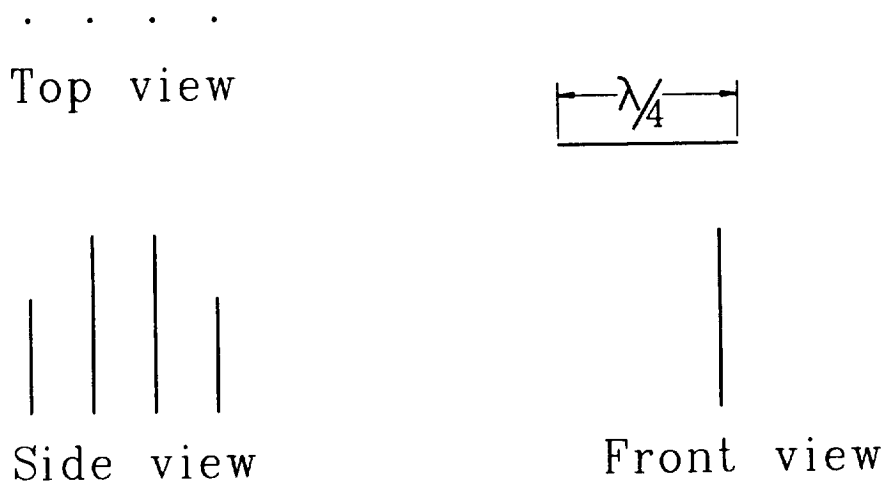

Figure 4.5: Wire model used in NEWAIR3 code for the AT741 antenna.

by illuminating it by the four CRA beams or by the sum and difference beams of the SPA TCAS in turn. These can be then directly added to the corresponding received signals. (Of course, one must be careful about the phase centers of the TCAS and blade antennas). The latter approach is adopted here, due to its flexibility and the fewer computations required.

In case of the CRA array, there are four beams each pointing in a different direction. Hence the illumination of the blade is different for each beam, and so are the induced currents. Thus, the CRA beams are created via the moment method by weighting the monopoles correctly, and the induced currents due to each beam on the wires are calculated and stored for use with the NEWAIR3 code. Similarly, for the SPA array, the sum and difference beams are created separately and the induced currents on the wires due to this type of illumination are also calculated and stored.

The curvature of the fuselage has only a small effect on the patterns of the blade antenna, because both antennas are along the axis of the fuselage, where the curvature close to zero. Hence, the approximation of the fuselage by a ground plane

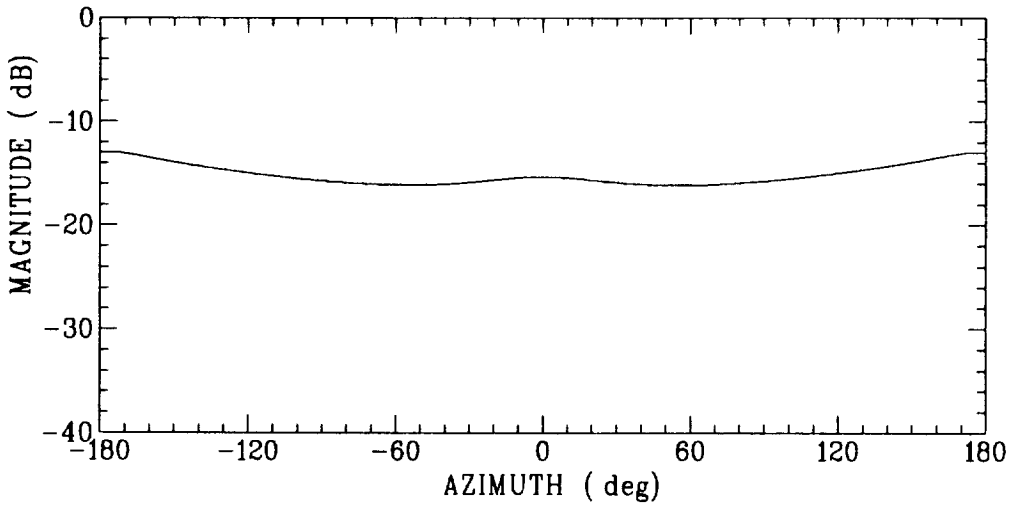

Figure 4.6: Radiation pattern of wire model for the L-band blade mounted on the fuselage of Boeing 727-200, calculated via UTD.

is valid. To demonstrate this, the wire model of Figure 4.5 was mounted on top of a Boeing 727-200 fuselage, 380″ from the nose. The scattered fields of the blade model for the CRA beam pointing towards the blade (beam 2) is shown in Figure 4.6 at an elevation of 10°. Note that, even though the levels of the two field patterns differ by about 34 dB in the moment method computation and those obtained via UTD, the relative levels of radiation from the blade antenna with respect to the peak level of the TCAS beam is the same (about 17 dB).

4.4 VHF DMC60-1 Blade

The VHF communication blade is one of the most common antennas found on commercial aircraft. It is even included in the line drawings of the airplanes given in Figures 2.11, 3.7, and 3.16. It is a general purpose VHF communication antenna operating in the 118–136 MHz range. Modeling this antenna for use in the NEWAIR3 code presents some unique problems, most of which are due to the size and shape of the antenna. As in the case of the L-band blade, the plate model obtained by the moment method is replaced by a set of inclined wires shown in Figure 4.7. These

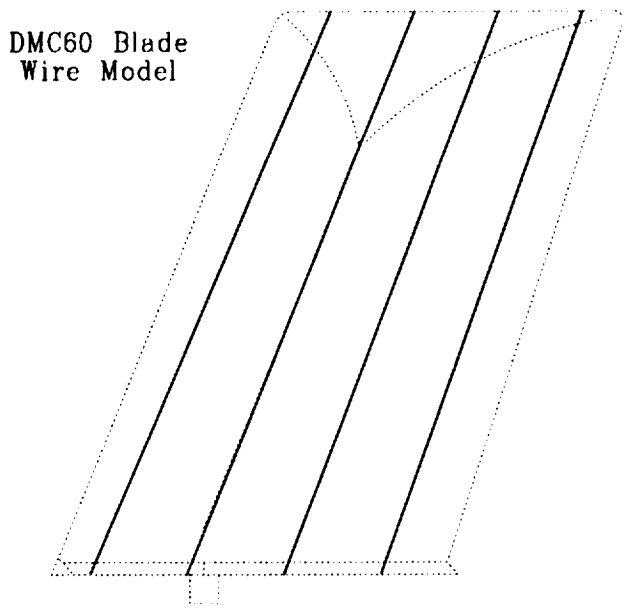

Figure 4.7: Model for the VHF blade using inclined wires.

wires are inclined at about 70° with respect to the ground plane. The radiation pattern for the flat plate model and the inclined wire models agree well as shown in Figure 4.8. The radiation patterns do not agree well when the wires are vertical. This indicates that the induced currents on the blade have significant horizontal as well as vertical components. The inclined wire model can not be directly used in the UTD procedure. The monopole antennas used in the NEWAIR3 software must meet the following criteria:

a. the monopoles must be perpendicular to the fuselage, and

b. the length of the monopoles must be less than $\lambda/4$.

The inclined wires are about one wavelength long at 1090 MHz, and hence, simply replacing the wires by short $\lambda/4$ monopoles will not give acceptable results. Hence other methods of synthesis must be explored, which meet the above constraints.

The objective here is to synthesize an arbitrary radiation pattern denoted by E_θ^m using an arbitrary planar array of N vertical monopoles on a ground plane. The

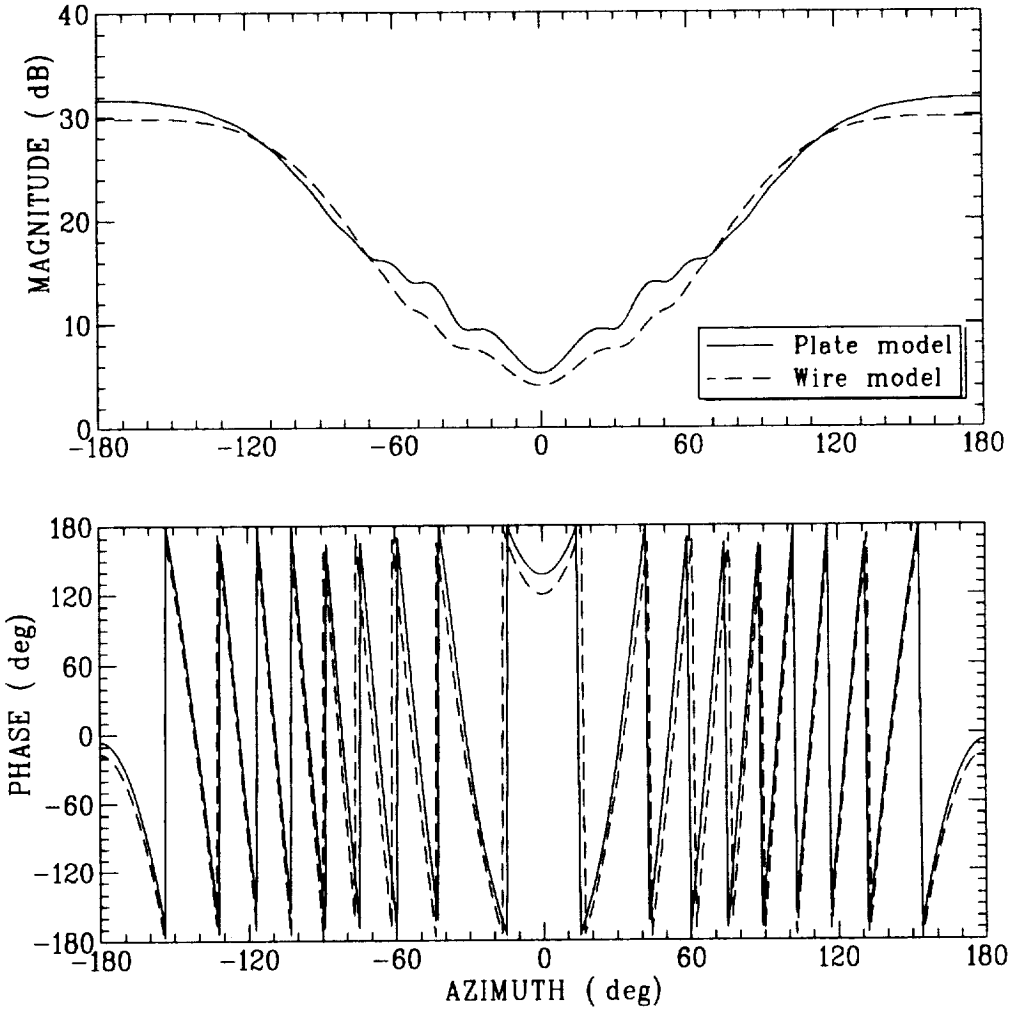

Figure 4.8: Radiation pattern of flat plate and inclined wires model for VHF blade mounted on flat ground plane.

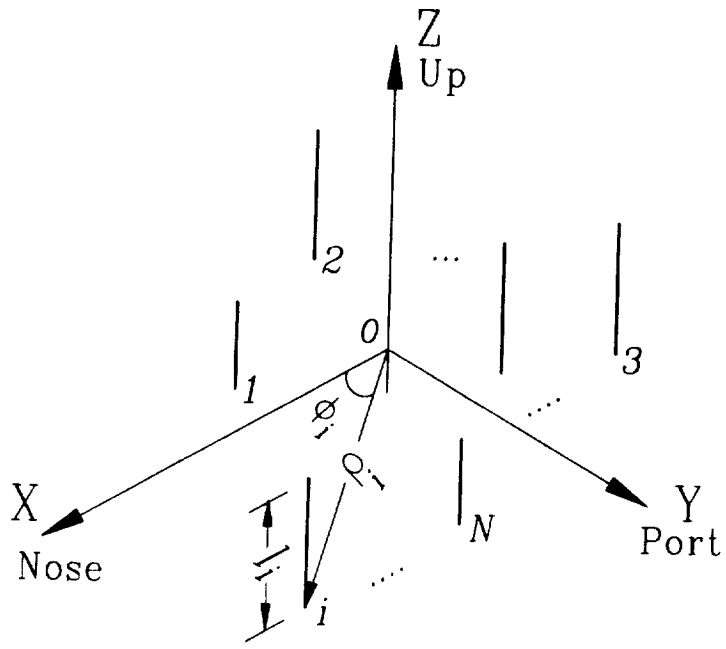

Figure 4.9: An arbitrary planar array of N monopoles.

field E_θ^m is the scattered field by the blade, computed in this case via the moment method.

The geometry of the planar array is shown in Figure 4.9. Let the length of the i^{th} monopole be defined by l_i and its position by ρ_i, and ϕ_i. The excitation of this monopole is given by

$$I_i = A_i e^{j\alpha_i} \tag{4.1}$$

where A_i is the amplitude, and α_i is the phase of the excitation.

The radiated field of this monopole array in the far-field is given by

$$E_\theta^w(\theta,\phi) = \sum_{i=1}^{N} \frac{j\eta I_i}{2\pi} \left[\frac{\cos\left(\frac{kl_i}{2}\cos\theta\right) - \cos\frac{kl_i}{2}}{\sin\theta} \right] e^{jk\rho_i \sin\theta\cos(\phi-\phi_i)} \tag{4.2a}$$

and

$$E_\phi^w(\theta,\phi) = 0 \tag{4.2b}$$

at any receiver location (θ,ϕ). The superscript denotes that the field is due to the monopole (*wire*) elements. Now, let E_θ^m be given at M receiver positions,

(θ_j, ϕ_j), $j = 1, 2, \ldots, M$. Then, let us set:

$$E_\theta^m(\theta_j, \phi_j) = \sum_{i=1}^{N} I_i Z_{ij}, \qquad j = 1, 2, \ldots, M \tag{4.3}$$

where

$$Z_{ij} = \frac{j\eta}{2\pi} \left[\frac{\cos\left(\frac{kl_i}{2}\cos\theta_j\right) - \cos\frac{kl_i}{2}}{\sin\theta_j} \right] e^{jk\rho_i \sin\theta_j \cos(\phi_j - \phi_i)}. \tag{4.4}$$

For $M > N$, as is normally the case, this denotes an over-determined system of equations. In matrix notation, one finds that

$$[\mathbf{E}_\theta^m] = [\mathbf{Z}][\mathbf{I}] \tag{4.5}$$

where

$$[\mathbf{E}_\theta^m] = \begin{bmatrix} E_\theta^m(\theta_1, \phi_1) \\ E_\theta^m(\theta_2, \phi_2) \\ \vdots \\ E_\theta^m(\theta_M, \phi_M) \end{bmatrix} \tag{4.6}$$

$$[\mathbf{Z}] = \begin{bmatrix} Z_{11} & Z_{12} & \cdots & Z_{1N} \\ Z_{21} & Z_{22} & \cdots & Z_{2N} \\ \vdots & & \ddots & \\ Z_{M1} & Z_{M2} & \cdots & Z_{MN} \end{bmatrix} \tag{4.7}$$

and

$$[\mathbf{I}] = \begin{bmatrix} I_1 \\ I_2 \\ \vdots \\ I_N \end{bmatrix}. \tag{4.8}$$

In the above equations, [I] is the unknown excitation vector to be solved for. This is derived using techniques from linear algebra such that

$$[\mathbf{I}] = \left[([\mathbf{Z}]^T [\mathbf{Z}]) \right]^{-1} [\mathbf{Z}]^T [\mathbf{E}_\theta^m]. \tag{4.9}$$

The solution for [I] thus obtained via (4.9) is the least squares solution [27]. This minimizes the squared difference between the fields due to the blade E_θ^m and due to the set of wires E_θ^w. It is noted that the above analysis is fairly general, and can be easily modified to account for radiation from any arbitrary set of antennas, like radial and axial slots, and/or a combination of wires and slots.

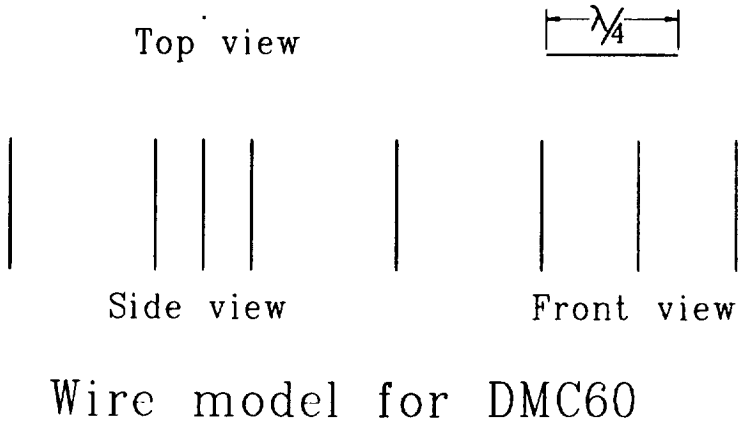

Figure 4.10: Wire model of VHF blade for NEWAIR code.

A model that was both accurate and easy to use in the NEWAIR3 code was then derived by varying the parameters of the monopole array such as length and spacing. It was observed that much better results (smaller number of monopole elements, lesser error) were obtained when the above procedure was carried out around the phase center of the blade antenna. This is because, when the scattering patterns of an antenna are referred to its phase center, variations in the phase are minimized. This becomes especially important when the separation between the two antennas is large, and the phase varies rapidly. The final model for the DMC60-1 consisted of six $\lambda/4$ monopoles arranged as shown in Figure 4.10.

The model was verified using the NEWAIR3 code by computing the radiation pattern of the monopoles located 48″ aft of the CRA TCAS antenna, on the fuselage of a Boeing 727-200, at 10° elevation. The radiation pattern of this array when illuminated by the beam pointing toward the tail (beam 2) is shown in Figure 4.11. The agreement is very good. Again, the difference in levels is relative, due to different normalizations in the two methods; i.e., the moment method and UTD.

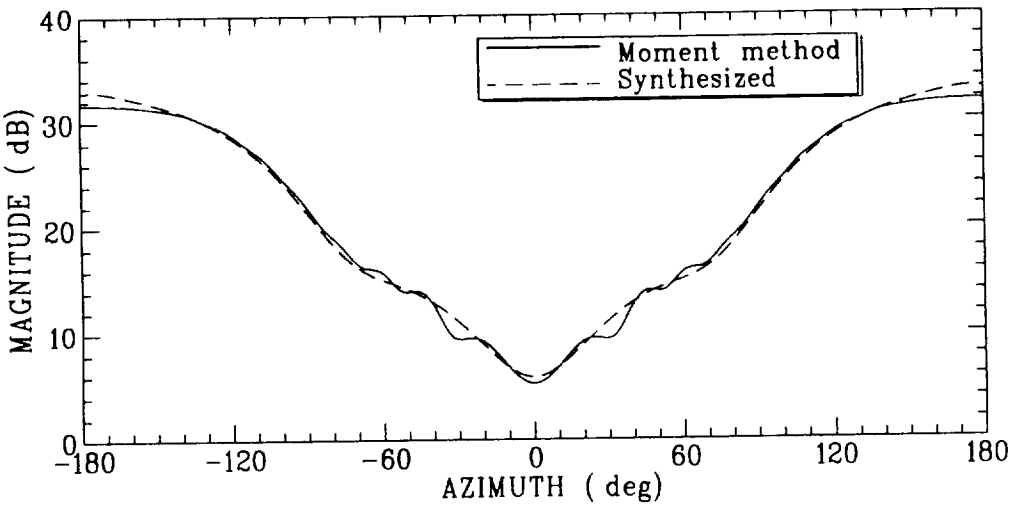

Figure 4.11: Radiation patterns of moment method and UTD models of VHF blade mounted on fuselage of Boeing 727-200.

It was found that these two models agree well only for a small range of elevation angles around which the synthesis was carried out. This is because, the flat plate model has horizontal components of induced currents, which are not accounted for by the monopole model. Hence, the synthesized monopole model can not be used for more than about 10° around the elevation at which it was created. Therefore, unlike the model for the L-band blade, it is necessary to calculate the induced wire currents at several elevation angles. As in the case of the L-band (AT741) antenna, the induced currents were calculated for each beam of the CRA array as well as the sum and difference beams of the SPA antenna.

4.5 Simulation and Results

Once the induced currents have been obtained, the monopole models for the L-band and VHF blades are placed on the fuselage of the aircraft under consideration. Since the total received fields are found using superposition, the TCAS array pattern is included as a separate term. The radiation patterns of these simulated blade antennas were then calculated in the presence of all scatterers on the airframe and

for the various illuminations at different distances from the TCAS array. Finally, the corresponding radiation patterns were superimposed, to obtain the patterns for the TCAS antenna when it is operating in the presence of the blade.

Error curves corresponding to a location 289″ from the nose on a Boeing 737-300, for elevations $-10°$ to $20°$ were already introduced in Figures 2.13–2.16. In these curves, the effect of the vertical stabilizer is apparent in the rear quadrant, but overall, the errors are relatively small. Figures 4.12–4.15 depict the same antenna location, except that the TCAS is now operating in the presence of the DMC60 blade antenna. The blade antenna was 48″ aft of the TCAS antenna. Similar error curves for the TCAS antenna operating in the presence of the AT741 blade are given in Figures 4.16–4.19.

It is seen that the blade antenna has a significant influence on the performance of the two TCAS systems. The most obvious effect is the oscillatory behavior of the SPA error curve over $[-180:180]$ range, as opposed to oscillations only over the $[-180:-90,\ 90:180]$ range for the CRA TCAS. This difference is due the way in which the received signal from each element is processed by the CRA system. Recall that the receiving antennas in this simulation are modeled as radiators. Thus, to estimate the bearing of the intruder, the CRA TCAS transmits four beams in the assigned directions. The blade, which is between the TCAS and tail, will not affect beam 0 except in the backlobe region. Beams 1 and 3, pointing to the sides, are also only slightly affected. Only beam 2, which illuminates the blade directly, is severely distorted. This is shown in Figure 4.20, where the distortion of the TCAS pattern by the VHF blade is apparent.

Although the blade re-radiates whenever the TCAS is in operation, the radiation is strongest only when illuminated by beam 2. Hence, the two highest received signals are still via beams 0 and 1 or 0 and 3 in the forward half. The radiation by the blade in the $-90°$ to $90°$ azimuth sector is not strong enough to change the two highest signals. Therefore, the distortion of the error curve by the blade is minimal

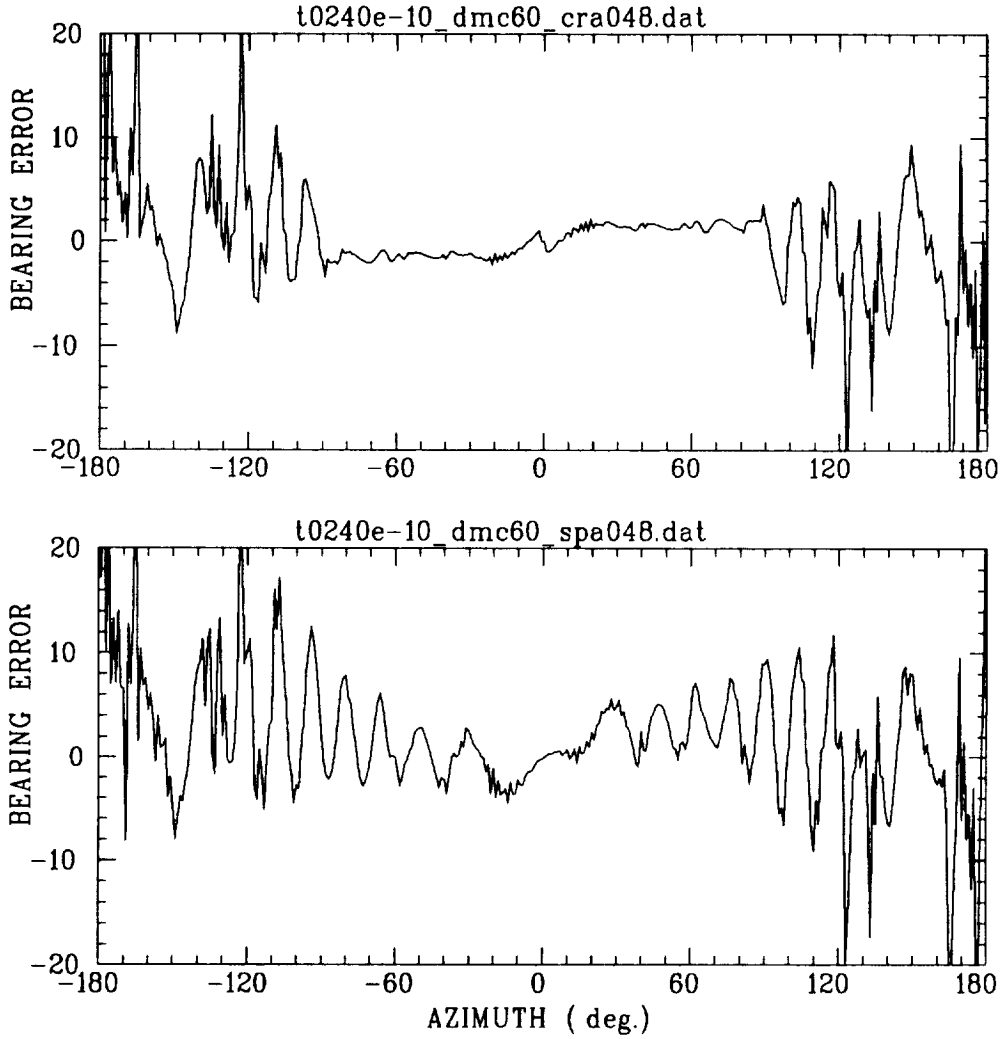

Figure 4.12: Error curves for CRA (top) and SPA (bottom) TCAS in the presence of DMC60 blade antenna 48″ aft. The TCAS antenna was mounted 289″ from the nose on Boeing 737-300. Elevation = −10°.

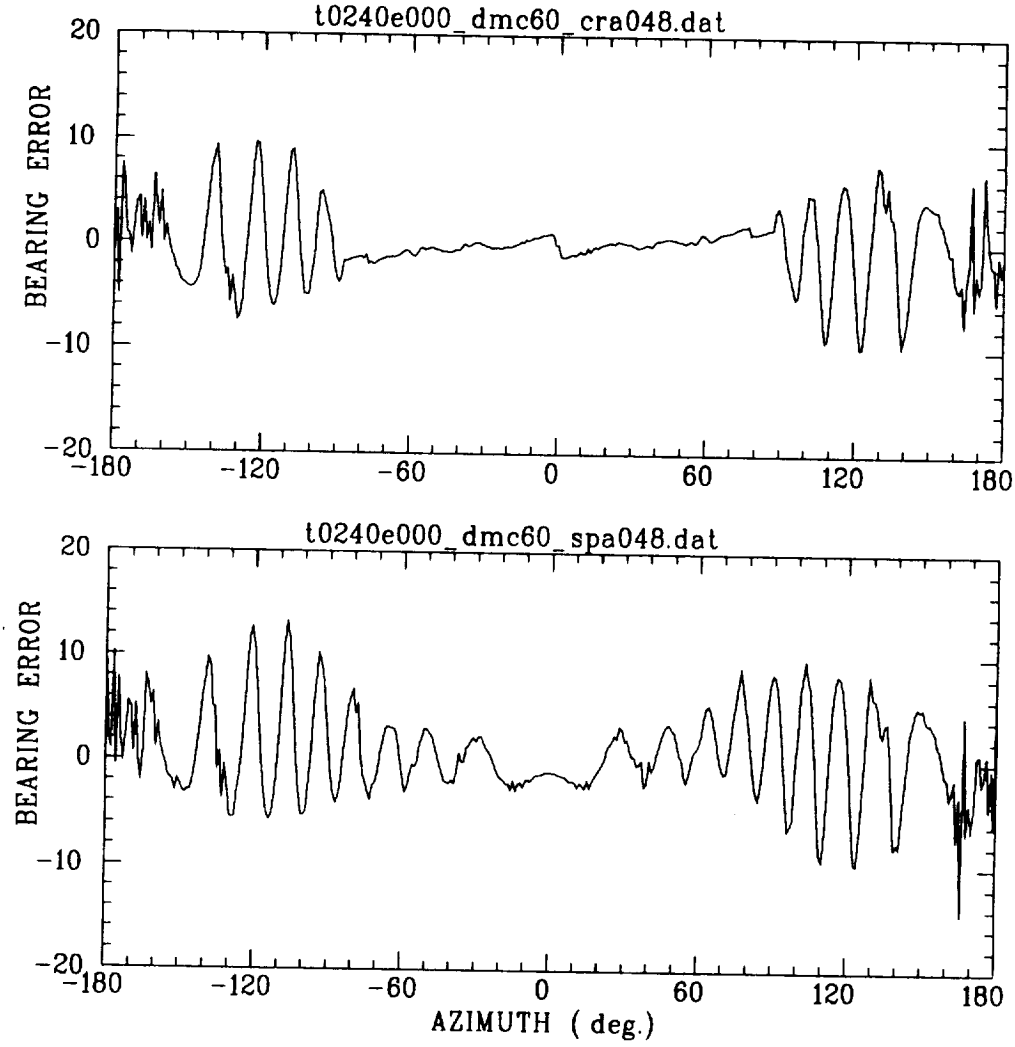

Figure 4.13: Error curves for CRA (top) and SPA (bottom) TCAS in the presence of DMC60 blade at 0° elevation. Aircraft setup same as Figure 4.12.

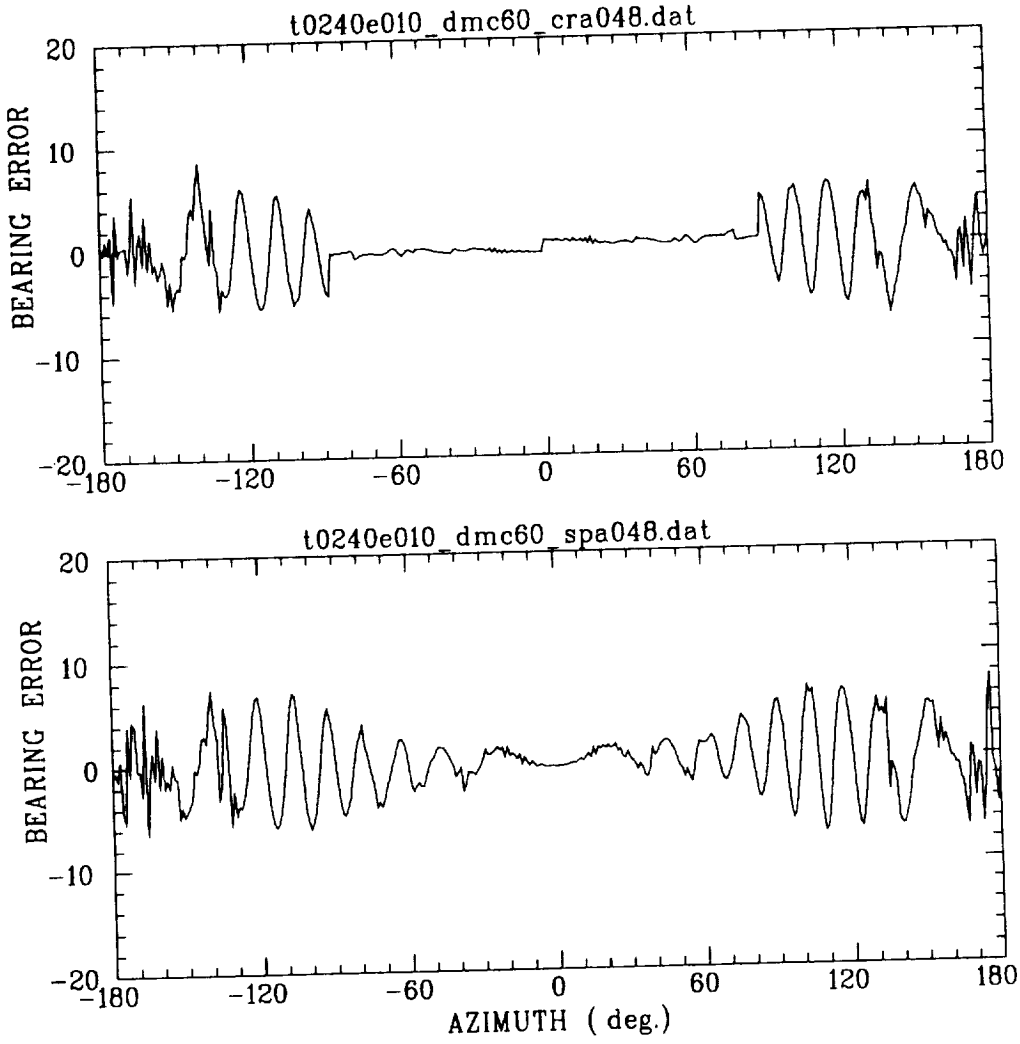

Figure 4.14: Error curves for CRA (top) and SPA (bottom) TCAS in the presence of DMC60 blade, at 10° elevation. Aircraft setup same as Figure 4.12.

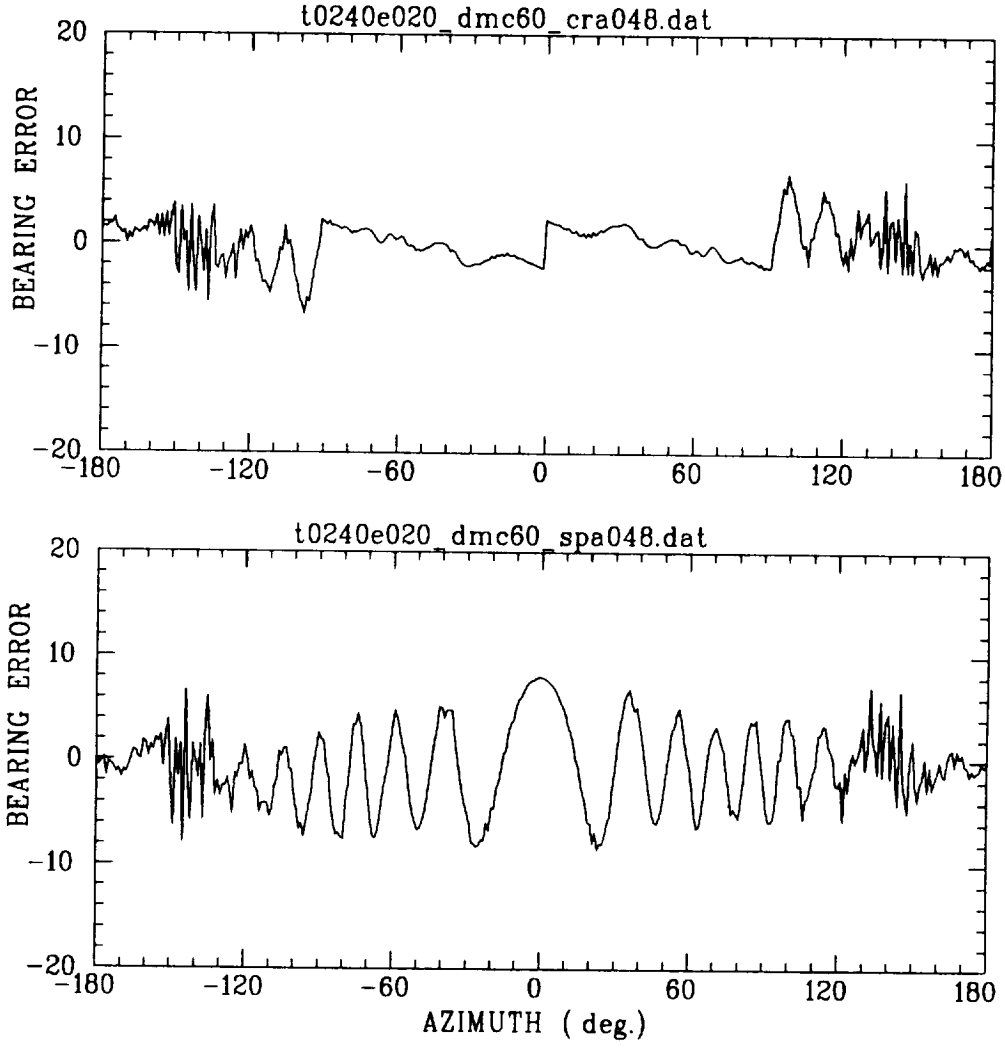

Figure 4.15: Error curves for CRA (top) and SPA (bottom) TCAS in the presence of DMC60 blade, at 20° elevation. Aircraft setup same as Figure 4.12.

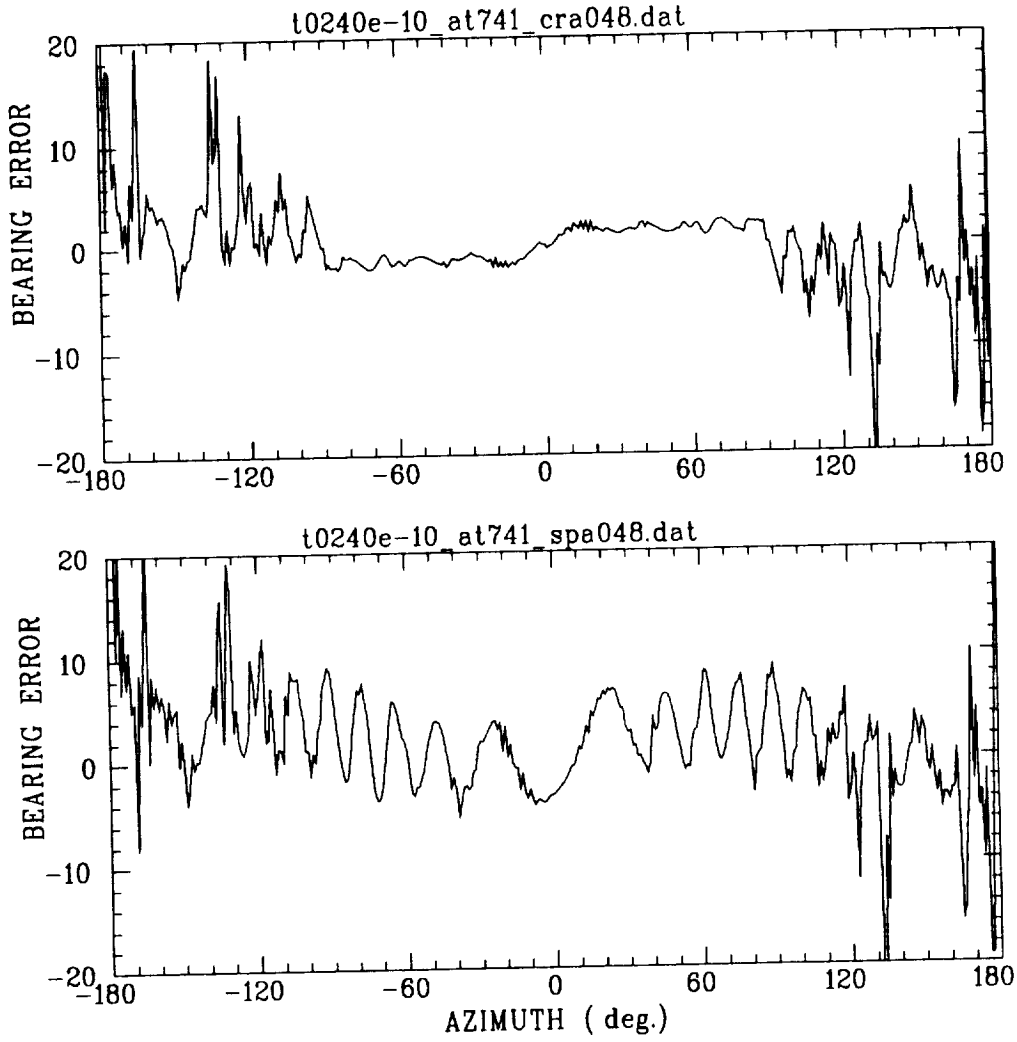

Figure 4.16: Error curves for CRA (top) and SPA (bottom) TCAS in the presence of AT741 blade antenna 48″ aft. The TCAS antenna was mounted 289″ from the nose on Boeing 737-300. Elevation = −10°.

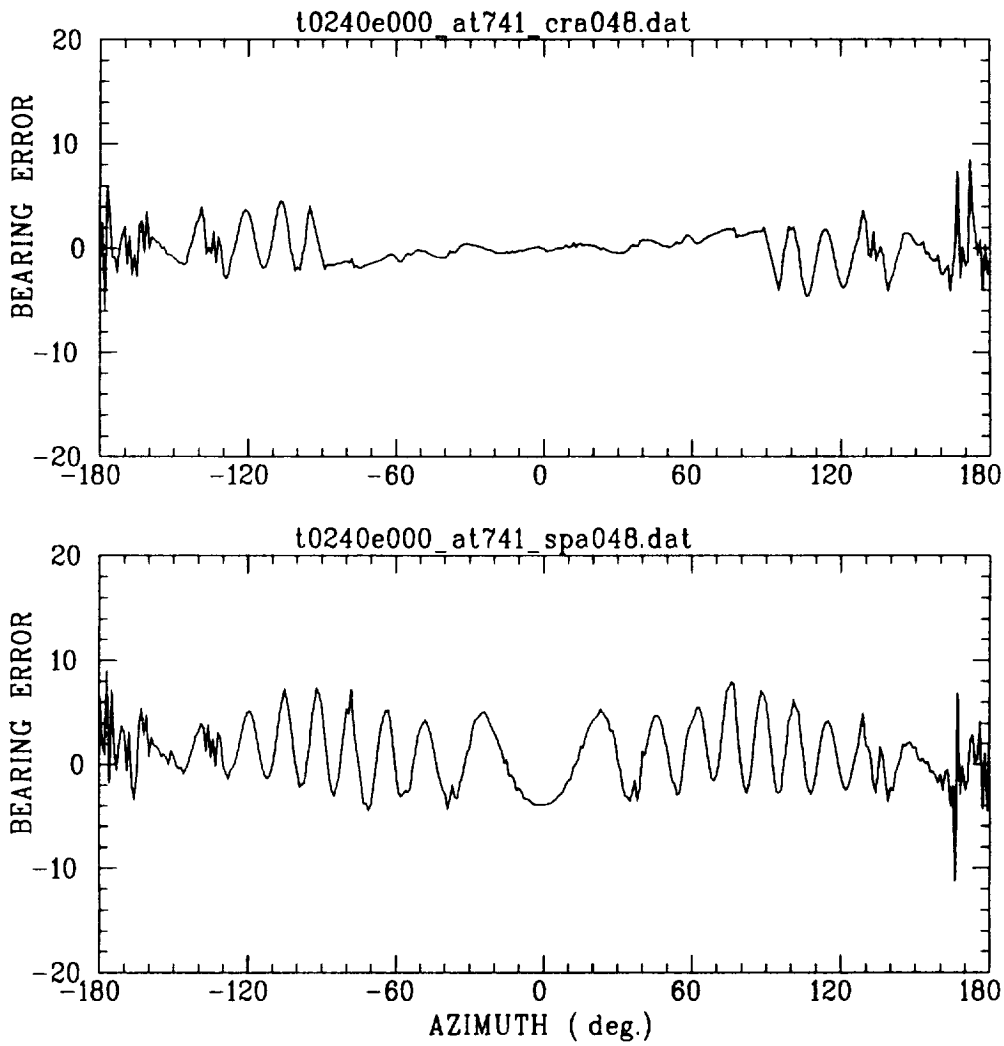

Figure 4.17: Error curves for CRA (top) and SPA (bottom) TCAS in the presence of AT741 blade, at 0° elevation. Aircraft setup same as Figure 4.16.

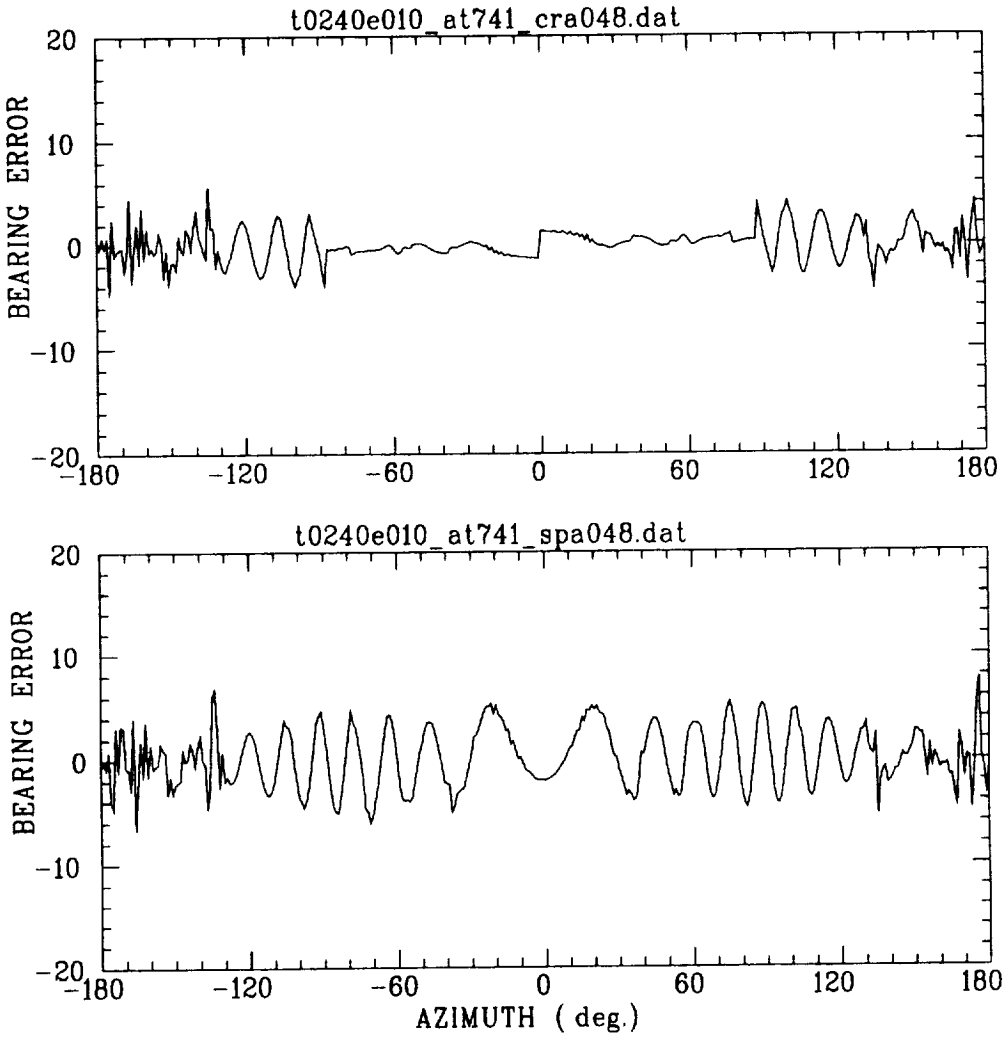

Figure 4.18: Error curves for CRA (top) and SPA (bottom) TCAS in the presence of AT741 blade, at 10° elevation. Aircraft setup same as Figure 4.16.

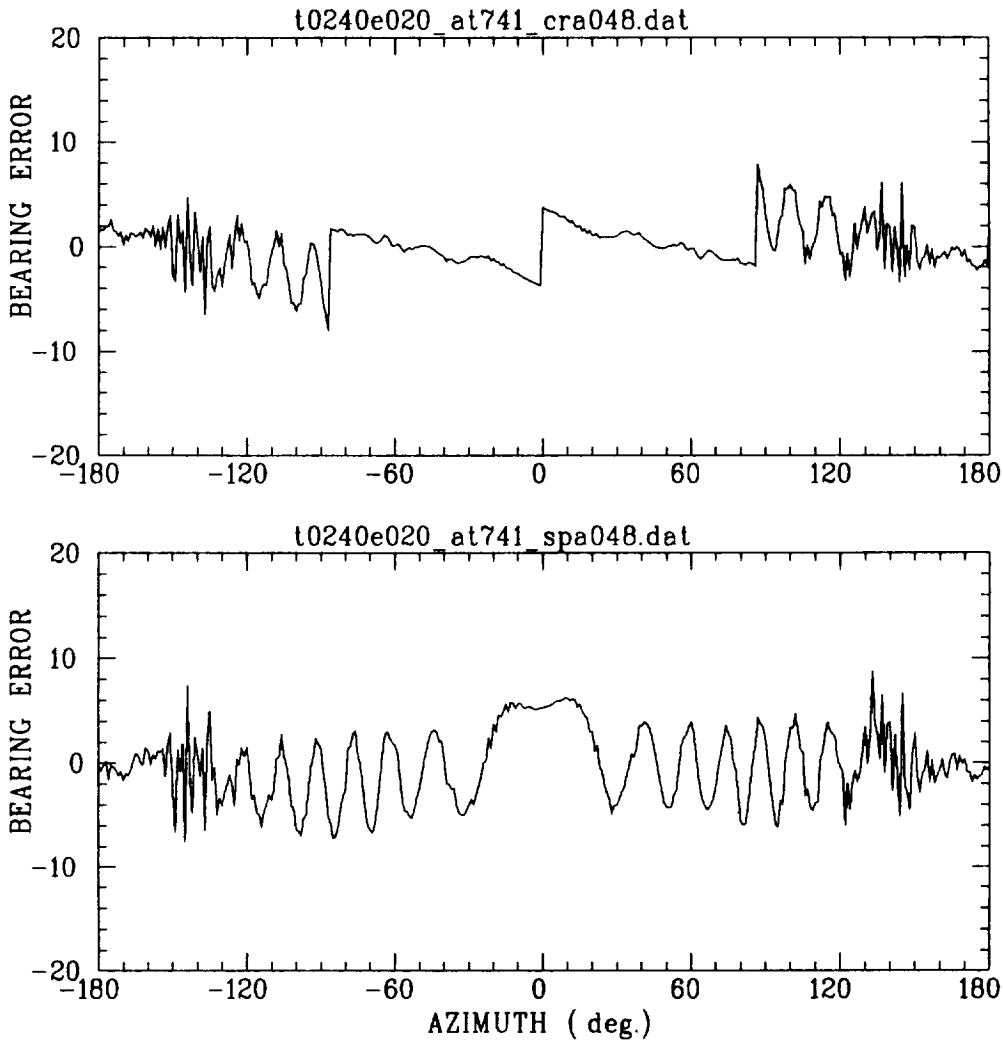

Figure 4.19: Error curves for CRA (top) and SPA (bottom) TCAS in the presence of AT741 blade, at 20° elevation. Aircraft setup same as Figure 4.16.

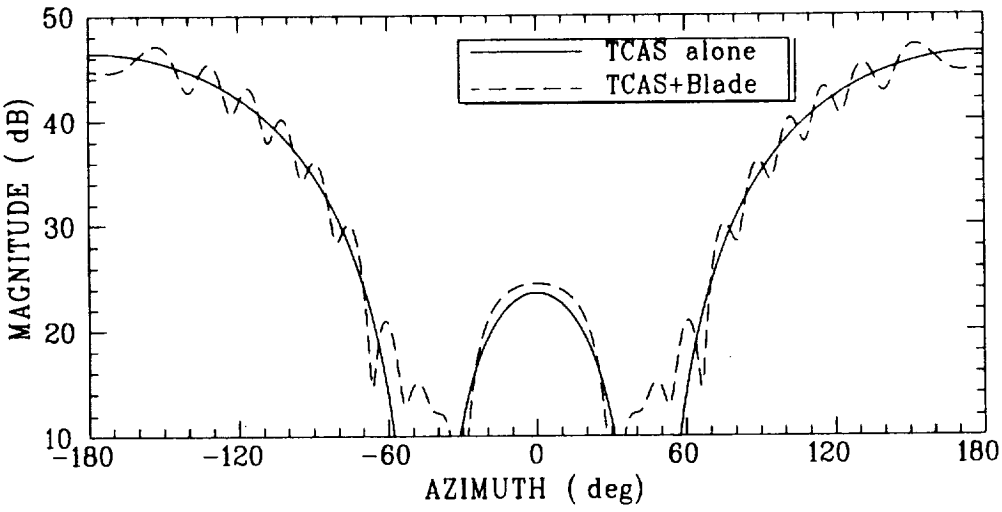

Figure 4.20: Distortion of CRA beam 2 due to re-radiation by the DMC60-1 blade antenna.

in the forward half is small. Of course, the error introduced by the blade in the rear quadrant is larger, because the blade is now illuminated by beam 2, which is the strongest beam in the rear quadrant. On the other hand, the SPA antenna always illuminates the blade via sum and difference beams, which are both omnidirectional, and differ in amplitude by only 3 dB. Thus, the effect of the blade is visible over the whole azimuth region as shown.

The behavior of the TCAS in elevation is quite similar for both systems. The radiation from the blade drops off approximately as $\sin\theta$ and hence, their error magnitude decreases slightly. It is interesting to note that the error magnitude is comparable for both the AT741 and DMC60-1 blade antennas.

Next, the behavior of the two TCAS systems was simulated at various separations from the blade antennas. For this study, the TCAS antenna was held fixed at 289″ from the nose on the Boeing 737-300. The blade antenna was placed at increasing distances aft of the TCAS antenna, starting at 24″ (2.2λ) from the TCAS up to 168″ (15.5λ). Error curves were computed via UTD for elevations ranging from 0° to 20° in 5° steps and averaged to find the standard deviation of the bearing error. The

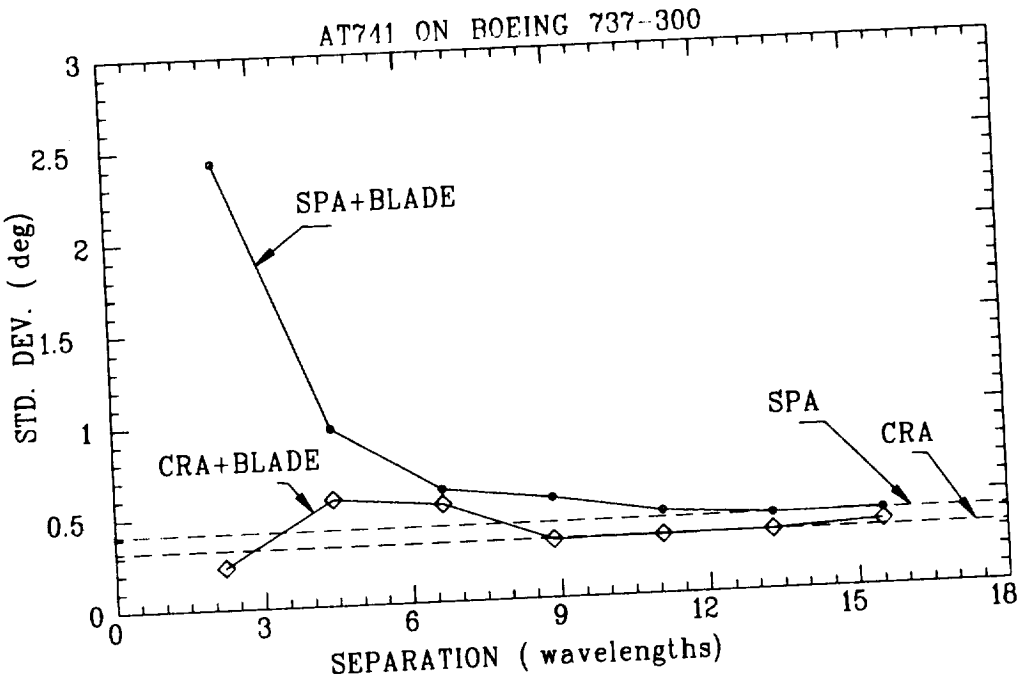

Figure 4.21: Variation of standard deviation with distance between the TCAS antenna and AT741 blade. The TCAS antenna was held fixed at 289″ from nose on Boeing 737-300.

results of this high frequency computation are given for the AT741 in Figure 4.21 and the DMC60-1 in Figure 4.22.

To verify these high frequency results, error curves were calculated via an independent moment method computation. For this case, the blade antenna was modeled by a flat plate and the antennas by thin wires. The curvature of the fuselage was ignored and the fuselage itself was then replaced by an infinite ground plane. Next, using image theory, the ground plane was removed and the wire monopoles and the blade antennas were augmented with their images. The geometry of the moment method model for the AT741 antenna in the presence of the SPA antenna is depicted in Figure 4.23. The model for the DMC60-1 is similar and is shown in Figure 4.24. Note that the latter figure depicts CRA array. Radiation patterns were then computed for each TCAS antenna in the presence of each blade. By processing these patterns as already described, the standard deviation of the bearing error was com-

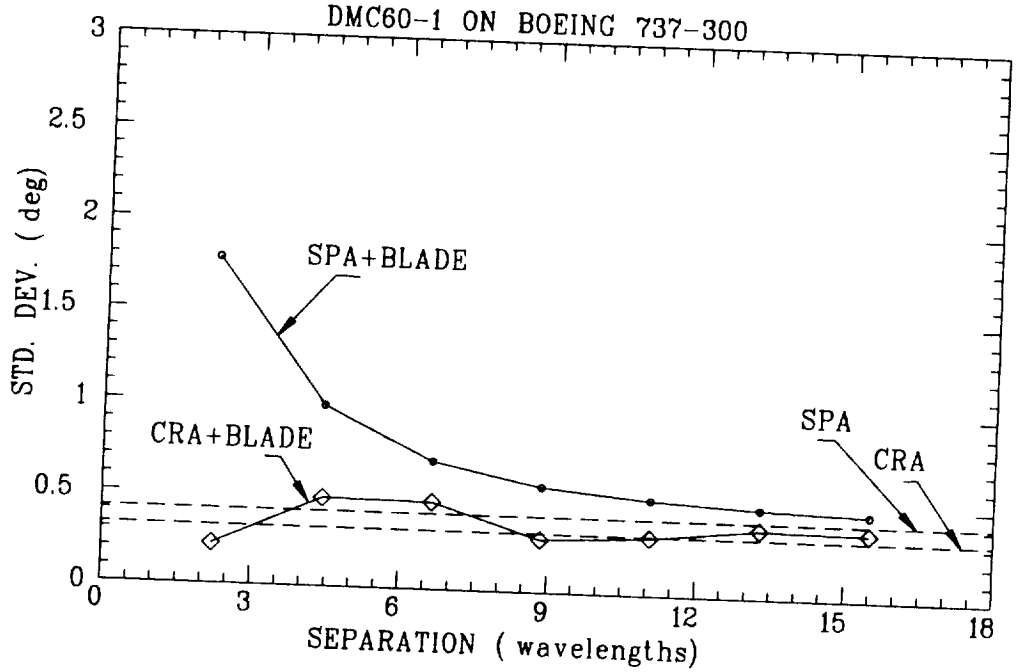

Figure 4.22: Variation of standard deviation with distance between the TCAS antenna and DMC60-1 blade. The TCAS antenna was held fixed at 289″ from nose on Boeing 737-300.

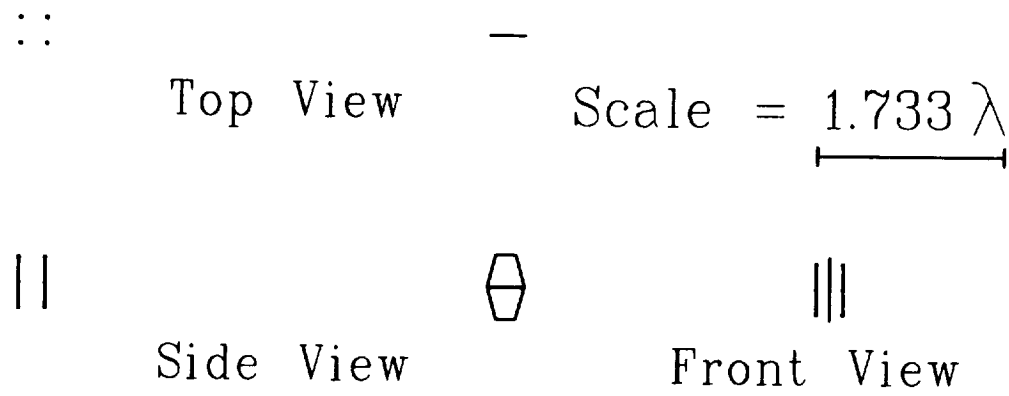

Figure 4.23: Moment method model for the AT741 antenna 48″ aft of the SPA TCAS antenna.

puted. It is noted here that, due to the modeling procedure, only positive elevations are valid. Hence the standard deviation was computed only for elevations in 0° to 20° range. The process was repeated at various elevations and separations to obtain the standard deviation of the bearing error for each location of the blade antenna. The standard deviation curves for the AT741 antenna are given in Figure 4.25 and the DMC60-1 blade in Figure 4.26.

The results are very interesting. Firstly, it is seen that the UTD and MM models agree. The minor differences in the curves for the high and low frequency models can be attributed to the differences in the models used — like flat plates versus monopoles for the antennas, flat versus the curved ground plane etc. Secondly, the SPA error monotonically decreases as the distance is increased from the TCAS antenna. In case of the CRA system, it is small to start with, increases in a region about 4 to 6 wavelengths behind the TCAS, and then decreases again. Finally, it is seen that, in the case of the UTD models on the Boeing 737-300, given in Figures 4.21 and 4.22, that the error approaches that of the TCAS antenna alone (dashed line) as δ increases. It is noted that the bearing error due to an isolated TCAS is close to zero. The error is identically zero for the intruder at the same elevation as the lookup table, and small for other elevations.

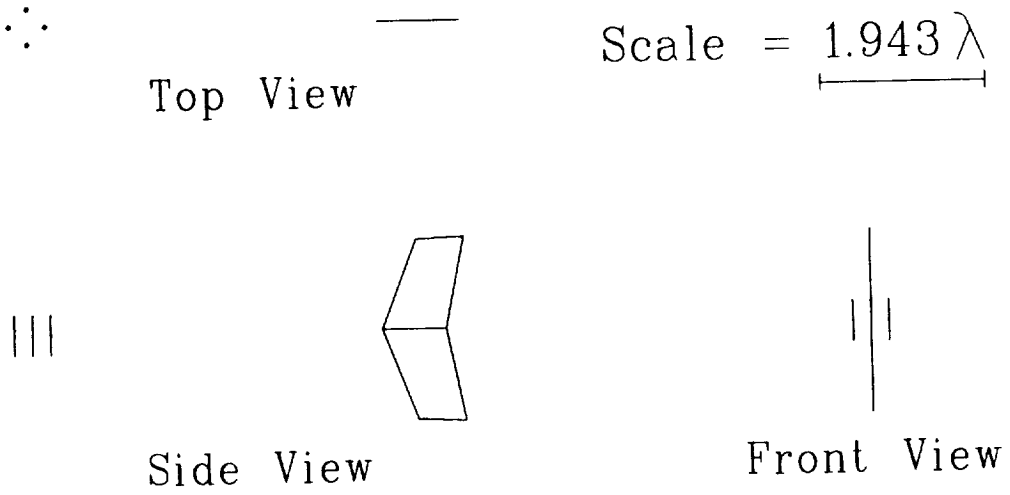

Figure 4.24: Moment method model for the DMC60-1 antenna 48″ aft of the CRA TCAS antenna.

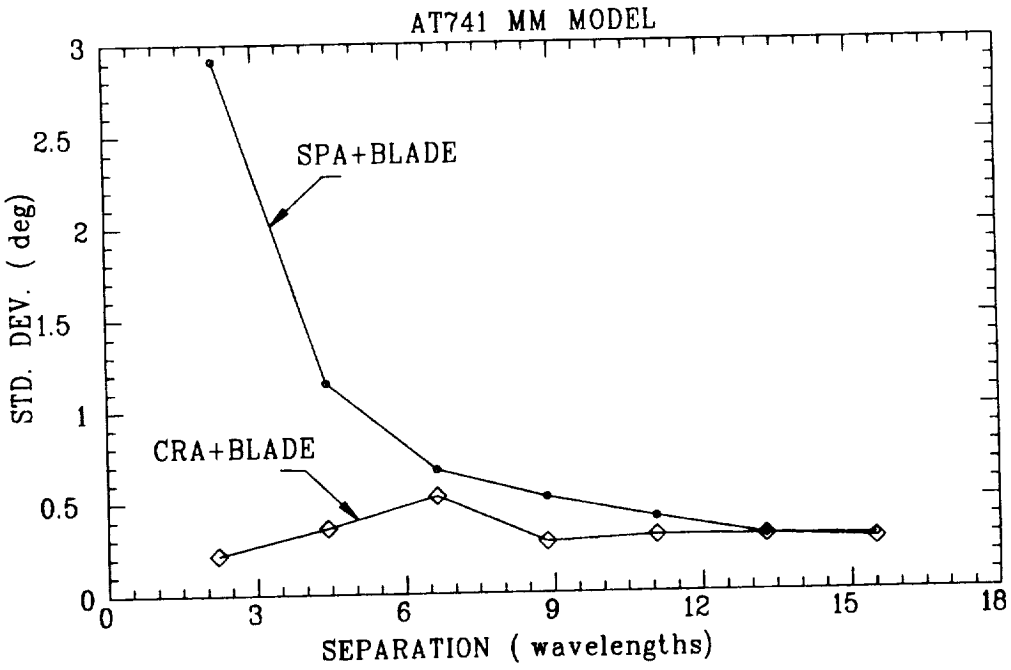

Figure 4.25: Moment method computation to verify the results of Figure 4.21. Fuselage was replaced by a flat ground plane and blade modeled as a flat plate.

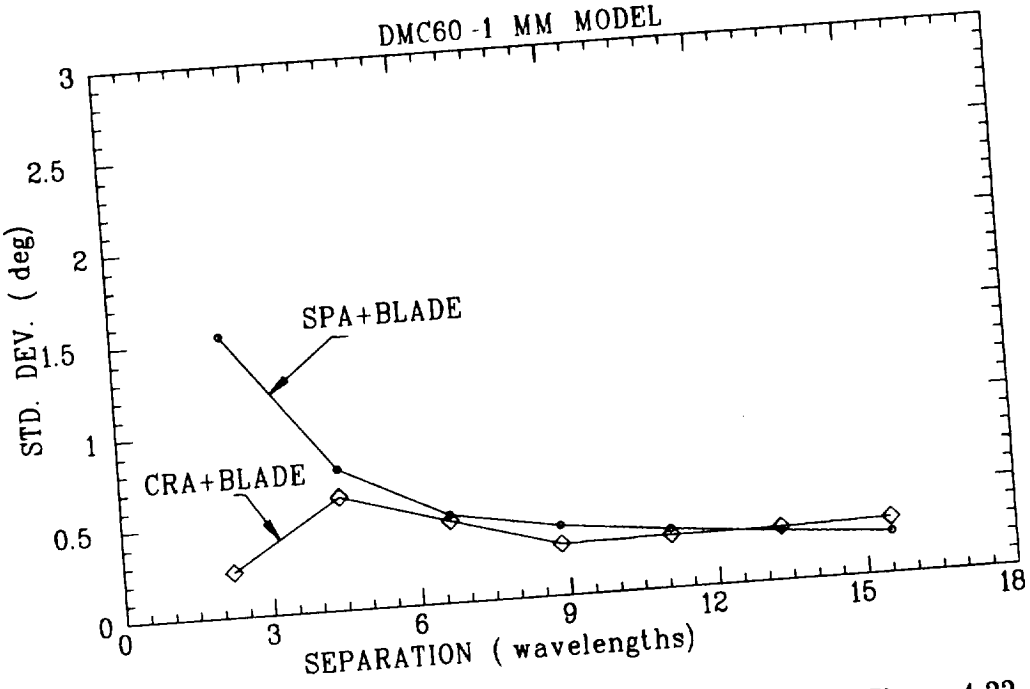

Figure 4.26: Moment method computation to verify the results of Figure 4.22. Fuselage was replaced by a flat ground plane and blade modeled as a flat plate.

One immediately notices that the standard deviation of the bearing error σ_s for the SPA TCAS increases as δ^{-1}, where δ is the separation between the TCAS antenna and the blade antenna. This is true for both MM and UTD models, for the AT741 as well as the DMC60 blade. On the other hand, the standard deviation of the CRA system actually decreases very close to the antenna. This is a result of the mutual coupling between the two antennas. As δ changes, both the amplitude and phase of the transmitted signal from the TCAS are modified by the induced currents on the blade. When δ is small (less than about 2λ), the amplitude of the TCAS beam is not affected as much as the phase is.

It is also seen that the error of the TCAS system near the DMC60-1 is somewhat smaller than the AT741. This is surprising at first, because the AT741 is about 3″ tall; whereas, the DMC60-1 is about 12″ tall. This is due to the magnitude of the induced currents which depend upon the *separation* as well as the *electrical* size of the blade antenna.

Thus, the performance of the *CRA system suffers little in the presence of the blade antenna.* On the other hand, *the SPA antenna is greatly affected* by these phase variations, as seen from these results. Hence, one may conclude that, to keep the standard deviation of the bearing error less than 1°, it is necessary that the SPA antenna be at least 4λ from any other scatterers aft. This is not the case with the CRA antenna, which exhibits superior performance in the presence of nearby scatterers.

Chapter 5

Effect of Engines

5.1 Introduction

Engines play an important role in the performance of the TCAS. The effect of the engines is especially noticeable when an engine inlet is directly illuminated by the TCAS antenna. To better understand the true scattering of the engine cavity, the inlet is modeled by an open-ended circular waveguide cavity in free space. It is assumed to be excited by an electromagnetic plane wave. The waveguide is semi-infinite and has an interior termination which may be modeled as a flat plate (short circuit), a dielectric material, or a flat blade disk optionally with a conical or hemispherical hub. Some of these geometries are depicted in Figure 5.1.

In the analysis presented below, primary emphasis is placed on the circular waveguide, because it approximates the structure of the engine most closely. Note that the terms, engine and inlet, are used interchangeably. In all cases studied here, the termination of the circular waveguide is assumed to be a PEC flat plate. The aircraft model used in this study is the Boeing 727-200, and the engine on top of the fuselage is of interest. Results are presented for both CRA and SPA systems for selected elevations in the lit region in the forward half of the airplane.

It is shown that the model of the engine plays a more prominent role on the performance of the SPA system than the CRA. Standard deviation curves to assess the systems are also given. These curves clearly demonstrate that the spiral phase

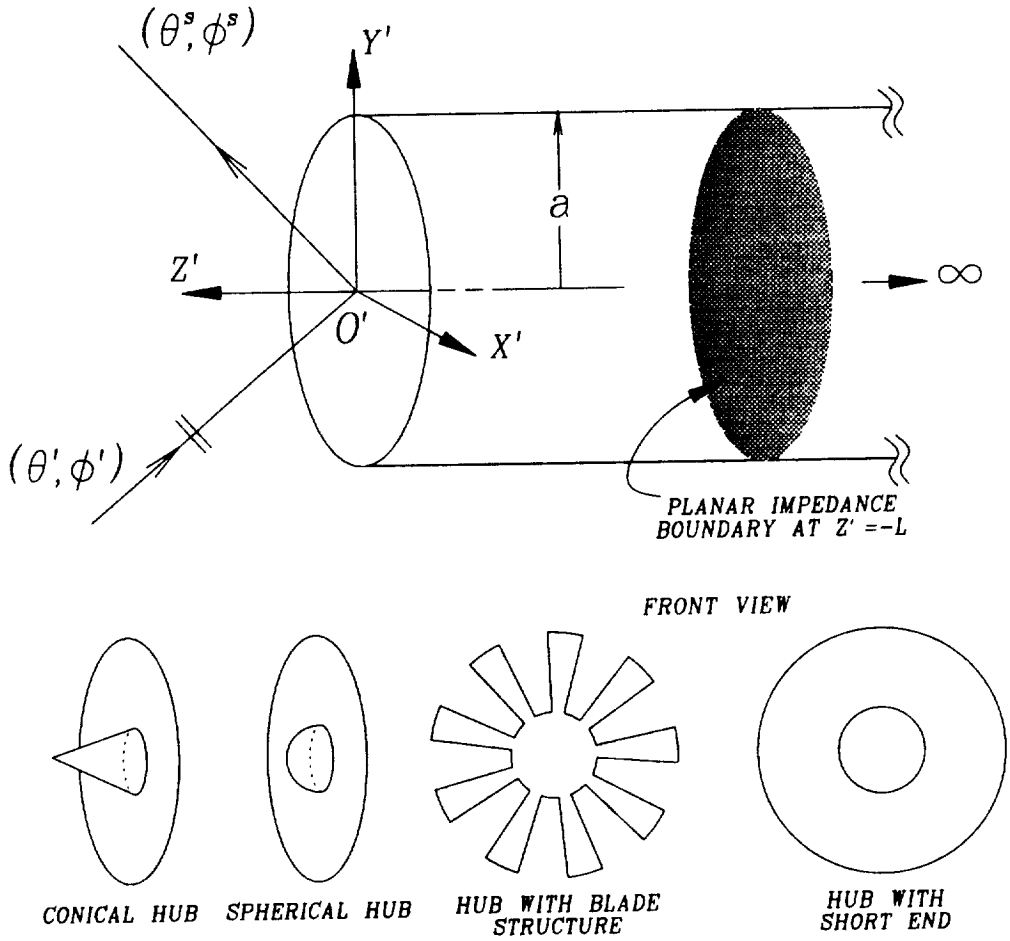

Figure 5.1: Some possible waveguide and termination geometries for modeling the aircraft engines.

TCAS is more susceptible to adverse engine effects than the amplitude system. This is especially true when the engine inlet is in the lit region of the TCAS antenna. It is seen that the overall errors are slightly smaller, and more uniform. Finally, it is noted that the performance in the forward half may be slightly improved if the TCAS antenna is closer to the nose, thus utilizing the natural curvature of the fuselage to cause some blockage of the engine inlet illumination.

5.2 Scattering by a Waveguide

The inlet analysis employs a combination of high frequency techniques such as the uniform geometrical theory of diffraction and its modifications based on the equivalent current method (ECM) as well as the physical theory of diffraction (PTD). These are used in conjunction with the self-consistent multiple scattering method (MSM) [18]. This method is presented in more detail in Appendix C. The analysis is fairly general and has been successfully applied to circular as well as rectangular waveguides.

In the hybrid asymptotic modal method, the self-consistent scattering matrix formulation is used to describe the fields inside the waveguide cavity. This includes the multiple interactions between the open end and termination. High frequency techniques are used to obtain the modal scattering matrices that describe the coupling between the cavity modes and the external region via the open end, and the interior modal reflection from the open end. The modal scattering matrix describing the reflection from the waveguide cavity termination may be found in closed form for the flat plate or dielectric termination. Physical optics is used to approximately compute the reflection matrix from disk/blade/hub terminations. The external scattering by the rim at the open end is found by replacing the rim with equivalent edge currents. These edge currents are found approximately by incorporating the UTD diffraction coefficients. First order as well as second order diffraction effects can be included in the computation.

5.3 Engine Model

The engine is modeled as a terminated circular waveguide cavity. The scattered fields of the terminated circular waveguide are calculated using the MSM formulation, introduced above. The computation is facilitated by a modified version of software titled NEAR_CIRC, which has been developed at the Ohio State University ElectroScience Laboratory [20, 19]. This program computes the bistatic scattered fields from a rectangular or circular semi-infinite waveguide terminated inside. The scattered fields are output as: $E_{\theta\theta}, E_{\theta\phi}, E_{\phi\phi}$, and $E_{\phi\theta}$, where the first subscript refers to the polarization of the incident plane wave and the second subscript to that of the scattered field. It is assumed that the amplitude of the incident plane wave is unity.

Figure 5.2 depicts the geometry of the engine mounted on an airplane. The aircraft coordinate system, the TCAS coordinate system as well as the engine's local coordinate system are shown. The coordinate system of the TCAS is the same as the pattern coordinate system for azimuth cuts.

The scattered fields of the engine (inlet) are incorporated into the patterns of the TCAS antenna via superposition. This must be done carefully because of the various coordinate systems involved. The scattered fields due to the engine are

$$\begin{bmatrix} E^e_{\theta l} \\ E^e_{\phi t} \end{bmatrix} = [Q_l][R_{lc}][Q'_c] \begin{bmatrix} E^c_{\theta e} \\ E^c_{\phi e} \end{bmatrix} e^{-jk\hat{r}\cdot\bar{r}_{ac}}. \tag{5.1}$$

Here, $E^e_{\theta l}, E^e_{\phi l}$ are the scattered fields of the engine in the TCAS coordinate system, $E^e_{\theta e}, E^e_{\phi c}$ are the scattered fields in the far zone of the inlet, with the phase referred to the center of the engine. $[Q_l]$ denotes the transformation matrix from rectangular to spherical coordinates with reference to the TCAS coordinate system, such that

$$[Q_l] = \begin{bmatrix} \cos\theta\cos\phi & \cos\theta\sin\phi & -\sin\theta \\ -\sin\phi & \cos\phi & 0 \end{bmatrix} \tag{5.2}$$

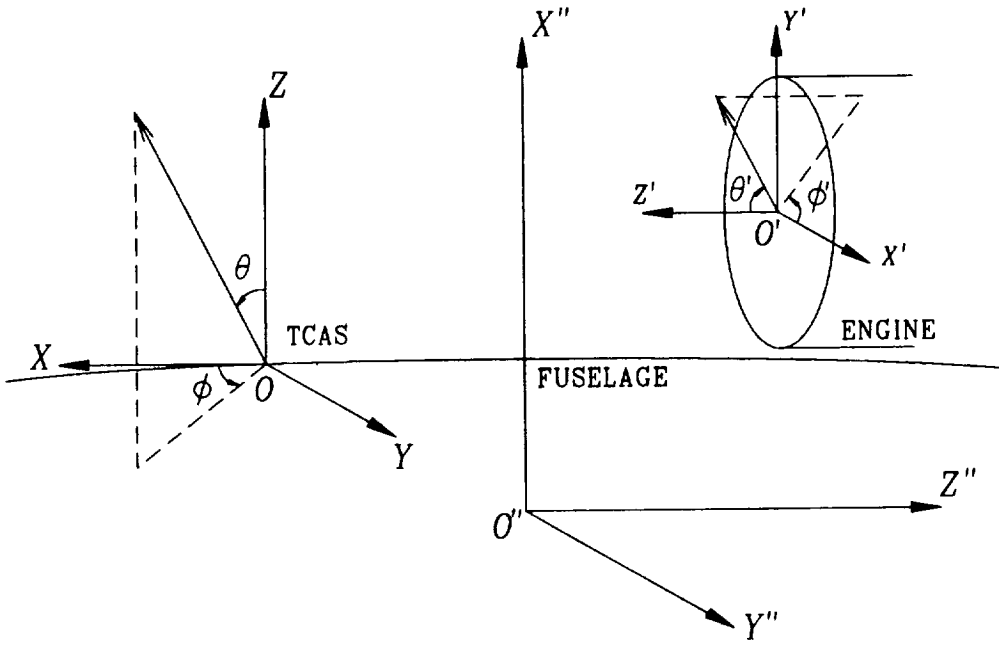

Figure 5.2: Geometry for modeling the engines.

The spherical to rectangular transformation with respect to the engine center is given by

$$[Q'_e] = \begin{bmatrix} \cos\theta' \cos\phi' & -\sin\phi' \\ \cos\theta' \sin\phi' & \cos\phi' \\ -\sin\theta' & 0 \end{bmatrix}. \tag{5.3}$$

Finally, $[R_{te}]$ is a rotation matrix, which for the top mounted TCAS is simply given by

$$[R_{te}] = \begin{bmatrix} 0 & 0 & 1 \\ 1 & 0 & 0 \\ 0 & 1 & 0 \end{bmatrix}. \tag{5.4}$$

From Figure 5.1, one finds that

$$\bar{r}_{ae} = \hat{r}_{ae} r_{ae} = \bar{e} - \bar{a}, \tag{5.5}$$

$$\bar{e} = \hat{x} x_e + \hat{y} y_e + \hat{z} z_e, \qquad \text{and} \tag{5.6}$$

$$\bar{a} = \hat{x} x_a + \hat{y} y_a + \hat{z} z_a \tag{5.7}$$

referring to the coordinates of the center of the inlet and the TCAS antenna, respectively. The incident direction (θ', ϕ') of the plane wave at the inlet is given

C-2

by

$$\theta' = \cos^{-1}(\hat{r}_{ac} \cdot \hat{z}'), \qquad \text{and} \tag{5.8}$$

$$\phi' = \tan^{-1}\left(\frac{\hat{r}_{ac} \cdot \hat{x}'}{\hat{r}_{ae} \cdot \hat{y}'}\right). \tag{5.9}$$

Finally, note that, for a given pattern direction (θ, ϕ), the corresponding direction of the scattered field in the inlet coordinate system is given by (θ_s, ϕ_s), where

$$\theta_s = \cos^{-1}(\sin\theta\cos\phi), \qquad \text{and} \tag{5.10}$$

$$\phi_s = \tan^{-1}\left(\frac{\cos\theta}{\sin\theta\sin\phi}\right). \tag{5.11}$$

$E^e_{\theta e}$ and $E^e_{\phi e}$ are the components of the scattered field of the engine (referred to engine center), suitably modified to account for the excitation by the TCAS antenna. This may be written as

$$\begin{bmatrix} E^e_{\theta e} \\ E^e_{\phi e} \end{bmatrix} = \begin{bmatrix} E_{\theta\theta} & E_{\theta\phi} \\ E_{\phi\theta} & E_{\phi\phi} \end{bmatrix} \begin{bmatrix} A^t_{\theta e} \\ A^t_{\phi e} \end{bmatrix} \tag{5.12}$$

Here, $A^t_{\theta e}$ and $A^t_{\phi e}$ are the scaled incident amplitudes of the plane wave from the TCAS antenna. $E_{\theta\theta}, E_{\theta\phi}, E_{\phi\phi}$, and $E_{\phi\theta}$ are the scattered fields from the inlet, with the first subscript indicating the polarization of the incident plane wave and the second subscript that of the scattered field.

Recall that the excitation of the engine is via sum and difference beams for the SPA system and the four beams for the CRA TCAS which were derived in Sections 2.2 and 2.3. To get the correct amplitude and phase of the incident plane wave, one first computes the fields due to the TCAS antenna, and converts them to the coordinate system of the inlet. Hence, one finds that

$$\begin{bmatrix} A^t_{\theta e} \\ A^t_{\phi e} \end{bmatrix} = ([Q_t][R_{te}][Q'_e])^{-1} \begin{bmatrix} E^t_{\theta e} \\ E^t_{\phi e} \end{bmatrix} \tag{5.13}$$

where, $E^t_{\theta e}, E^t_{\phi e}$ are the components of the radiated field from the TCAS at the engine location.

5.4 TCAS Performance

The performance of the TCAS is re-evaluated in the presence of the engine using the above models. This may be accomplished via two equivalent methods. One can recompute each element pattern in the presence of the inlet and process the received signals as before; alternately, the inlet scattered fields can be computed by illuminating it by the four CRA beams or the sum and difference beams of the SPA system in turn. These can then be directly superimposed on the receiver beams computed for the same geometry without the engine inlet. The latter approach is adopted here for its flexibility and lesser computations.

In case of CRA array, there are four beams, each pointing in a different direction. Hence, the illumination of the inlet is different for each beam, and so are the scattered fields. Thus, the CRA or SPA beams are created by weighting the monopoles in turn to compute the field incident on the inlet. The scattered fields are obtained via the MSM method and stored. These fields are then superimposed to obtain the pattern of the TCAS antenna in the presence of the engine. Note that, the received signal at the TCAS antenna is simulated by computing the transmitted field, which because of reciprocity are identical.

The engine on top of the Boeing 727-200 was modeled via this procedure to check the validity of the results. The model of the engine consisted of a circular waveguide, terminated by a PEC plate. The radius of the waveguide is 2.89λ. The depth was 2.77λ, which is approximately the depth of the blades from the inlet. The TCAS antenna was placed successively at 60″ intervals at distances 100″ up to 400″ from the nose on top of the fuselage.

The scattering from the center engine of the Boeing 727-200 is shown in Figure 5.3 for 0° and 10° elevations. The incident field at the engine was from beam 2 of a CRA TCAS, located 340″ from the nose. It is noticed that the scattering from the engine is more uniform, due to the large number of modes inside the waveguide structure.

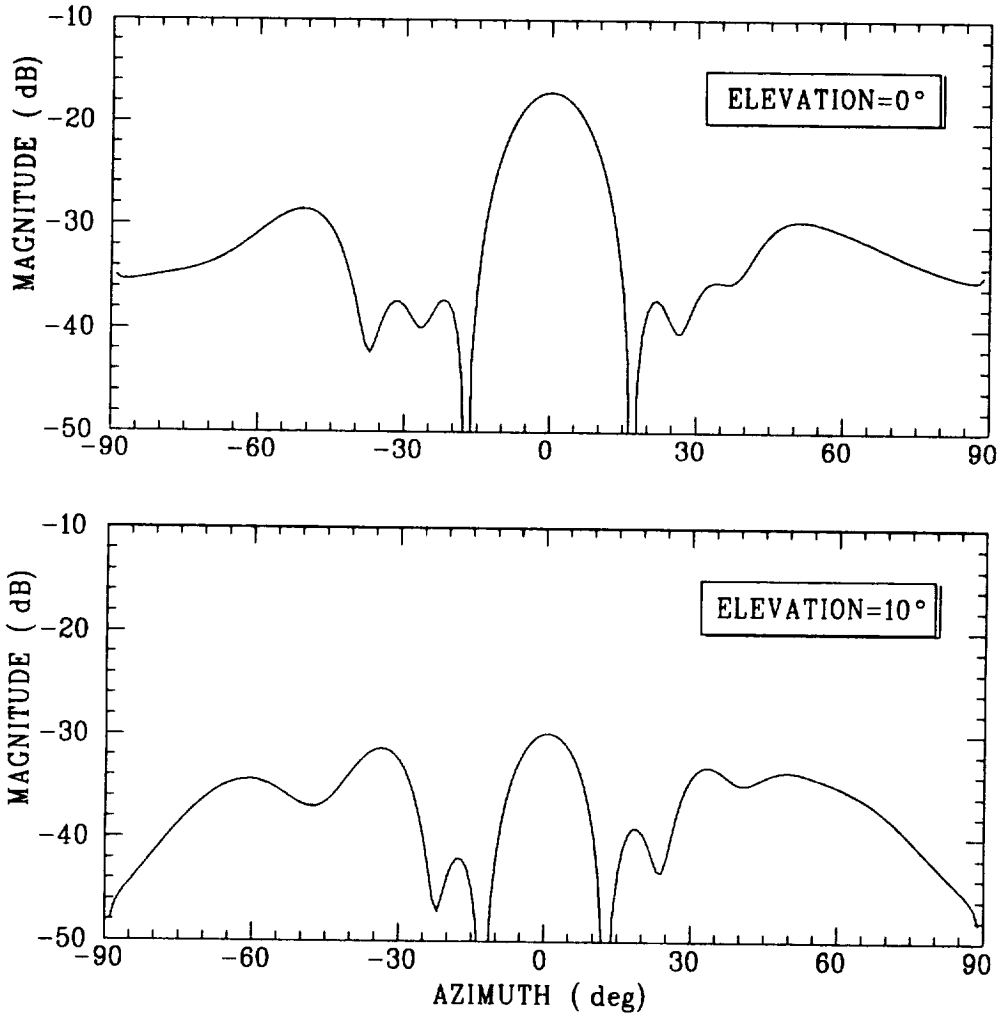

Figure 5.3: Scattered fields from a terminated circular inlet at 0° (top) and 10° (bottom). The inlet was excited by beam 2 of the CRA TCAS placed 340″ from nose on a Boeing 727-200.

Error curves presented in Figures 5.4 and 5.5 depict the effect of the engine model on the performance of the two TCAS systems at 0° for the engine modeled by the circular waveguide and closed rectangular PEC box, respectively. The TCAS antenna was placed at location 0340 (same distance in inches from the nose) on top of the Boeing 727-200. Similarly, Figures 5.6 and 5.7 and Figures 5.8 and 5.9 depict the error curves for the same location at 10° and 20° elevations, respectively.

It is seen that from these results that the error curves are comparable, especially at lower elevations. This is due to the large backscatter from the waveguide termination. It is also noticed that the bearing error due to the waveguide model is more uniform; i.e., one does not see the specular, localized regions of higher errors as in the flat plate model. In the case of the plate model, the highest error drops quite rapidly. This is not the case with the waveguide model, whose error tends to be more uniform. This is expected because, the waveguide has many propagating higher order modes, which give rise to higher side lobe levels. Hence, the distortion of the beams is more uniform, and the error tends to be smaller.

To study if the performance of the SPA system could be enhanced by moving it forward, standard deviation curves were generated for each TCAS location spanning 100″ to 400″ at 60″ intervals along the top of the Boeing 727-200 fuselage. The results are depicted in Figure 5.10. It must be noted that, due to modeling constraints, only positive elevation are valid. Thus, the standard deviation was calculated in the forward sector, $-90°$ to 90° for elevations 0° to 20° only. The figure also shows the tilt angle of the antenna normal towards the nose of the airplane. It is seen that the minimum error occurs around station 160, where the tilt is about 7.5°. This is close to the optimal location at 140, obtained with the plate model for the top engine. Comparing Figures 5.10 and 3.18, it is noticed that the overall errors are less for the TCAS systems when the top engine is modeled by circular waveguide. The general trends are still the same—the standard deviation of the error decreases and then increases as one increases the distance from the nose. The standard deviation of

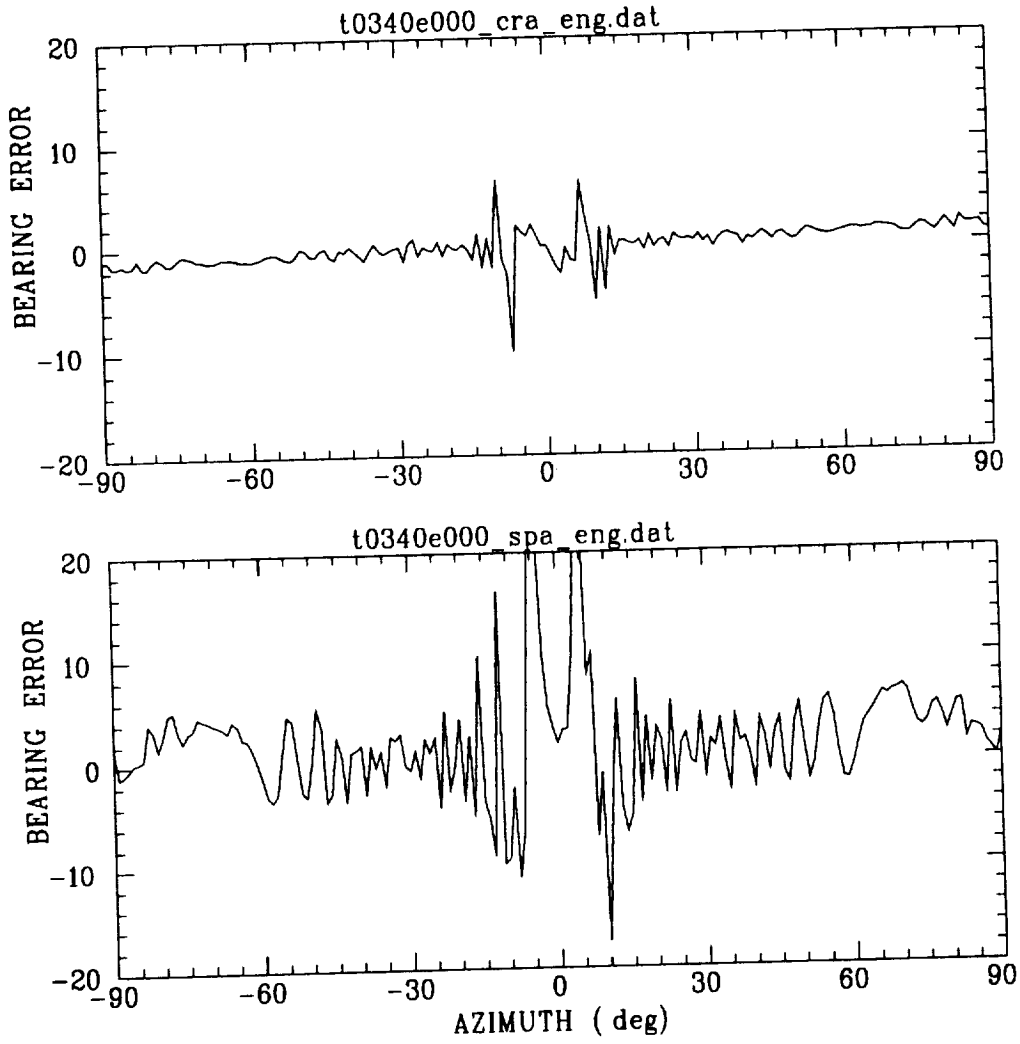

Figure 5.4: Error curves for CRA (top) and SPA (bottom) TCAS at 0° elevation. Top engine of Boeing 727-200 modeled by terminated circular waveguide.

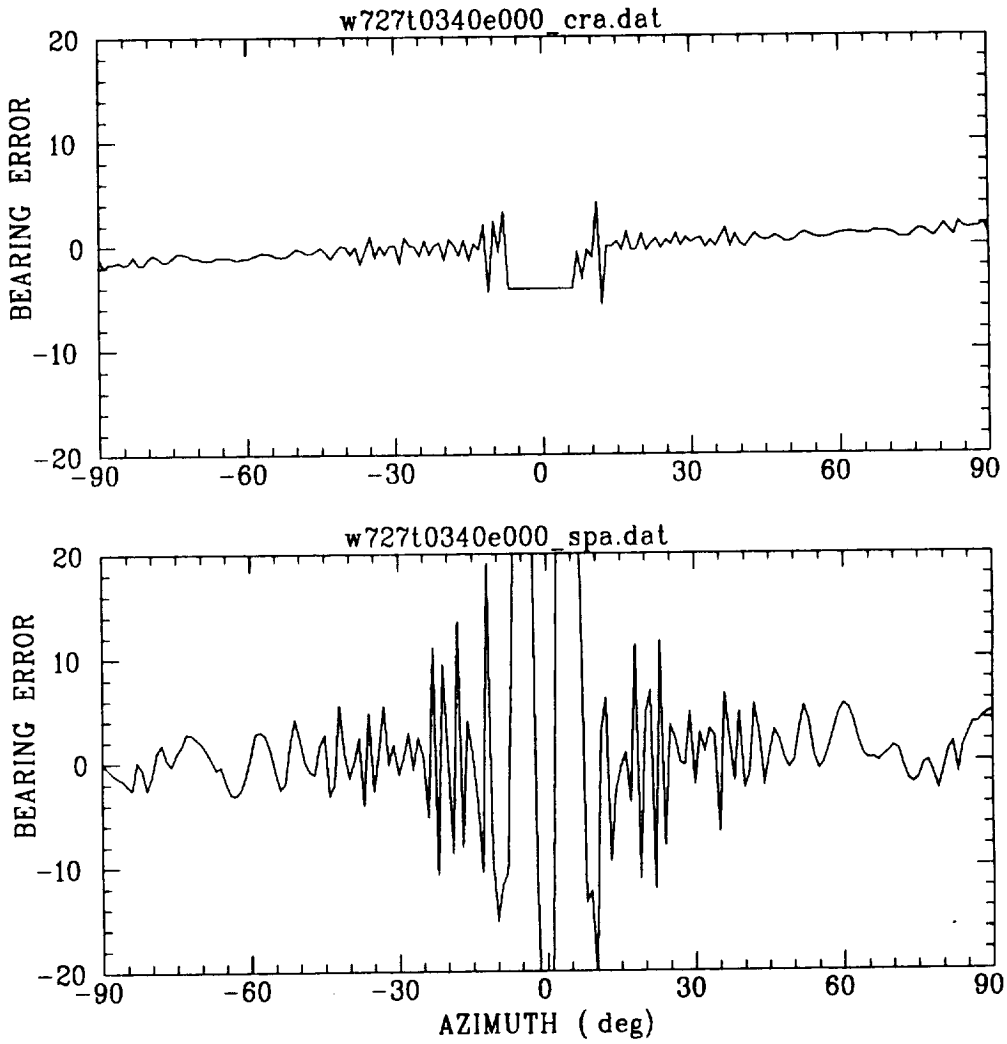

Figure 5.5: Error curves for CRA (top) and SPA (bottom) TCAS at 0° elevation. Top engine of Boeing 727-200 modeled by closed rectangular box.

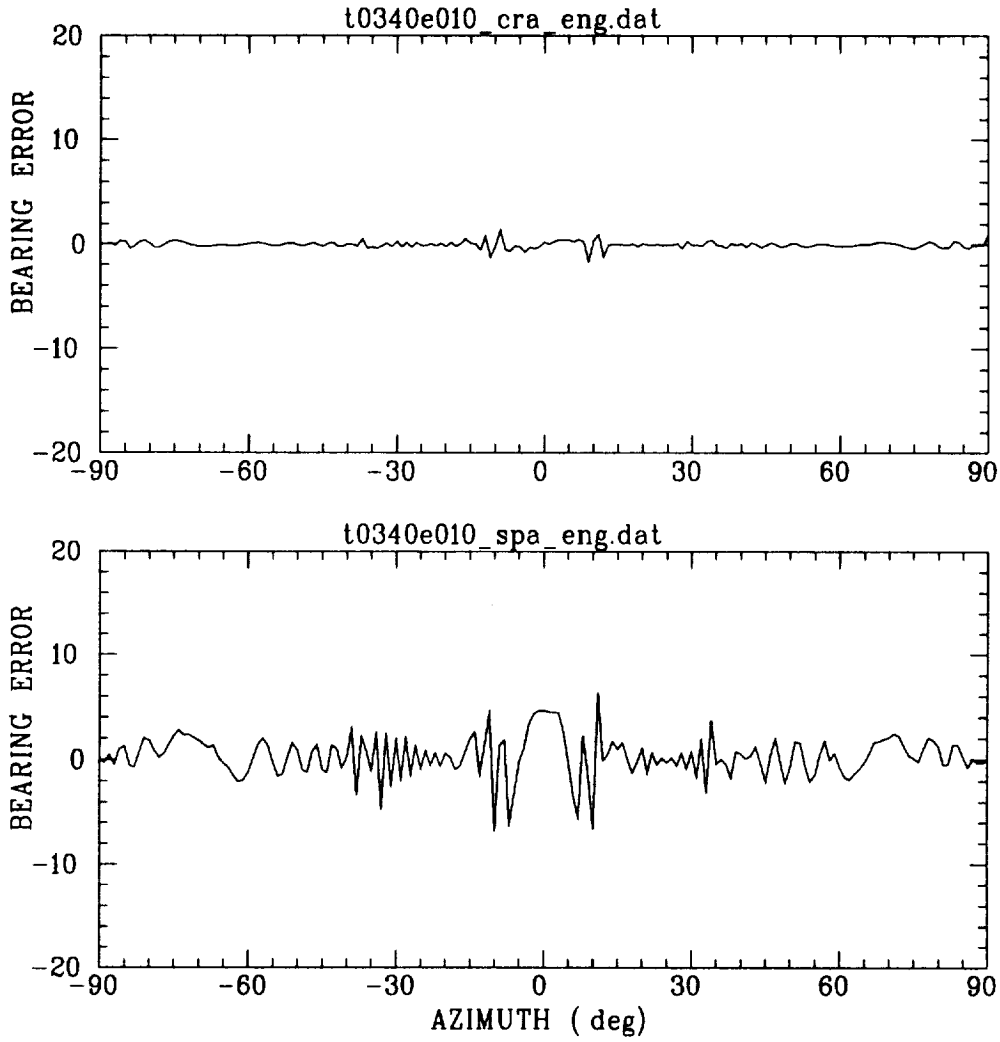

Figure 5.6: Error curves for CRA (top) and SPA (bottom) TCAS at 10° elevation. Top engine of Boeing 727-200 modeled by terminated circular waveguide.

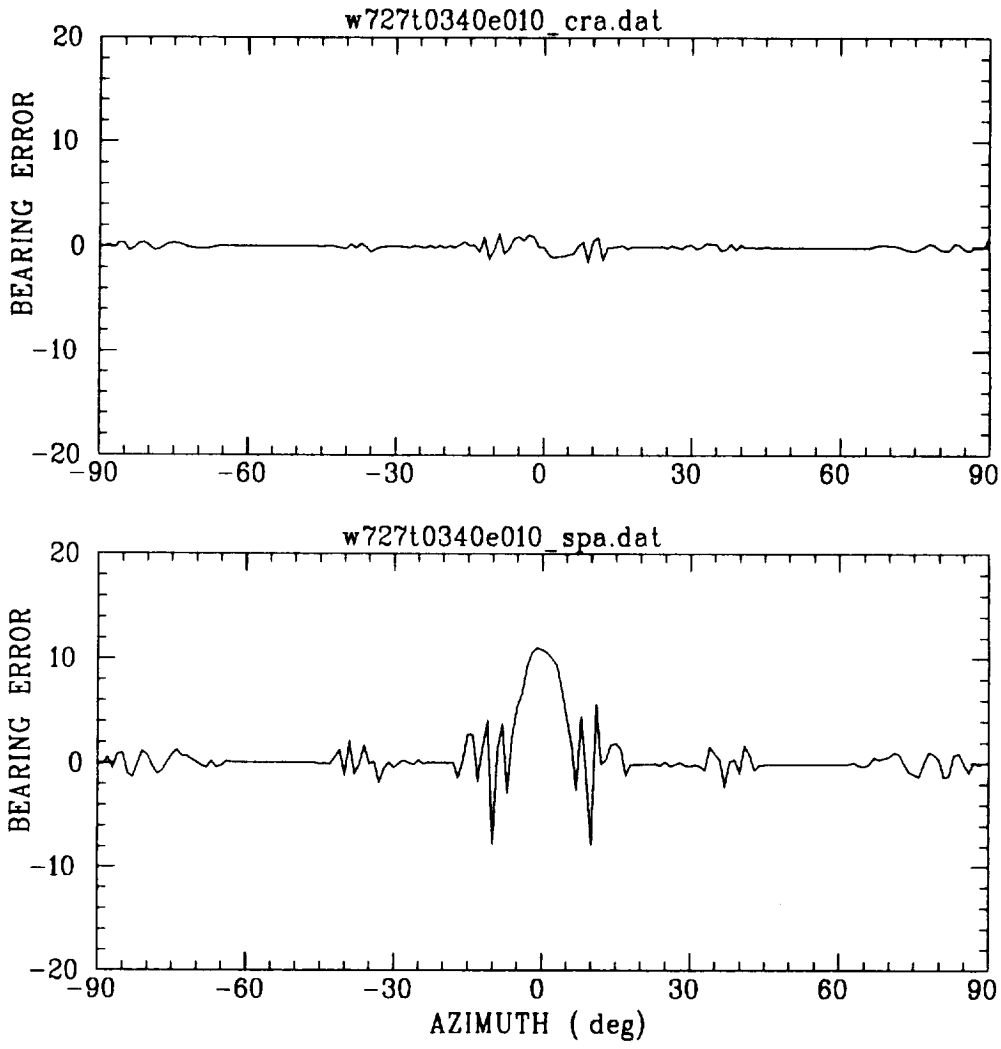

Figure 5.7: Error curves for CRA (top) and SPA (bottom) TCAS at 10° elevation. Top engine of Boeing 727-200 modeled by closed rectangular box.

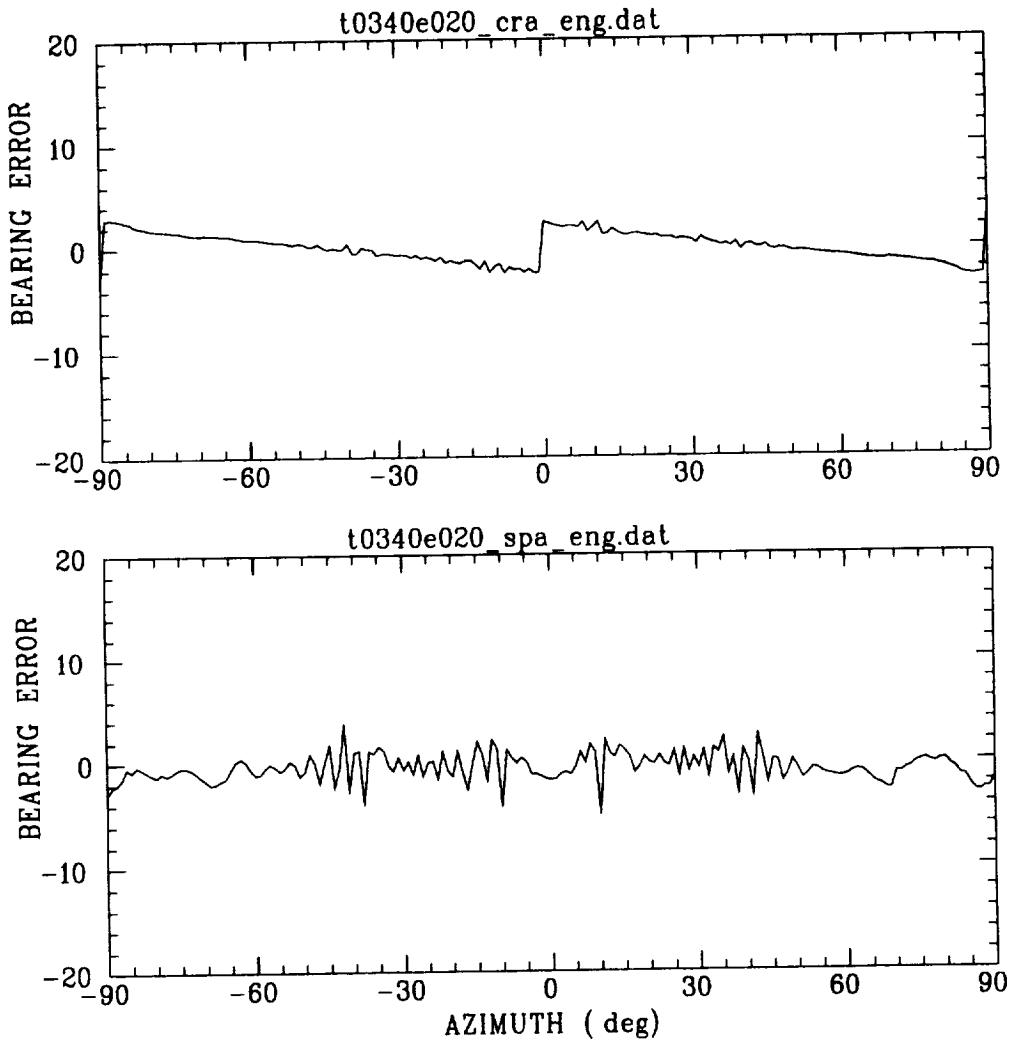

Figure 5.8: Error curves for CRA (top) and SPA (bottom) TCAS at 20° elevation. Top engine of Boeing 727-200 modeled by terminated circular waveguide.

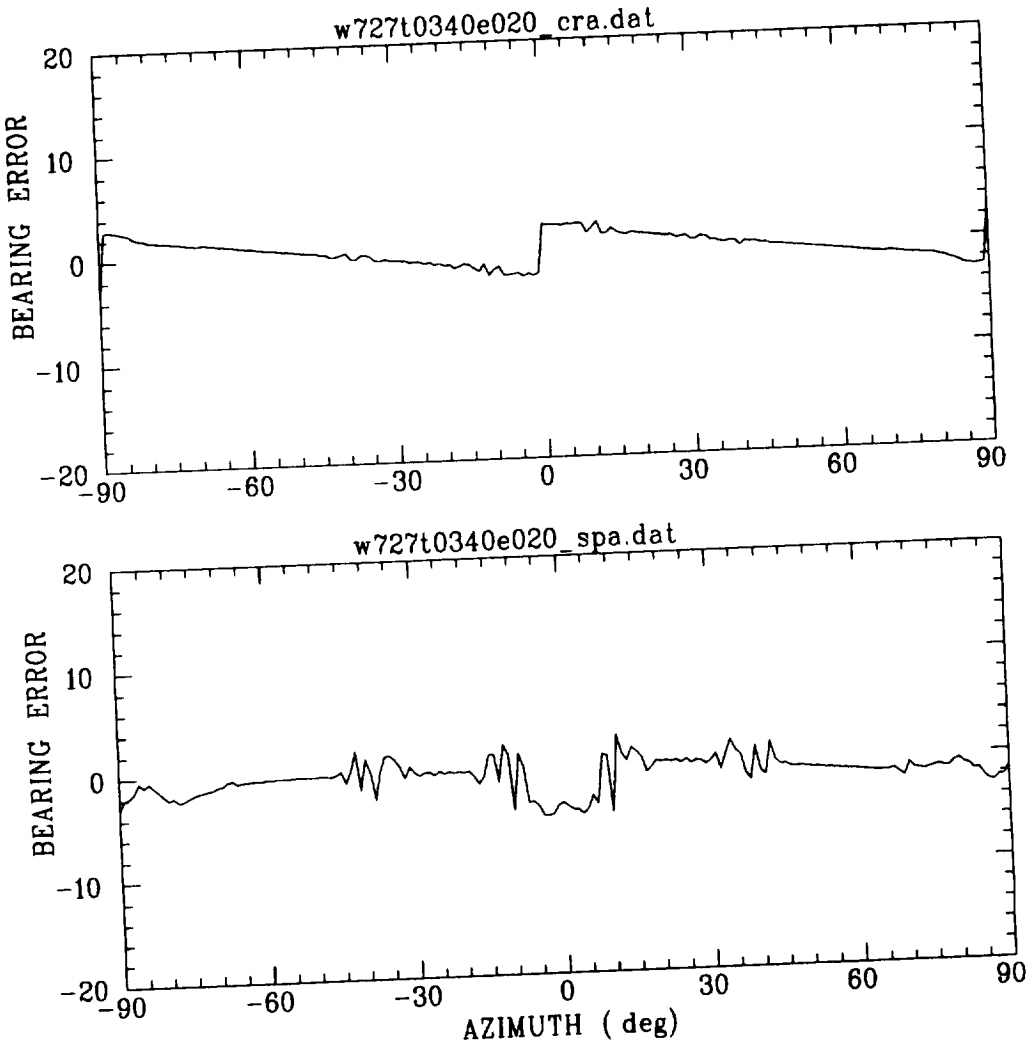

Figure 5.9: Error curves for CRA (top) and SPA (bottom) TCAS at 20° elevation. Top engine of Boeing 727-200 modeled by closed rectangular box.

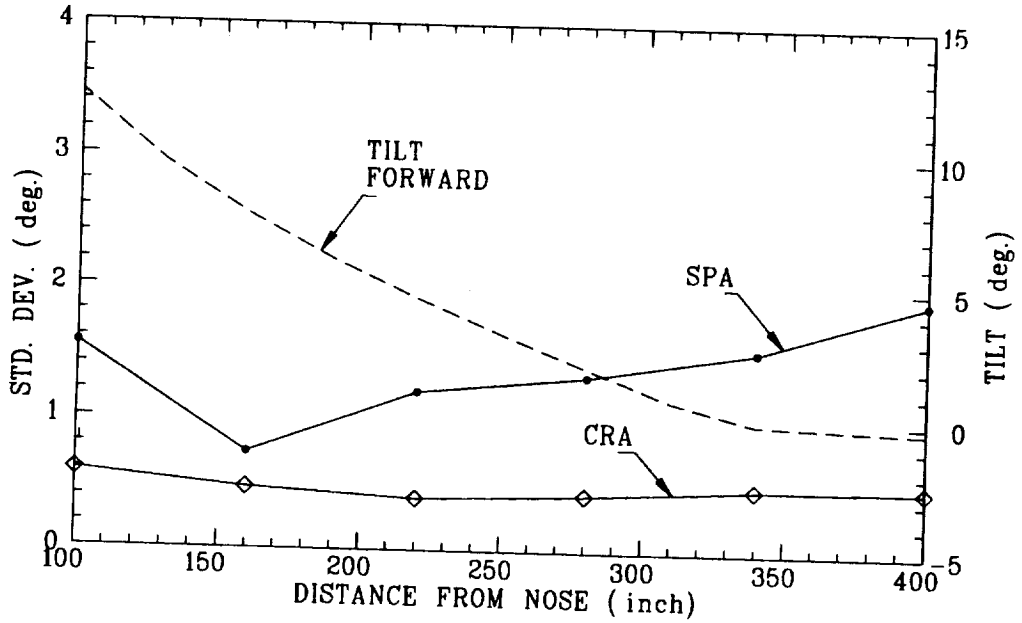

Figure 5.10: Standard deviation curves for Boeing 727-200, with top engine modeled by a terminated circular waveguide.

the error is practically the same for both cases of engine models for location 0100. This was found to be due to the placement of the TCAS. As one moves the TCAS forward, the top engine illumination gets blocked by the fuselage. Thus, the incident field at the inlet is smaller, because the creeping rays get rapidly attenuated by the fuselage. At location 0100, however, the attenuation is so great that the scattering from the inlet or the plate modeling the top engine is insignificant. Hence, it is concluded that the effect of the engine on the SPA TCAS can be overcome to a certain extent by moving the antenna forward.

Chapter 6

Conclusion

6.1 Introduction

The operation of CRA and SPA TCAS systems has been studied in terms of system performance based on electromagnetic effects. Each system has its own unique features, and shortcomings. In this chapter, these results are summarized. Possible methods of improving the performance are suggested to overcome some of these deficiencies. The error increases very close to the nose, due to the forward tilting of the TCAS antenna. The error also increases as one moves the antenna aft, i.e. towards the stabilizers.

It is interesting to find that the performance of both CRA and SPA systems is similar in the absence of nearby scatterers. The CRA however, performs much better in the vicinity of scatterers. Even in the absence of nearby scatterers, the standard deviation of the bearing error is consistently smaller for the CRA TCAS than the SPA system. A technique that could improve the performance of the CRA TCAS is suggested.

Lastly, the results obtained so far are extrapolated to a couple of other popular commercial airplanes, namely the MD-87 and the Boeing 757. It is expected that the TCAS would perform well if installed in the forward region of the fuselage based on the results generated in this report.

6.2 Elevation Effects

It is now well known that the performance of the TCAS system depends upon the elevation of the intruder. In all cases studied, the errors are smallest at 10°, which is the elevation at which the lookup table is created. The errors increase as the elevation changes. It was also seen in Chapter 2 that the CRA system exhibits discontinuities in the bearing error curves at elevations other than the one at which the lookup table was created. When the TCAS is in operation, the bearing of an intruder is continuously monitored and updated. Some of the signal processing involves the rate of change of the intruder's bearing. When the intruder passes from one quadrant to another, the jump in the detected bearing leads to discontinuities in the bearing rate signal. Unless this is detected and corrected immediately, the TCAS pilot would be given wrong information about the intruder. The spiral phase TCAS does not have these discontinuities in the bearing rate curve, because there is only one monotonic section of the lookup table, and the phase of the received signal always lies in the $[-180° : 180°]$ range.

The CRA system performance can be easily improved by using *elevation dependent lookup tables.* This presumes knowledge of the elevation of the intruder, which is available in the Mode-S transponder return. On the other hand, this entails more involved signal processing and storage requirements for (possibly) a large number of calibration curves, which should not be that big a problem for modern digital systems.

Lastly, it is noticed in general that the performance of the TCAS antenna gets worse as the intruder gets deeper into the shadow region of the TCAS (below the horizon, for a top mounted antenna) due to the blockage by the fuselage. The amount of error induced by the fuselage is fairly constant for the antenna in the mid-section of the fuselage, and gets smaller as the antenna is moved forward.

6.3 Nearby Antenna Effects

It was seen that the re-radiation from a nearby scatterer, such as another blade antenna, could affect the performance. Two typical blade antennas were considered, the AT741 and DMC60-1. Models based on the moment method were derived for these blade antennas. These models were then used along with the models for the TCAS antenna to study the performance of the TCAS system in the presence of these blades. It has also been demonstrated via moment method and UTD simulations that the blade antenna patterns are affected only slightly by the curvature of the fuselage. Based on these studies, it was found that the SPA system is severely affected by the blades. The CRA TCAS does not suffer from this problem to the same degree, due to its lobe switching technique. Consequently, it was established that the nearby antennas could be much closer to the CRA antenna than the SPA. It was also discovered that the nearby antenna need not be physically large to affect the bearing accuracy of the TCAS. The AT741 L-band blade, which is physically smaller than the DMC60-1 VHF antenna, illustrated this point.

Thus, for acceptable performance from the SPA antenna, one solution is to move it many wavelengths away from the scatterers. This would help two ways; firstly, due the increased separation, the re-radiation will be weaker from the other antenna. Secondly, the natural curvature of the fuselage would tend to block or attenuate the fields reaching the blade antenna.

The overall performance of both TCAS systems will be severely compromised by placing the TCAS aft of the blade antenna. The only solution in this case is to either switch the antenna positions (not always possible) or to increase the separation between the two antennas.

6.4 Engine Effects

In some of the cases studied, notably the bottom mounted antennas on the Boeing 737-300, and Boeing 747-200, it was found that for good performance of the TCAS antenna, it must be as far forward as practically possible. This is especially true for the SPA system, which has been proven to be more susceptible to scatterers around it. Since the SPA system does not discriminate as well as the CRA, it was found that it is much more difficult to find an acceptable performance location for the SPA than the CRA.

The engine plays a vital role in the performance of top mounted TCAS antenna in the case of the Boeing 727-200. It is once again seen that the SPA system is affected worse than the CRA TCAS. It was found that the adverse effect of the engine on the SPA system could be overcome to a certain extent by moving the antenna forward so that the fuselage curvature tends to block the engine illumination. It was also found that the CRA system performs much better in the presence of engines and other scatterers.

6.5 Other Factors

The treatment of the TCAS system has been solely from the viewpoint of the antenna designer. It is noted however, that this is last stage of the entire TCAS and and a fair amount of signal processing is necessary to acquire and track the other aircraft in the vicinity.

A factor that causes further deterioration of the performance occurs due to changes in the characteristics of the antenna, cables, etc., due to temperature and other variations. These changes affect both systems; however, it is suspected that the SPA system will be more sensitive to phase shifts and hence probably more difficult to calibrate and maintain.

The accuracy and stability of the phase comparison system may be enhanced by utilizing the amplitude information available at the antenna terminals. One could combine the antenna outputs with passive circuitry to yield sum and difference signals, and process these signals as a conventional amplitude system as suggested in [4].

6.6 Concluding Remarks

It has been seen that all these studies generally point to locating the TCAS antenna towards the forward region of the fuselage. For the top mounted antenna, it is best to locate the antenna where the fuselage is curving down so that good coverage can be obtained for lower elevation angles and lessen the effects of the top-mounted engines, blade antennas and/or vertical stabilizer. For the bottom mounted antenna however, it is best to locate it on a flat section, because full azimuthal coverage is desirable. Care must be exercised to mount the antenna away from engines and other scatterers.

Finally, based on these findings, some remarks can be made about other aircraft. These are listed below:

6.6.1 McDonnell Douglas MD-87

The McDonnell Douglas MD-80 series airplanes, developed from the DC-9 are popular as a short/medium range commercial transport. Other aircraft in the series are similar, except for the fuselage length. The most recent addition to this family is the MD-90 airplane, which is very similar to the MD-87. The MD-87 airplane is powered by two JT8D series turbofan engines, on either side of the fuselage, near the tail of the aircraft [28]. A side view of the MD-87 aircraft is shown in Figure 6.1.

This aircraft would probably be the easiest to place the TCAS antennas on. The placement of its engines, between the top and bottom of the fuselage, is in shadow of both the top and bottom mounted antennas. Hence, good performance of the

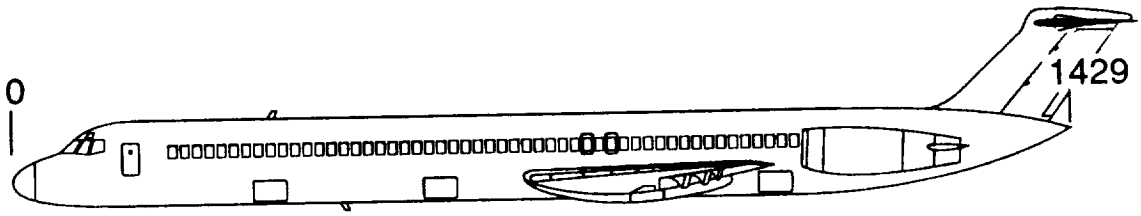

Figure 6.1: A scaled sketch of the McDonnell Douglas MD-87 aircraft. Fuselage length is shown marked in inches.

TCAS system may be expected for an antenna placed in the forward region, for both top and bottom mounted cases. It is noticed that the wings are slightly above the bottom of the fuselage towards the rear of the aircraft and are not expected to deteriorate the performance very much.

6.6.2 Boeing 757-200

The Boeing 757 series of aircraft is similar to the Boeing 737, in that its two engines are placed under the wings. The Boeing 757-200 is a short/medium range transport aircraft, 1858″ long as shown in Figure 6.2. Note that the fuselage of the Boeing 737-300 is only 1163″ long; whereas, the Boeing 747-200 is 2792″ long [28].

Due to the increased space available on the top of the fuselage, and placement of the VHF blade antenna towards the middle of the aircraft, it is expected that the location of antenna for the TCAS system would pose fewer problems than the Boeing 737. The bottom antenna on the other hand is restricted by the engine inlets and probably should be placed far forward for looking in the nose region.

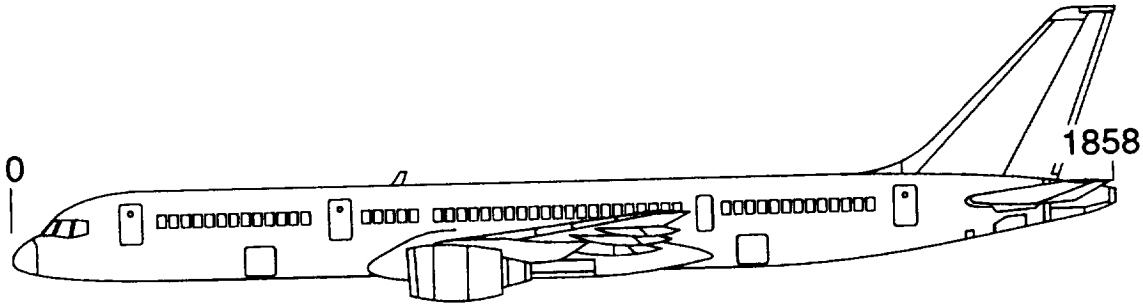

Figure 6.2: A scaled sketch of the Boeing 757-200 aircraft. Fuselage length is shown marked in inches.

Bibliography

[1] M. T. Pozesky and M. K. Mann, "The US Air Traffic Control System Architecture," *Proc. IEEE*, vol. 77, pp. 1605–1617, November 1989. Special Issue on Air Traffic Control.

[2] T. S. Perry, "Improving the Worlds's Largest Most Advanced System," *IEEE Spectrum*, vol. 28, pp. 22–36, February 1991. Special Report: Air Traffic Control.

[3] R. K. Jurgen, "Antenna Ups Bearing Accuracy in TCASII," *IEEE Spectrum*, vol. 27, p. 11, April 1990. News Item in 'Innovations' Column.

[4] M. I. Skolnik, *Radar Handbook*. New York: McGraw-Hill Book Company, Inc., 1970.

[5] R. G. Rojas, Y. C. Chen, and W. D. Burnside, "Improved Computer Simulation of the TCAS III Circular Array Mounted on an Aircraft," Technical Report 716199-12, The Ohio State University ElectroScience Laboratory, April 1989.

[6] J. E. Reed, "Enhanced TCAS II Antenna Characteristics Report," Report BCD-TR-090, Allied Bendix Aerospace — Bendix Communications Division, October 1983.

[7] J. E. Reed, "Enhanced TCAS II System Summary (A 3D Traffic Alert & Collision Avoidance System)," Report BCD-TR-098, Allied Bendix Aerospace — Bendix Communications Division, April 1984.

[8] A. I. Sinsky, J. E. Reed, and J. Fee, "Enhanced TCAS II Tracking Accuracy," in *AIAA/IEEE Digital Avionics Systems Conference*, December 1984. Paper 84-2738-cp.

[9] K. J. Kunachowicz, "Model Testing of Airborne VHF Direction Finding Antenna System," in *Antennas for Aircraft and Spacecraft*, pp. 223–227, IEE Conference Publication, no. 128, 1975.

[10] R. G. Kouyoumjian and P. H. Pathak, "A Uniform Geometrical Theory of Diffraction for an Edge in a Perfectly Conducting Surface," *Proc. IEEE*, vol. 62, pp. 1448–1461, November 1974.

[11] J. J. Kim and W. D. Burnside, "Simulation and Analysis of Antennas Radiating in a Complex Environment," *IEEE Trans. Antennas and Propagat.*, vol. AP-34, pp. 554–562, April 1986.

[12] W. D. Burnside, J. J. Kim, B. Grandchamp, R. G. Rojas, and P. Law, "Airborne Antenna Radiation Pattern Code User's Manual," Technical Report 716199-4, The Ohio State University ElectroScience Laboratory, September 1985.

[13] K. S. Sampath, R. G. Rojas, and W. D. Burnside, "Modelling and Performance Analysis of Four and Eight Element TCAS," Technical Report 716199-15, The Ohio State University ElectroScience Laboratory, April 1990.

[14] R. G. Rojas, K. S. Sampath, and W. D. Burnside, "Analysis and Simulation of Collision Avoidance TCAS Antennas mounted on Aircraft," *Applied Computational Electromagnetics Society Journal*, vol. 6, pp. 112–139, Summer 1991.

[15] R. G. Rojas and K. S. Sampath, "Analysis of Airframe Effects on the Performance of TCAS Antennas," Technical Report 724737-1, The Ohio State University ElectroScience Laboratory, August 1992.

[16] R. F. Harrington, *Time Harmonic Electromagnetic Fields.* New York: McGraw-Hill Electrical Engineering Series, 1961.

[17] E. H. Newman, "A User's Manual for the Electromagnetic Surface Patch Code: ESP, Version IV," Technical Report 716199-11, The Ohio State University ElectroScience Laboratory, August 1988.

[18] A. Altintas, *Electromagnetic Scattering from a Class of Open-Ended Waveguide Discontinuities.* Ph.D. dissertation, The Ohio State University, Dept. Elec. Eng., Columbus, OH, March 1986.

[19] P. H. Pathak, A. Altintas, C. W. Chuang, and S. Barkeshli, "Near Field Scattering by Rectangular and Circular Inlet Configurations with an Impedance Surface Termination," Technical Report 715267-1, The Ohio State University ElectroScience Laboratory, July 1984.

[20] P. H. Pathak, C. W. Chuang, and M. C. Liang, "Inlet Modeling Studies," Technical Report 717674-1, The Ohio State University ElectroScience Laboratory, October 1986.

[21] C. A. Balanis, *Antenna Theory: Analysis and Design.* New York: Harper & Row Electrical Engineering Series, 1982.

[22] S. Silver, *Microwave Antenna Theory and Design*, vol. 12 of *Radiation Laboratory Series.* New York: McGraw Hill Book Company, Inc., 1949.

[23] E. K. Sandeman, "Spiral Phase Fields—Possible Applications," *Wireless Engineer*, pp. 96–105, March 1949.

[24] E. W. Braeden, F. T. Klevenow, E. H. Newman, R. G. Rojas, K. S. Sampath, J. T. Scheik, and H. T. Shamansky, "Operation of the Helicopter Antenna Radiation Prediction Code," Technical Report, The Ohio State University ElectroScience Laboratory, 1993. To be published.

[25] P. H. Pathak and N. Wang, "Ray Analysis of Mutual Coupling Between Antennas on a Convex Surface," *IEEE Trans. Antennas and Propagat.*, vol. AP-29, pp. 911–922, November 1981.

[26] D. W. Burgess. MIT Lincoln Laboratory, 1991. Personal Communication.

[27] L. W. Johnson and R. D. Riess, *Introduction to Linear Algebra.* Reading, MA: Addison-Wesley Series in Mathematics, 1981.

[28] J. W. R. Tailor, ed., *Jane's All the World's Aircraft.* New York: Jane's Publishing Inc., 1988.

[29] M. E. Peters and E. H. Newman, "A User's Manual for the Method of Moments Aircraft Modeling Code," Technical Report 716199-14, The Ohio State University ElectroScience Laboratory, September 1989.

[30] J. Van Bladel, *Electromagnetic Fields.* New York: McGraw-Hill Electrical Engineering Series, 1966.

[31] R. E. Collin, *Foundations for Microwave Engineering.* New York: McGraw-Hill Electrical Engineering Series, 1966.

[32] P. H. Pathak and R. J. Burkholder, "Modal, Ray and Beam Techniques for Analyzing the EM Scattering by Open-Ended Waveguide Cavities," *IEEE Trans. Antennas and Propagat.*, vol. AP-37, pp. 636–647, May 1989.

Appendix A

Statistics of TCAS Antennas

In this appendix, some relevant statistics for the various aircraft are provided. These tables provide the location code used in the simulation for future reference. This is usually the distance of the antenna from the nose in the UTD model used for the aircraft code. The second column is the distance of the TCAS antenna on the actual aircraft. Third column gives the angle the antenna normal makes with the forward horizontal direction, at the location of the TCAS antenna. The next three columns are the output of processing all the data from the aircraft code and they give the maximum, average, and the standard deviation of the absolute value of the error for each location.

Table A.1: Statistics for top mounted CRA TCAS: Boeing 737-300.

Location Code	Distance From Nose	Theta Normal	Maximum |Error|	Absolute Average	Standard Deviation
0120	169.0000	99.2480	2.4980	1.1879	0.4191
0150	199.0000	97.1515	2.2110	0.9646	0.3438
0180	229.0000	95.3608	2.0571	0.8627	0.3491
0210	259.0000	93.7611	1.6377	0.7999	0.2363
0240	289.0000	92.2793	1.3883	0.7899	0.2311
0270	319.0000	90.8634	1.5407	0.8293	0.2720
0300	349.0000	89.9599	1.6729	0.9009	0.2809
0330	379.0000	89.8543	1.7210	0.9336	0.2654
0360	409.0000	89.7483	1.6968	0.9521	0.2577
0390	439.0000	89.6418	1.7127	0.9849	0.2578
0420	469.0000	89.5345	1.7925	0.9870	0.2625
0450	499.0000	89.4262	1.8011	1.0182	0.2659
0480	529.0000	89.3167	1.9183	1.0296	0.2629

Table A.2: Statistics for top mounted SPA TCAS: Boeing 737-300.

Location Code	Distance From Nose	Theta Normal	Maximum |Error|	Absolute Average	Standard Deviation
0120	169.0000	99.2469	3.3511	1.3753	0.7325
0150	199.0000	97.1508	2.9690	1.2441	0.5995
0180	229.0000	95.3603	2.5731	1.1413	0.5163
0210	259.0000	93.7608	2.3611	1.0144	0.5437
0240	289.0000	92.2791	2.2978	0.9988	0.5347
0270	319.0000	90.8633	2.4378	1.0313	0.5538
0300	349.0000	89.9599	2.4480	1.1330	0.5811
0330	379.0000	89.8543	2.6821	1.1293	0.5752
0360	409.0000	89.7483	2.6012	1.1599	0.5918
0390	439.0000	89.6418	2.4741	1.1542	0.5906
0420	469.0000	89.5346	2.4361	1.1825	0.5844
0450	499.0000	89.4263	2.6128	1.1964	0.5759
0480	529.0000	89.3167	2.3412	1.2175	0.5598

Table A.3: Statistics for bottom mounted CRA TCAS: Boeing 737-300. The model for aft mounted antenna used for locations greater than 645″ from nose.

Location Code	Distance From Nose	Theta Normal	Maximum |Error|	Absolute Average	Standard Deviation
0046	95.0000	102.1612	20.6132	2.6537	1.6585
0106	155.0000	95.9989	18.8678	2.2422	1.9440
0136	185.0000	93.6377	37.4938	2.0531	2.4643
0166	215.0000	91.4692	17.5247	2.0979	2.0902
0196	245.0000	89.9799	17.0278	2.4506	2.3047
0226	275.0000	89.9127	24.4318	2.8565	3.2220
0256	305.0000	89.8453	22.3935	3.0850	3.3810
0286	335.0000	89.7777	28.9407	3.3745	4.1844
0316	365.0000	89.7098	24.3487	3.3209	4.0494
0346	395.0000	89.6414	32.2942	4.3415	6.2711
0376	425.0000	89.5724	30.1544	3.6141	5.2096
0406	455.0000	89.5027	29.3484	3.5755	4.6831
0441	490.0000	89.4202	24.9285	3.8472	4.4048
0466	515.0000	89.3606	31.9606	3.9398	5.9372
0556	605.0000	89.1386	41.5618	4.4798	6.3547
0321	645.0000	88.6294	27.5043	4.5429	6.2296
0381	705.0000	87.8999	30.8443	3.7551	5.9535
0441	765.0000	87.1022	20.6750	2.9689	4.2512
0501	825.0000	86.1958	23.1261	2.6340	3.6603
0561	885.0000	85.1138	20.5303	2.3502	2.6607
0621	945.0000	83.7318	31.8529	2.5823	4.4394

Table A.4: Statistics for bottom mounted SPA TCAS: Boeing 737-300. The model for aft mounted antenna used for locations greater than 645″ from nose.

Location Code	Distance From Nose	Theta Normal	Maximum |Error|	Absolute Average	Standard Deviation
0046	95.0000	102.1582	30.8373	3.8794	3.4399
0106	155.0000	95.9978	34.4278	3.7863	4.3934
0136	185.0000	93.6372	40.0473	3.6513	4.5670
0166	215.0000	91.4689	40.3006	3.9780	4.4966
0196	245.0000	89.9799	39.1592	4.3582	4.7137
0226	275.0000	89.9127	45.3880	4.8528	5.2688
0256	305.0000	89.8453	47.7038	5.7377	6.7111
0286	335.0000	89.7778	55.7487	6.2868	7.8076
0316	365.0000	89.7098	61.4151	7.3627	9.5852
0346	395.0000	89.6414	53.1614	8.5782	11.1961
0376	425.0000	89.5724	61.8417	9.4100	11.7726
0406	455.0000	89.5027	57.1034	10.0566	12.2142
0436	485.0000	89.4322	53.5945	10.2609	12.4516
0466	515.0000	89.3606	52.8546	9.5808	11.4672
0556	605.0000	89.1387	74.3590	8.0684	10.2340
0381	705.0000	87.9001	48.1701	5.9154	8.3961
0441	765.0000	87.1025	39.6457	5.1586	7.2997
0501	825.0000	86.1961	60.4006	4.5379	7.3458
0561	885.0000	85.1143	37.2314	3.7076	5.4990
0621	945.0000	83.7326	37.6421	3.3194	4.6561

Table A.5: Statistics for top mounted CRA TCAS: Boeing 747-200. Stations 1380 and 1440 lie aft of the cupola.

Location Code	Station Number	Theta Normal	Maximum |Error|	Absolute Average	Standard Deviation
0270	270.0000	115.5353	7.3619	4.8343	1.0551
0300	300.0000	107.4228	4.1563	2.8565	0.5684
0330	330.0000	101.8281	2.6717	1.7810	0.4083
0360	360.0000	96.1295	1.7323	0.8561	0.3383
0390	390.0000	91.7944	1.1224	0.4508	0.2671
0420	420.0000	93.0957	1.2683	0.5083	0.2936
0450	450.0000	92.2849	1.2555	0.4675	0.2831
0480	480.0000	90.5367	1.0390	0.4380	0.2347
0510	510.0000	89.6165	1.2578	0.4908	0.2370
0540	540.0000	89.3417	1.2732	0.5121	0.2275
0570	570.0000	86.7256	1.6685	0.7823	0.3263
0600	600.0000	85.7099	1.8806	0.9030	0.3309
0630	630.0000	84.2348	1.8233	1.0237	0.2963
0660	660.0000	83.6920	2.0761	1.1187	0.3112
0690	690.0000	82.6091	2.0706	1.3080	0.3264
0720	720.0000	82.0216	2.0176	1.3942	0.2979
0750	750.0000	80.5222	2.5456	1.6350	0.3695
0810	810.0000	78.7237	2.6632	1.9270	0.3219
1380	1380.0000	90.5189	8.7265	1.0336	1.3710
1440	1440.0000	90.5575	7.3996	0.9982	1.1837

Table A.6: Statistics for top mounted SPA TCAS: Boeing 747-200. Stations 1380 and 1440 lie aft of the cupola.

Location Code	Station Number	Theta Normal	Maximum |Error|	Absolute Average	Standard Deviation
0270	270.0000	115.5353	5.4403	4.0316	1.2404
0300	300.0000	107.4228	3.7187	2.4174	0.8712
0330	330.0000	101.8281	2.8663	1.5443	0.6506
0360	360.0000	96.1295	2.1297	0.8624	0.4671
0390	390.0000	91.7944	1.9998	0.6201	0.4309
0420	420.0000	93.0957	2.1131	0.6440	0.4604
0450	450.0000	92.2849	1.9889	0.6328	0.4547
0480	480.0000	90.5367	1.7400	0.5881	0.4214
0510	510.0000	89.6165	1.8281	0.7403	0.3830
0540	540.0000	89.3417	1.8827	0.6224	0.3729
0570	570.0000	86.7256	2.1105	0.8498	0.3984
0600	600.0000	85.7099	2.0913	0.9906	0.4379
0630	630.0000	84.2348	2.5281	1.0946	0.3755
0660	660.0000	83.6920	2.4717	1.2531	0.4140
0690	690.0000	82.6091	2.3826	1.4119	0.3658
0750	750.0000	80.5222	2.9295	1.7092	0.3737
0810	810.0000	78.7237	3.0454	1.9732	0.3745
1380	1380.0000	90.5189	32.8940	3.3374	5.3732
1440	1440.0000	90.5575	37.0278	3.5694	5.3195

Table A.7: Statistics for bottom mounted CRA TCAS: Boeing 747-200.

Location Code	Station Number	Theta Normal	Maximum |Error|	Absolute Average	Standard Deviation
0170	170.0000	112.4038	31.0171	4.8203	3.1640
0200	200.0000	108.0461	22.0036	3.8405	2.3237
0230	230.0000	103.7831	19.5476	3.1210	2.4771
0260	260.0000	100.6243	17.8396	2.3556	1.8371
0290	290.0000	99.0747	18.7528	2.5253	2.6292
0320	320.0000	98.0066	11.7499	2.0940	1.7301
0350	350.0000	97.1260	18.3055	1.9955	2.2995
0380	380.0000	96.4559	18.4471	1.9474	2.1145
0410	410.0000	95.9381	20.2134	2.2221	2.9699
0440	440.0000	95.5523	23.1327	2.1376	2.8784
0470	470.0000	95.2549	14.2177	1.9531	2.1094
0500	500.0000	95.0356	19.5529	2.1708	2.9524
0530	530.0000	94.8662	23.0913	2.0412	3.0873
0560	560.0000	94.6189	24.3195	2.0245	3.4849
0590	590.0000	94.5140	27.0265	2.2386	3.8630
0620	620.0000	94.2928	17.1046	1.8590	2.0605
0650	650.0000	94.1702	24.2844	2.0502	3.3240
0680	680.0000	93.9038	24.6918	2.4173	4.3770
0710	710.0000	93.6169	25.5776	2.3023	4.1770
0800	800.0000	92.5765	29.4408	2.6359	5.2018
0890	890.0000	91.6126	31.6827	2.6496	4.9040
0980	980.0000	90.8671	24.1719	1.9948	3.3114
1070	1070.0000	90.4037	27.6843	1.7368	3.3079
1160	1160.0000	89.9385	30.3365	1.7019	3.3601

Table A.8: Statistics for bottom mounted SPA TCAS: Boeing 747-200.

Location Code	Station Number	Theta Normal	Maximum |Error|	Absolute Average	Standard Deviation
0170	170.0000	112.4038	28.8542	4.7222	3.4279
0200	200.0000	108.0461	38.9429	4.1454	3.6746
0230	230.0000	103.7831	37.2420	3.5994	3.9984
0260	260.0000	100.6243	30.1497	3.1487	3.9460
0290	290.0000	99.0747	26.2923	3.0423	3.5636
0320	320.0000	98.0066	31.9184	2.6144	3.1870
0350	350.0000	97.1260	21.6287	2.6256	3.5423
0380	380.0000	96.4559	37.3500	2.9808	4.7845
0410	410.0000	95.9381	29.5302	2.9839	4.3333
0440	440.0000	95.5523	32.1880	2.8229	4.3041
0470	470.0000	95.2549	32.2645	2.9104	4.3667
0500	500.0000	95.0356	35.6382	2.8998	4.0981
0530	530.0000	94.8662	46.7629	2.8092	4.8430
0560	560.0000	94.6189	42.7559	3.2123	6.0199
0590	590.0000	94.5140	48.3350	3.9122	7.6843
0620	620.0000	94.2928	45.4221	3.4294	6.5876
0650	650.0000	94.1702	50.0999	3.3702	6.4994
0680	680.0000	93.9038	52.8423	3.2489	6.2358
0710	710.0000	93.6169	47.5850	3.3366	6.1165
0800	800.0000	92.5765	44.9433	3.8839	7.5809
0890	890.0000	91.6126	50.5754	4.3110	7.5467
0980	980.0000	90.8671	44.6187	4.4109	7.1810
1070	1070.0000	90.4037	35.8714	4.6880	7.4140
1160	1160.0000	89.9385	45.9116	4.7909	8.0948

Table A.9: Statistics for top mounted CRA TCAS: Boeing 727-200.

Location Code	Distance From Nose	Theta Normal	Maximum |Error|	Absolute Average	Standard Deviation
0100	100.0000	102.3022	3.9868	1.5764	0.5341
0140	140.0000	98.9772	2.4316	1.1656	0.4360
0180	180.0000	96.5303	2.4374	0.8667	0.5235
0200	200.0000	95.4916	2.3658	0.9394	0.4318
0220	220.0000	94.5344	2.1595	0.8669	0.4356
0260	260.0000	92.7874	2.9008	0.9677	0.4569
0300	300.0000	91.1730	3.6957	1.0707	0.6966
0320	320.0000	90.3896	3.9930	1.0916	0.6490
0340	340.0000	89.9625	3.7680	1.2352	0.7462
0380	380.0000	89.8125	4.0563	1.4472	0.7959
0420	420.0000	89.6616	4.7993	1.4166	0.8804
0460	460.0000	89.5094	4.9945	1.4267	0.9297
0500	500.0000	89.3549	5.5235	1.5664	1.0979
0540	540.0000	89.1976	6.5893	1.6835	1.2862
0580	580.0000	89.0366	7.0991	1.9211	1.4842

Table A.10: Statistics for top mounted SPA TCAS: Boeing 727-200.

Location Code	Distance From Nose	Theta Normal	Maximum |Error|	Absolute Average	Standard Deviation
0100	100.0000	102.3002	15.0834	2.1480	1.2350
0140	140.0000	98.9761	6.7901	1.8592	1.0037
0180	180.0000	96.5298	8.3212	1.9102	1.3128
0200	200.0000	95.4911	8.9065	2.0151	1.7084
0220	220.0000	94.5340	12.1936	2.2136	2.2104
0260	260.0000	92.7872	14.0352	2.5460	2.8560
0300	300.0000	91.1729	15.4140	3.0154	3.5035
0320	320.0000	90.3896	20.7349	3.6282	4.5359
0340	340.0000	89.9625	17.5436	4.3637	4.2194
0380	380.0000	89.8125	20.8014	4.0296	4.8206
0420	420.0000	89.6617	24.6850	4.6279	6.0154
0460	460.0000	89.5094	22.0273	4.7512	5.5725
0500	500.0000	89.3549	23.6262	4.8537	5.6560
0540	540.0000	89.1976	32.5785	6.1714	7.6192
0580	580.0000	89.0367	41.5553	7.3432	9.4367

Table A.11: Statistics for bottom mounted CRA TCAS: Boeing 727-200.

Location Code	Distance From Nose	Theta Normal	Maximum |Error|	Absolute Average	Standard Deviation
0100	100.0000	100.0279	45.0644	2.9680	5.6467
0140	140.0000	97.2995	40.0294	2.7964	6.2837
0180	180.0000	95.3030	58.3248	3.0624	7.9488
0220	220.0000	93.6793	24.8572	1.2885	1.7567
0240	240.0000	92.9514	8.0948	1.1278	1.0205
0260	260.0000	92.2608	14.8468	1.0957	1.1760
0300	300.0000	90.9512	9.0197	1.0902	1.1176
0340	340.0000	89.9696	24.4167	1.2039	1.9215
0360	360.0000	89.9088	12.6119	1.1121	1.2853
0380	380.0000	89.8480	30.9790	1.6472	3.4001
0420	420.0000	89.7257	33.1766	2.7763	5.7794
0460	460.0000	89.6022	69.0273	3.2817	8.0215
0480	480.0000	89.5398	90.8555	7.4584	14.3458

Table A.12: Statistics for bottom mounted SPA TCAS: Boeing 727-200.

Location Code	Distance From Nose	Theta Normal	Maximum |Error|	Absolute Average	Standard Deviation
0100	100.0000	100.0260	34.9310	2.8616	3.8932
0140	140.0000	97.2985	24.9701	2.6363	3.9149
0180	180.0000	95.3024	39.3768	2.7321	4.8413
0220	220.0000	93.6789	31.0480	1.8654	2.3767
0240	240.0000	92.9511	26.1150	1.3524	2.2934
0260	260.0000	92.2605	33.9125	1.8206	2.5723
0300	300.0000	90.9511	31.9772	1.6031	1.7913
0340	340.0000	89.9696	37.6930	2.4063	3.0135
0360	360.0000	89.9088	32.4067	1.4347	3.0853
0380	380.0000	89.8480	28.1335	2.0772	2.7737
0420	420.0000	89.7257	55.0527	3.1774	6.1373
0460	460.0000	89.6022	68.5810	3.8541	7.1191
0480	480.0000	89.5398	70.0208	6.6051	12.6037

Appendix B

Helicopter Antenna Radiation Prediction (HARP)

B.1 Introduction

The Helicopter Antenna Radiation Prediction (HARP) is the name given to a computer code developed at the Ohio State University ElectroScience Laboratory [24]. It integrates the techniques of modern computer graphics with two electromagnetic far zone scattering and radiation analysis programs. The result is an easy to use, versatile, package to graphically complement and help visualize the mathematical models and patterns at various stages of the program.

Two widely used computational techniques of electromagnetic analysis are the method of moments (MM) and the uniform geometrical theory of diffraction (UTD). MM is a low frequency method, used when the objects are not electrically large. For the sources radiating in the vicinity of electrically large bodies, UTD is more appropriate. For a given problem, hence, the method chosen depends upon the size of the body as well as available computational resources.

HARP is an X windows based graphical user interface (GUI) that enables a user to build a model of an aircraft from the blue prints of the cross sections of the body along its length. The user can then predict the electromagnetic radiation patterns of specified antennas on the airplane or helicopter. Though HARP was developed

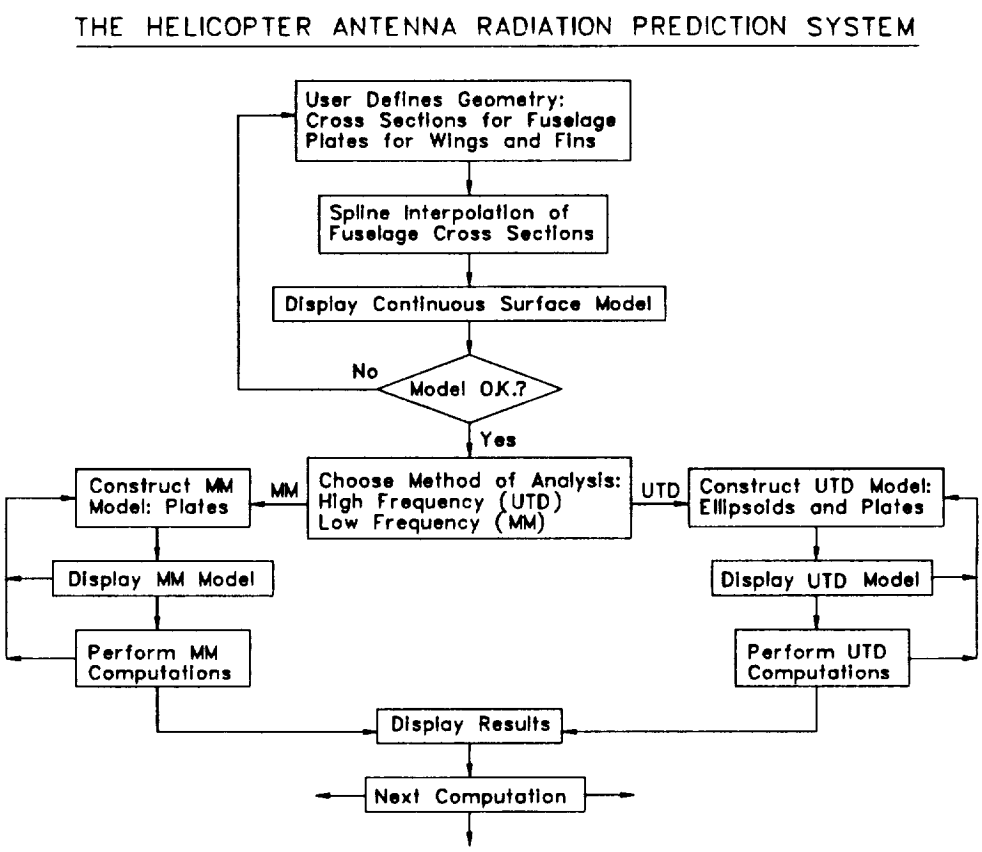

Figure B.1: Block diagram of the major components of HARP.

primarily for modeling helicopters, the modeling methods are very general and hence applicable to many varieties of bodies, of essentially arbitrary shape, like airplanes, missiles etc.

B.2 Overview

Figure B.1 depicts a block diagram of HARP. The major functions are denoted by their own blocks. Most of the modeling involves the entry and editing of the body data until a satisfactory body is built. Note that the only electromagnetics codes are blocks, labeled *Perform MM Computations* and *Perform UTD Computations.*

There are three main parts in the block diagram given in Figure B.1:

1. User enters the aircraft geometry as cross sections of the body along some sections. Fins, wings, stabilizers, etc., are entered as flat plates. A continuous surface representation of the fuselage is generated by using splined interpolation of the cross sections. This surface is then displayed on the workstation screen along with the flat plates. HARP does not yet have the capability to read the various databases used by the aviation/aerospace industry, but is anticipated soon.

2. Depending on the frequency and size, one uses either the high frequency method (UTD) or the low frequency MM technique. The models are different based on the method chosen, as given below:

   (a) If the aircraft is to be analyzed via UTD, a model that simulates the fuselage by a composite ellipsoid is generated and displayed. The radiation patterns of the antennas on this model are then computed using the airborne antenna code [12].

   (b) If the user chooses MM, then the aircraft is modeled by polygonal plates and displayed. The radiation patterns are then computed via MM using the Aircraft Modeling Code (AMC) [29].

3. The results of the EM computation are displayed in a user friendly form, that is both easy to interpret and analyze.

B.3 Low Frequency MM Analysis

When conditions dictate that MM be the method most suitable for the analysis, the first step is the construction of a model to be used with AMC. This program requires that the fuselage be defined by cross sections, wings and fins by flat plates and antennas, rotor, etc. by wires. HARP converts the continuous surface model into a set of cross sections compatible with AMC. This is not a trivial task because

AMC needs the fin and wing attachments to exactly match the grid formed by the fuselage. AMC then converts the fuselage cross section data into a set of polygonal flat plates. The wings and fins are also flat plates. The rotor is modeled by a set of arbitrary wires.

Once the surface patch model of the helicopter has been computed, AMC continues with the complete MM computation. This involves the determination of the impedance matrix, the right hand side voltage vector, as well as the matrix of solution for the patch and wire currents. Once this is computed, AMC finally computes the required patterns in the far zone. Depending on the electrical size of the body, and the computational power at hand, the MM computation can take a few seconds to several hours of execution time.

B.4 High Frequency UTD Analysis

If the body is electrically large, then UTD provides the solution more efficiently. This task is accomplished by the use of NEWAIR3 computer program. NEWAIR3 requires the fuselage to be modeled by a composite ellipsoid and the remainder of the structures by flat plates. The composite ellipsoid need accurately model the aircraft only the neighborhood of the antenna. Note that the antenna is required to be attached to the fuselage. Flat plates (if necessary) need only be approximate. Both attached as well as unattached plates to the fuselage are treated by NEWAIR3.

It is emphasized that, in contrast to the moment method technique where the entire model has to be reasonably accurate, the UTD model needs to be accurate only in the vicinity of the antenna. This is due to the more localized nature of high frequency phenomena, such as diffraction, reflection etc. Therefore, the airplane model can be less accurate in the shadow regions, and locations away from the antenna.

HARP generates this composite ellipsoid very accurately, as well as the flat plates that are necessary to reasonably model the aircraft. If the user is satisfied with

the views of the model presented on the screen, he can then continue on to the computation of the required radiation patterns. These can once again be displayed on the screen.

Appendix C

Scattering from Waveguide Inlets

The analysis of the near field bistatic EM scattering by the waveguide is primarily based on the GTD and the ECM, as well as the PTD, combined with the self-consistent MSM. In the MSM based analysis, the basic scattering mechanisms are isolated and identified as being associated with the scattering by junctions I and II as in the waveguide shown in Figure C.1. The MSM procedure requires knowledge of the generalized scattering matrices $[S_{11}]$, $[S_{12}]$, $[S_{21}]$, $[S_{22}]$, and $[S_{I}]$ for the two junctions.

The scattering matrix concept in microwave circuit analysis is based on the propagating modes within the circuit. It characterizes the circuit properties or waveguide discontinuities of a microwave network. Hence, the circuit scattering matrix for microwave networks is limited to guided wave (interior) regions. On the other hand, the polarization scattering matrix is defined for exterior regions [30]. The generalized scattering matrix extends the concept of the microwave circuit scattering matrix to include evanescent modes for interior regions as well as the polarization scattering matrix for external scattering. Thus, this approach is useful for problems that involve a coupling between interior and exterior regions as in the geometry of Figure 5.1.

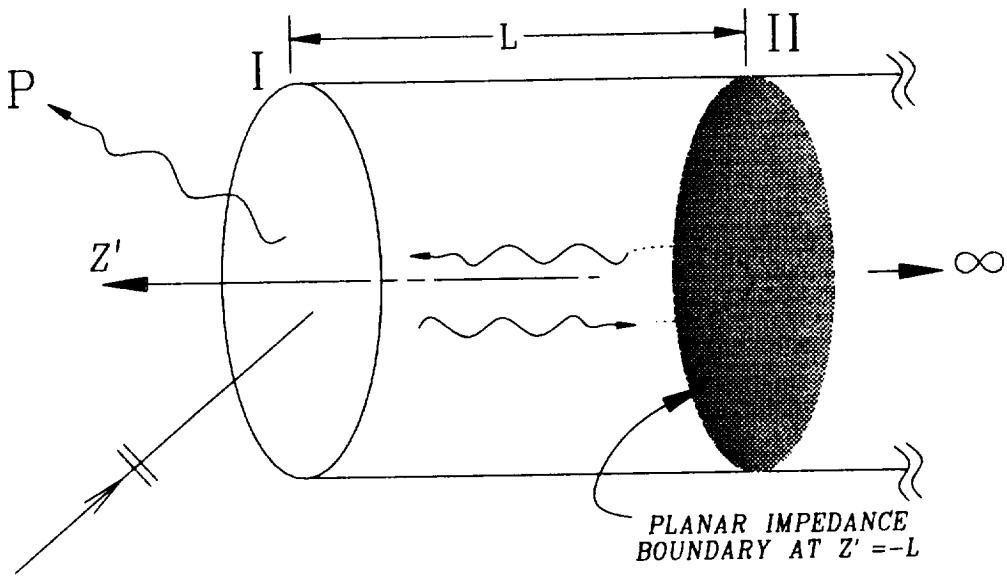

Figure C.1: Illustration of multiple scattering between junctions I and II in a terminated waveguide.

Let $\mathbf{E}^i$ denote the electric field intensity of the incident EM plane wave. One may express $\mathbf{E}^i$ as:

$$\mathbf{E}^i = \hat{\theta} E^i_0 + \hat{\phi} E^i_\phi \tag{C.1}$$

with

$$E^i_\theta = A_\theta e^{-j\bar{k}^i \cdot \bar{r}}, \qquad \text{and} \tag{C.2}$$

$$E^i_\phi = A_\phi e^{-j\bar{k}^i \cdot \bar{r}} \tag{C.3}$$

where

$$\bar{k}^i = -k(\sin\theta^i \cos\phi^i \hat{x} + \sin\theta^i \sin\phi^i \hat{y} + \cos\theta^i \hat{z}) \tag{C.4}$$

and

$$\bar{r} = x\hat{x} + y\hat{y} + z\hat{z}. \tag{C.5}$$

Note that k is the free space wave number and $\bar{r}$ is the position vector of an observation point at P.

The scattering matrix $[S_{11}]$ is described next. The matrix $[S_{11}]$ relates the electric field $\mathbf{E}^{so}$ scattered from only the open end at $z = 0$ to the field $\mathbf{E}^i$ which is incident

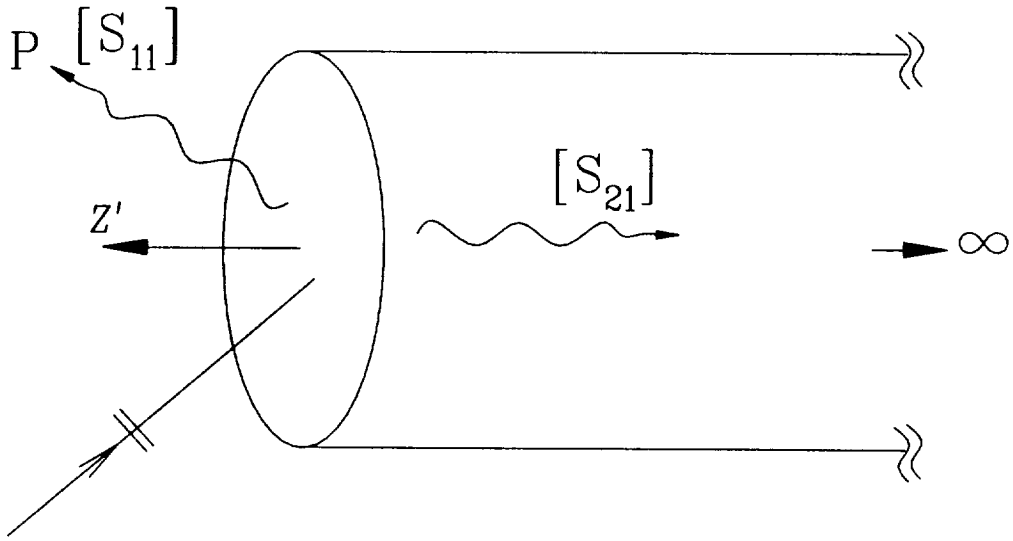

Figure C.2: Scattering by only the rim at the open end of the inlet. This scattering affects both the exterior and interior regions.

upon the open end as follows (see Figure C.2):

$$\begin{bmatrix} E_x^{so} \\ E_y^{so} \\ E_z^{so} \end{bmatrix} = \begin{bmatrix} S_{x\theta}^{so} & S_{x\phi}^{so} \\ S_{y\theta}^{so} & S_{y\phi}^{so} \\ S_{z\theta}^{so} & S_{z\phi}^{so} \end{bmatrix} \begin{bmatrix} A_\theta \\ A_\phi \end{bmatrix} \tag{C.6}$$

where

$$\mathbf{E}^{so}(P) = E_x^{so}\hat{x} + E_y^{so}\hat{y} + E_z^{so}\hat{z} \tag{C.7}$$

and

$$[S_{11}] = \begin{bmatrix} S_{x\theta}^{so} & S_{x\phi}^{so} \\ S_{y\theta}^{so} & S_{y\phi}^{so} \\ S_{z\theta}^{so} & S_{z\phi}^{so} \end{bmatrix}. \tag{C.8}$$

Note that A_θ and A_ϕ are the amplitudes of the incident fields E_θ and E_ϕ, respectively.

The scattering matrix $[S_{12}]$ converts the waveguide modal fields incident at the open end ($z = 0$) from the interior region ($z < 0$) to the fields radiated by these modes from the open end as shown in Figure C.3. The modal electric field $\mathbf{E}_g^{\pm}$ within the waveguide region ($z < 0$) may be represented as [31]:

$$\mathbf{E}_g^{\pm} = \sum_m \sum_n [A_{nm}^{\pm} \bar{e}'_{nm} e^{\mp j\beta'_{nm}z} + B_{nm}^{\pm}(\bar{e}_{nm} \pm \hat{z}\bar{e}_{znm})e^{\mp j\beta_{nm}z}] \tag{C.9}$$

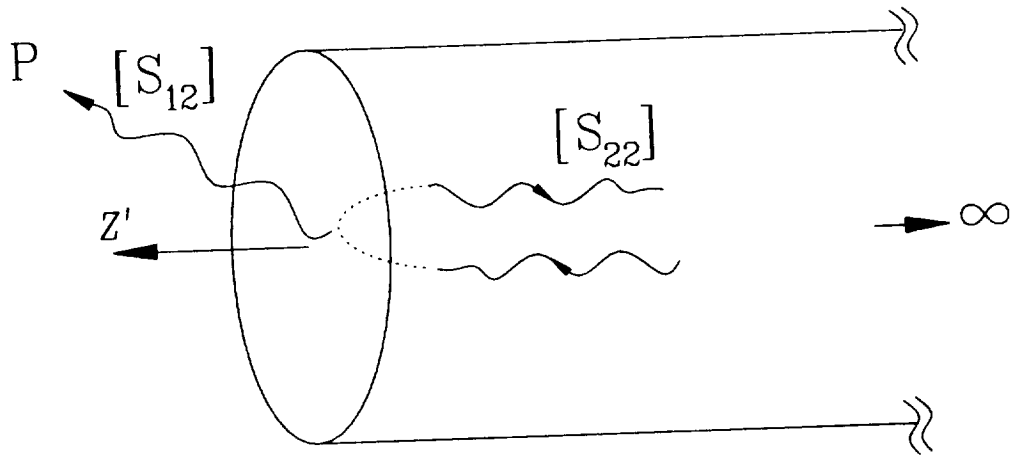

Figure C.3: Radiation and reflection at the open end due to a waveguide mode incident on the opening.

where, $\bar{e}'_{nm}$ and $\bar{e}_{nm}$ denote the transverse (to z) electric vector mode functions for the TE_{nm} and TM_{nm} modes, respectively. The $A^{\pm}_{nm}$ and $B^{\pm}_{nm}$ in (C.9) are the modal amplitude coefficients, and β'_{nm} and β_{nm} denote the propagation constants for the TE_{nm} and TM_{nm} modes, respectively. Here, n and m refer to the modal indices associated with the transverse eigenvalues in ϕ and ρ and eigenfunctions (modes), and e_{znm} is the $\hat{z}$-component of the TM_{nm} modal electric field. The corresponding e'_{znm} for the TE_{nm} are identically zero by definition. The superscripts $+$ and $-$ above refer to the modes propagating in the $+\hat{z}$ and $-\hat{z}$ directions, respectively.

If $\mathbf{E}^{ro}(P)$ denotes the electric field at P external to the waveguide region, which is radiated by the modes striking the open end, then the Scattering matrix $[S_{12}]$ relates $\mathbf{E}^{ro}(P)$ to $\mathbf{E}^{+}_{g}$ by

$$\begin{bmatrix} E^{ro}_x \\ E^{ro}_y \\ E^{ro}_z \end{bmatrix} = \begin{bmatrix} [S^{ro'}_x] & [S^{ro}_x] \\ [S^{ro'}_y] & [S^{ro}_y] \\ [S^{ro'}_z] & [S^{ro}_z] \end{bmatrix} \begin{bmatrix} [A^{+}_{nm}] \\ [B^{+}_{nm}] \end{bmatrix} \tag{C.10}$$

where

$$\mathbf{E}^{ro}(P) = E^{ro}_x \hat{x} + E^{ro}_y \hat{y} + E^{ro}_z \hat{z} \tag{C.11}$$

and

$$[S_{12}] = \begin{bmatrix} [S_x^{ro'}] & [S_x^{ro}] \\ [S_y^{ro'}] & [S_y^{ro}] \\ [S_z^{ro'}] & [S_z^{ro}] \end{bmatrix} \tag{C.12}$$

with

$$[S_i^{ro'}] = [S'_{i01}\ S'_{i02}\ \cdots\ S'_{i11}\ S'_{i12}\ \cdots\ S'_{inm}\ \cdots] \tag{C.13}$$

and

$$[S_i^{ro}] = [S_{i01}\ S_{i02}\ \cdots\ S_{i11}\ S_{i12}\ \cdots\ S_{inm}\ \cdots] \tag{C.14}$$

where $i = x, y, z$.

The scattering matrix $[S_{21}]$ describes the transformation or the coupling of the incident plane wave field into the waveguide modes as shown in Figure C.2. It is also noted that the determination of $[S_{21}]$ is related to the determination of $[S_{12}]$ via reciprocity, when the receiver recedes to the far zone in the latter problem. It may be seen that $[S_{21}]$ relates $\mathbf{E}_g^-$ to $\mathbf{E}^i$ via

$$\begin{bmatrix} [A_{nm}^-] \\ [B_{nm}^-] \end{bmatrix} = \begin{bmatrix} [S'_{\theta nm}] & [S'_{\phi nm}] \\ [S'_{\theta nm}] & [S'_{\phi nm}] \end{bmatrix} \begin{bmatrix} A_\theta \\ A_\phi \end{bmatrix} \tag{C.15}$$

where

$$[S_{21}] = \begin{bmatrix} [S'_{\theta nm}] & [S'_{\phi nm}] \\ [S'_{\theta nm}] & [S'_{\phi nm}] \end{bmatrix} \tag{C.16}$$

The scattering matrix $[S_{22}]$ is a modal reflection coefficient matrix associated with the mechanisms depicted in Figure C.3. In particular, the elements of $[S_{22}]$ describe the reflection coefficients associated with the TE_{nm} and TM_{nm} modes reflected back from the open end (at $z = 0$) into the waveguide region ($z < 0$) when either a TE_{pq} or a TM_{pq} mode in incident on the open end from within the waveguide. Thus, the matrix $[S_{22}]$ relates $\mathbf{E}_g^-$ to $\mathbf{E}_g^+$ by

$$\begin{bmatrix} [A_{nm}^-] \\ [B_{nm}^-] \end{bmatrix} = \begin{bmatrix} [R_{nm;pq}^{hh}] & [R_{nm;pq}^{he}] \\ [R_{nm;pq}^{eh}] & [R_{nm;pq}^{ee}] \end{bmatrix} \begin{bmatrix} [A_{pq}^+] \\ [B_{pq}^+] \end{bmatrix} \tag{C.17}$$

where

$$[S_{22}] = \begin{bmatrix} [R_{nm;pq}^{hh}] & [R_{nm;pq}^{he}] \\ [R_{nm;pq}^{eh}] & [R_{nm;pq}^{ee}] \end{bmatrix}. \tag{C.18}$$

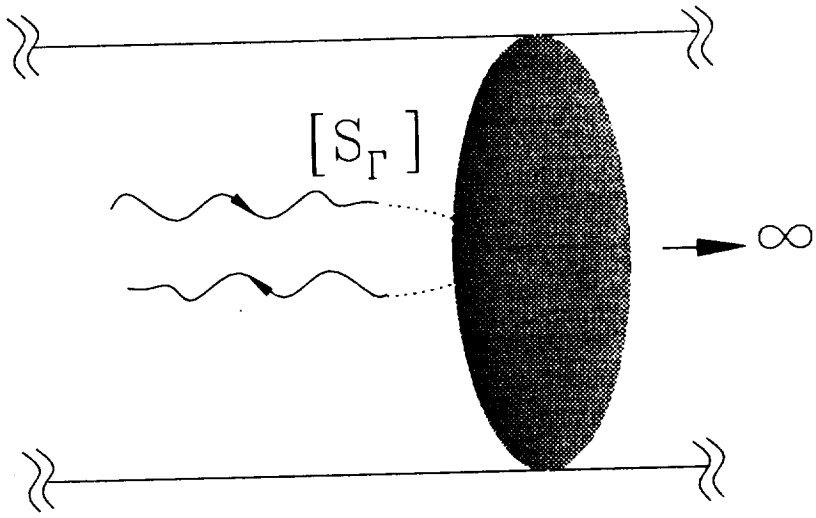

Figure C.4: Reflection of waveguide modes from the termination at $z = -L$.

Note that the reflection coefficient $R^{he}_{nm;pq}$ denotes the following: A TM_{pq} (or e type) mode with modal amplitude B^+_{pq} which is incident at the open end is partly transformed (coupled) into a reflected TE_{nm} (or h type) mode with modal amplitude $A^-_{nm} = R^{he}_{nm;pq} B^+_{pq}$.

The scattering matrix $[S_\Gamma]$, like $[S_{22}]$, is also a reflection coefficient type matrix which is associated with the termination at $z = -L$. This mechanism is illustrated in Figure C.4. For this case, one obtains that

$$\begin{bmatrix} [A^+_{nm}] \\ [B^+_{nm}] \end{bmatrix} = \begin{bmatrix} [\Gamma^{hh}_{nm;pq}] & [\Gamma^{he}_{nm;pq}] \\ [\Gamma^{eh}_{nm;pq}] & [\Gamma^{ee}_{nm;pq}] \end{bmatrix} \begin{bmatrix} [A^-_{pq}] \\ [B^-_{pq}] \end{bmatrix} \tag{C.19}$$

where

$$[S_\Gamma] = \begin{bmatrix} [\Gamma^{hh}_{nm;pq}] & [\Gamma^{he}_{nm;pq}] \\ [\Gamma^{eh}_{nm;pq}] & [\Gamma^{ee}_{nm;pq}] \end{bmatrix}. \tag{C.20}$$

As before, for example, $\Gamma^{he}_{nm;pq}$ relates A^+_{nm} to B^-_{pq} via $A^+_{nm} = \Gamma^{he}_{nm;pq} B^-_{pq}$.

At any given frequency, the waveguide region (interior) can support a finite number of propagating modes and an infinite number of non-propagating (evanescent) modes. Hence, strictly speaking, the matrices $[S_{12}]$, $[S_{21}]$, $[S_{22}]$ and $[S_\Gamma]$ are of infinite order. However, in practice, one need retain only a finite number of elements of the matrix (finite number of modes), because the distance L is generally large,

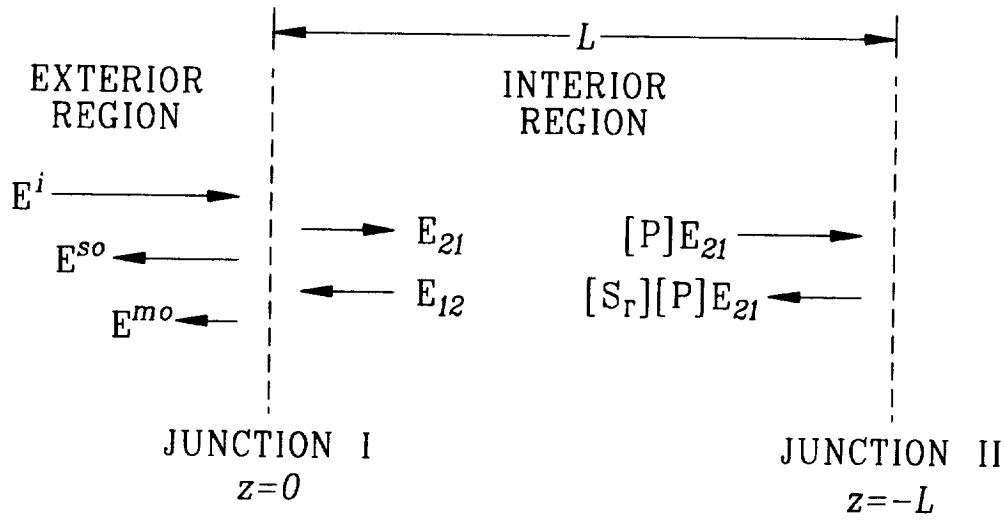

Figure C.5: Multiple interations between junctions I and II for calculating the total scattered field.

and the infinite number of modes generated at junction I contribute negligibly at junction II, and vice versa. Therefore, only a finite number of propagating modes are retained in practice. If the distance L is too small, such that these evanescent modes do become important, then one must include these modes, but one may still ignore the higher-order evanescent mode contributions.

The fields scattered by the inlet may be viewed as the superposition of two parts, one of which is the scattered field from the open end (rim) by itself. The other field is that radiated by the open end as a result of all the interactions between the open end and the termination, which arises from the incident field coupled into the waveguide region. Referring to Figure C.5, it is seen that the field scattered by junction I is simply

$$[E^{so}] = [S_{11}][E^i] \tag{C.21}$$

where

$$[E^{so}] = \begin{bmatrix} E_x^{so} \\ E_y^{so} \\ E_z^{so} \end{bmatrix}. \tag{C.22}$$

A part of the incident field is coupled at I into the waveguide region, which becomes the incident field at junction II from which it is reflected. The field reflected

by junction II impinges again on I, where it experiences further scattering into the exterior and interior regions. This process repeats *ad infinitum*. The fields resulting from these multiple interactions may be found from the self-consistent MSM analysis, which is briefly described below.

Let $[E_{12}]$ be the total field incident at I from II after taking all the multiple interactions into account. Similarly, let $[E_{21}]$ represent the total field incident at junction II from I after taking all the multiple interactions into account. Then, the total scattered field in the exterior region $[E^s]$ consists of superposition of $[E^{so}]$ and $[E^{mo}]$, where $[E^{mo}]$ is the field scattered into the exterior region when $[E_{12}]$ is incident on I. Hence,

$$[E^s] = [E^{so}] + [E^{mo}] \tag{C.23}$$

where

$$[E^{mo}] = [S_{12}][E_{12}]\Big|_{z=0} \tag{C.24}$$

Writing the expressions for $[E_{12}]$ and $[E_{21}]$ in terms of $[S_{21}]$ and $[S_{22}]$,

$$[E_{21}]\Big|_{z=0} = [S_{21}][E^i] + [S_{22}][E_{12}]\Big|_{z=0} \tag{C.25}$$

and

$$[E_{12}]\Big|_{z=0} = [P][S_\Gamma][P][E_{21}]\Big|_{z=0} \tag{C.26}$$

where, $[S_\Gamma]$ denotes the reflection coefficient scattering matrix for the junction II as defined in (C.20), and $[P]$ is a diagonal matrix accounting for the phase delay along the length L of the waveguide between junctions I and II. Eliminating $[E_{12}]$ from (C.25) and (C.26) yields:

$$([I] - [S_{22}][P][S_\Gamma][P])\,[E_{21}]\Big|_{z=0} = [S_{21}][E^i] \tag{C.27}$$

where $[I]$ is an identity matrix of infinite order. Solving (C.27) for $[E_{21}]$, one obtains that

$$[E_{21}]\Big|_{z=0} = ([I] - [S_{22}][P][S_\Gamma][P])^{-1}[S_{21}][E^i]. \tag{C.28}$$

Substituting (C.28) into (C.26), one finds that

$$[E_{12}]\Big|_{z=0} = [P][S_\Gamma][P]([I] - [S_{22}][P][S_\Gamma][P])^{-1}[S_{21}][E^i]. \qquad \text{(C.29)}$$

From (C.29) and (C.24), the total exterior scattered field from the internal scattering is given by

$$[E^{mo}] = [S_{12}][P][S_\Gamma][P]([I] - [S_{22}][P][S_\Gamma][P])^{-1}[S_{21}][E^i]. \qquad \text{(C.30)}$$

Finally, the self-consistent expression for the total scattered field $[E^s]$ can be written from (C.21), (C.30) and (C.23) as

$$[E^s] = \left\{[S_{11}] + [S_{12}][P][S_\Gamma][P]([I] - [S_{22}][P][S_\Gamma][P])^{-1}[S_{21}]\right\}[E^i]. \qquad \text{(C.31)}$$

It is noted that the above scattering matrices are different from the conventional scattering matrices due to the fact that they contain range information. They remain valid for field calculations in the near zone of the inlet opening. Further, as noted in [20], the above analysis is *restricted to angles of incidence and scattering which are about 60° or less* from the forward axis of the inlets.

The scattering matrices $[S_{11}]$, $[S_{12}]$, $[S_{21}]$, and $[S_{22}]$ can be found via asymptotic high frequency techniques (such as UTD, ECM and PTD). The methods are discussed in detail in [32] and [20] and not repeated here.